AERODYNAMIC ANALYSIS AND DRAG COEFFICIENT EVALUATION OF TIME-TRIAL BICYCLE RIDERS

by

Peter Nicholas Doval

A Thesis Submitted in

Partial Fulfillment of the

Requirements for the Degree of

Master of Science

in Engineering

at

The University of Wisconsin – Milwaukee

December 2012

ABSTRACT

AERODYNAMIC ANALYSIS AND DRAG COEFFICIENT EVALUATION OF TIME-TRIAL BICYCLE RIDERS

by

Peter Nicholas Doval

The University of Wisconsin – Milwaukee, 2012
Under the Supervision of Professor Ilya V. Avdeev

Evaluation of drag coefficient often requires wind tunnel experiments and can be prohibitively expensive if not impossible for large objects or systems. Computational Fluid Dynamics (CFD) aerodynamic analysis offers an alternative approach and can be used as a very effective design tool in many industries: automotive, aerospace, marine, etc. The main objective of this research is to investigate feasibility of using non-contact digitizers for developing finite element models of large objects for subsequent CFD analysis. The developed methodology is applied to investigation of time-trial bicycle rider efficiency. Companies competing in this class of racing spend millions trying to optimize bicycle and rider geometry in order to reduce aerodynamic drag. This project investigates an alternative way to optimize the aerodynamic efficiency of the rider, considering the rider contributes the majority of the drag force of the rider-bicycle system. If small riding position adjustments could be made to the rider's body during a race, drag may be significantly reduced. This idea, and the fact that the direction of wind impacting the rider can vary, influenced the concept of this project. It was hypothesized that adjusting the time-trial handlebars on the bicycle to stagger the fore-aft position of the rider's hands would influence the upper body to rotate

slightly. This could then reduce the frontal area of the rider in the wind direction, therefore reducing the aerodynamic drag. To simulate this situation, the Konica Minolta VIVID 910 non-contact 3-D digitizer was used to scan two separate riders, each aboard a different bicycle, in several positions, as described above. The 3-D scans were then imported into the CFD software package Star-CCM+ and several simulations were run using each of the two rider-bicycle models. The initial simulations seemed to support the theory as the asymmetrical riding position experienced decreased drag at significant wind yaw angles while the normal riding position did not. A second study, using a different rider and bicycle, yielded less conclusive results. The two studies represent the groundwork for similar large system CFD analysis and provide useful recommendations for continued research into bicycle rider aerodynamics.

TABLE OF CONTENTS

LIST OF FIGURES

LIST OF TABLES

ACKNOWLEDGEMENTS

Foremost, I would like to thank Dr. Ilya Avdeev, my graduate advisor and director of the Advanced Manufacturing and Design Laboratory, for his continued support and enthusiasm regarding my work on this project and others. Also working with Dr. Avdeev in the AMDL were my colleagues Austen Scudder, Mike Martinsen, Alex Francis, Andrew Hastert, Mir Shams, Mehdi Gilaki, Matt Juranitch, Jesse DePinto, and Calvin Berceau, who all offered their support and friendship at one time or another. Additionally, for encouraging my interest in Computational Fluid Dynamics and acting as an excellent and patient mentor, I would like to thank Rob Brummond.

For providing the excellent foundation upon which I've built my outstanding undergraduate and graduate education, I would also like to thank the University of Wisconsin–Milwaukee, specifically the Graduate School, the College of Engineering and Applied Science, and the Department of Mechanical Engineering. With the above resources at hand, I had the tools and support I needed to investigate and expand my engineering knowledge and to attain a higher level of technical and professional expertise than I had previously thought possible.

I would like to thank my parents, Peter and Helen Doval, for their constant support and praise throughout my many years of education and professional development. And finally, my four older siblings, Abram Doval, Justin Doval, Nora Siwarski and Grace Doval, for providing me with motivation and guidance toward my schooling through their many accomplishments in life.

1 INTRODUCTION

Aerodynamic evaluation of larger systems, from bicycles to airplanes, is an important topic and requires significant effort and financial investment in today's efficiency-driven world. Whether the application of the product is racing, where speed is key, or it is commercial transportation, where efficiency of moving goods around the country may be the highest priority, wind tunnel experiments and CFD simulations must be an area of serious consideration. This work addresses the need for development of a virtual wind tunnel, to be used as a design instrument for large-scale systems. The specific objectives of this research are:

1. Developing 3-D scanning methodology for the digitization of large systems.
2. Developing CFD methodology for aerodynamic analysis of large systems.
3. Applying developed methodologies to investigation of drag characteristics of various time-trial bicycle riding positions.

In the trucking industry, Peterbilt Motors Company has invested more and more effort over the years in the aerodynamic efficiency of their tractor-trailer packages. In 1988, Peterbilt introduced the Model 372 which could achieve fuel efficiency of 11mpg in a market where 5mpg was the accepted norm (Peterbilt Motors Company, 2001). Given the size of tractor-trailers, full-scale wind tunnel testing would be an extremely expensive undertaking for most companies and may not be a possible option for others. Scaled-down testing would be an alternative but wind tunnel use still requires significant financial and time

investments. This is an area where the use of computational fluid dynamics could save companies millions and speed up product development. This can make a great difference in fast-paced industries, like the automotive industry, where companies often race to put new technology on the road. Small scale wind tunnel testing is useful for small systems but, when large systems are considered, CFD simulations are invaluable.

The sport of road bicycle racing is continuously pushing the bounds of new technology and investigating every conceivable method to increase speed and efficiency. In time-trial cycling, bicycles are made as aerodynamically efficient as the governing rules allow and companies are always searching for new ways to be the fastest. Sponsored riders competing in the Ironman triathlon, for example, can spend hours pedaling in a wind tunnel to collect useful data in order to improve their aerodynamics. These wind tunnel tests allow a unique opportunity for the riders to obtain immediate feedback for riding position optimization in order to reduce drag. An unfortunate aspect of these useful wind tunnel tests is the financial investment required to rent the wind tunnel. Athletes training with Carmichael Training Systems in preparation for the 2008 Ironman World Championships rented time in a wind tunnel for $1,500 per hour (Rutberg, 2008). Recently, time-trial bicycle design has followed that of the aeronautic industry to produce airfoil-shaped frames, wheels, seat posts, handlebars, etc. A study presented at the 2010 STAR European Conference utilized CFD to compare several different wheel designs for time-trial use, many of which utilized an

airfoil-shaped cross-section in an attempt to reduce drag (Godo, 2010). Meanwhile, the riders are also outfitted to be as streamlined as possible. In 1990, a patent was filed for a streamlined bicycle racing helmet by Giro to assist the rider in decreasing his/her contribution to the overall drag of the bicycle and rider system (Gentes & Sasaki, 1990). Many of these initial design approaches based on the shape of an airfoil have yielded positive results, but other factors that are not present in aeronautics come into play when considering the lower speed of bicycle travel. The most significant factor in this case is that of wind yaw angle. The speeds at which bicycles usually race tend to almost always yield a resultant wind yaw angle – the resultant wind vector impacting the rider and bicycle is not parallel to their direction of travel. This fact has led some companies to investigate methods to reduce drag when a wind yaw angle is present. This study experiments with an asymmetric riding position for this very purpose – to reduce drag when a wind yaw angle is present.

Current testing methods used in the bicycle racing industry employ primarily wind tunnel testing for aerodynamic studies. Trek Bicycle Corporation utilizes a full-scale, articulating mannequin to simulate a pedaling rider in their full-scale wind tunnel tests. They also have the capability to test at different yaw angles in the wind tunnel, necessary because of the nearly always apparent cross wind in bicycling (Harder, Cusack, Matson, & Lavery, 2010). Another study related to wind yaw angle was conducted in 2009 by Wing-Light. This study compared several different time-trial bicycle wheels subject to differing wind yaw angles

(Knupe & Farmer, 2009). Studies of this sort are becoming more necessary as other legal aerodynamic technologies are exhausted. As more teams obtain the newest technologies to improve the aerodynamics of their bicycles and riders, teams who want to remain at the front will need to discover new ways to do so.

Many bicycle companies have just recently begun to employ the use of CFD analysis coupled with a 3-D scanned model of a real rider. This approach has the ability to fine tune bicycle and riding position geometry based on rider size, build, body composition, etc. Throughout 2012, new studies have been conducted using these powerful methods. From studies on a new helmet design, utilizing golf ball-like dimples (LG, 2012), to the use of a scanned rider to validate new time-trial bicycle frame designs (Sidorovich, 2012), these methods are becoming more and more mainstream. However, it is yet unknown if any company has investigated posture changes to help reduce drag at different yaw angles. Trek has discovered frame geometry, seen on the Speed Concept bicycle, which exploits the principles of angled wind velocities but it is not apparent that anyone has investigated differing postures to do the same. If a theory like this one is proved to provide even the slightest advantage in real-world racing conditions, it could become a must-have technology for those teams who wish to exhaust all methods within regulation in order to win.

1.1 3-D SCANNING

A crucial step in a project like this is accurately capturing the geometry and building a 3-D representation of the subject. Achieving a 3-D model of the human

body is not a new practice, either. In 1996, Paquette describes the use of a 3-D laser scanner to digitize an outfitted paratrooper in order to simulate soldiers in free fall after exiting an aircraft (Paquette, 1996). Today, there are several different technologies available for 3-D scanning and each exhibit their own advantages. 3DMD manufactures a flash-based scanner where four arranged cameras capture an image of the object from slightly different angles within two milliseconds when the flash is triggered. Polhemus sells a handheld laser triangulation scanner with a fixed camera and a projected laser stripe to digitize a surface. The Konica Minolta Vivid 910, used in this project, is similar to the Polhemus but it is fixed on a tripod or desktop. A laser stripe sweeps across the object and the reflection is captured by the camera and triangulated to produce a 3-D image. In a 2005 study, the Konica Minolta scanner provided superior surface accuracy over the previous two choices (Boehnen & Flynn, 2005).

The goal is to generate a single, closed 3-D model of the rider aboard the bicycle. For this to be possible, scans from many different angles are necessary. There are several different approaches to achieving a complete scan of an object, from several linked scanners working together to a singular scanner with the object placed on a turntable. Many of these methods, however, can be sensitive to movement because of the time taken to complete a scan and the need for multiple, separate scans. For example, the Cyberware scanner used in military and apparel engineering applications can scan the human body in roughly 17 seconds. This, however, requires the subject to hold very still during the process

and even shallow breathing can result in surface errors (Paquette, 1996). The scanning of the human body brings with it difficulties relating to scan time. This is a problem not encountered when scanning static objects and can be somewhat resolved by quick scanning methods, like the 3DMD mentioned above.

An additional, low-cost option, currently being investigated by researchers in the Advanced Manufacturing and Design Lab at UW-Milwaukee, is a structured light 3-D scanner. A simple design of this scanner has been mocked up and includes a small multimedia projector and a CCD camera interfaced through an open source software package called David–LaserScanner (DAVID 3D Solutions, 2012). Once properly calibrated, this technology should allow better resolution and greater focal range than the VIVID 910 laser scanner. Continued research on this project could greatly benefit from the use of such a scanner.

1.2 BICYCLE AERODYNAMICS

As stated previously, a rider aboard a bicycle contributes a majority of the aerodynamic drag of the entire bicycle and rider system. In fact, a rider's body typically contributes 70% of the total aerodynamic drag of the system (Gross, Kyle, & Malewicki, 1983). There have, over the years, been many advancements in bicycle design to decrease the drag experienced by the rider. Although not legal for use in most racing classes, like the Tour De France, several fairing designs which enclose the rider for a more streamlined system have yielded impressively low drag coefficients and equally impressive top speeds. The current top speed record for a bicycle was set at the World Human Powered Speed Challenge in

2009 by Sam Whittingham, who managed a top speed of 83mph in his fully-faired recumbent bicycle ("IHPVA Official Land Speed Records," 2009). When the assistance of a streamlined fairing is not available, the clothing on the rider and the position of the rider become very important. This is illustrated by the many new technologies emerging every year, from aerodynamically optimized helmets and shoes to tight-fitting, full-body race suits. The United Kingdom's Olympic team, UK Sport, began investing heavily in CFD technologies around 2004 with the addition of a new R&I Director. They were rewarded for this effort by capturing 14 of the 25 medals awarded in the 2008 Olympic cycling events (Hanna, 2011). Beyond equipment, the position of the rider has been studied for 0° wind yaw angle riding. Several studies can be found regarding drag as a function of rider torso angle in different racing scenarios(Defraeye, Blocken, Koninckx, Hespel, & Carmeliet, 2010a; Underwood & Schumacher, 2011). In a study performed at the Lowe's Motor Speedway in 2008, a rider travelling at 8.61m/s experienced yaw angles in the range of +/-7° (Cote, 2008). Some may think this range of yaw angle is negligible in the grand scheme of a road race but, as Trek has shown, even optimizing the frame to better handle a crosswind has proven advantageous. The methods discussed in this thesis may prove to do the same with the rider's body.

1.3 DRAG COEFFICIENT

The term drag relates to the resistance of an object as it moves through a fluid and can be represented as a unit of drag force, D. Drag force is the summation of

both friction and pressure (form) drag. Friction drag, D_f, is produced when a viscous fluid flows over a surface. A comparison of the two is simply illustrated in Figure 1 below.

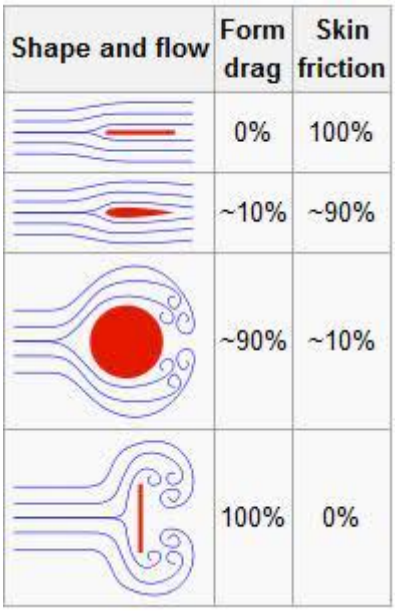

Figure 1 – Form Drag vs. Friction Drag
("Drag (Physics)," 2012)

The friction drag is produced by the shearing of the fluid in the boundary layer, created as a result of no-slip condition, and is given by:

$$D_f = \oint \tau_w \sin\varphi dS \quad (1)$$

Pressure drag, D_p, is produced by flow separation at the rear end of a blunt object, leading to a negative pressure area behind such object. This pressure gradient from the front to the rear of the object will produce the pressure drag force, given by:

$$D_p = \oint p\cos\varphi dS \quad (2)$$

where τ_w and p are the shear stress and pressure acting on the surface area, dS, and φ is the angle measured from the direction of free stream flow. More commonly used is the dimensionless representation of drag called the drag coefficient, C_d, and can be calculated using the following equation (Hucho, 1998):

$$C_d = \frac{(Df + \mathrm{D}p)}{\frac{1}{2}\rho v^2 A} \tag{3}$$

where ρ is the fluid density, v is the velocity of the object relative to the fluid, and A is the reference area of the object.

Drag on bicycles plays a much larger role than on automobiles, for example, as a rider aboard a bicycle is not a smooth object like a passenger car. An aerodynamically designed car can have minimal flow separation; therefore most of the drag force will be friction drag and a smaller percentage pressure drag. A passenger car, for example, typically has a drag coefficient in the range of 0.3 to 0.35 (Shahbazi, 2007). A bicycle and rider are very different in the way drag is produced. The general shape of a rider aboard a bicycle is not streamlined and there are many pockets where air can be trapped and increase drag. Common aerodynamic drag coefficient values for bicycles can range from 0.6 to 0.8 in racing configurations (Debraux, Grappe, Manolova, & Bertucci, 2011).

Drag studies for applications with complicated geometry, like that of automobiles, motorcycles, and bicycles, can be extremely difficult to solve directly. A simplified model of such an object could be used to calculate initial drag values by hand but it will be a significant approximation of the real-world case. The problem of complicated geometry causes most industries to jump

straight to CFD simulations and wind tunnel testing. A CFD simulation can be set up easily and a rough simulation can be solved in far less time than a team of engineers working out calculations by hand.

As CFD simulation software advances and becomes more accessible and user friendly, companies in the automotive and aerospace industries are relying more heavily on these computer simulations. CFD simulations, if set up accurately, could completely replace wind tunnel testing, saving companies millions as wind tunnel work can be extremely expensive. A current convention of many automotive companies is to use CFD for initial designs and only use wind tunnel testing for validation purposes. Once a configured simulation is validated through wind tunnel testing, it may be applied to many other tests very easily and without significant financial investment.

1.4 TURBULENCE MODELING

Computational fluid dynamics can be utilized for the two main flow scenarios, laminar and turbulent flow. Laminar flow is very simple and predictable and tends to be less useful when attempting to simulate real-world situations. Turbulent flow, on the other hand, can be utilized to simulate virtually any real-world flow situation. It is also characterized by very chaotic and unpredictable flow. Modeling turbulent flow, therefore, is significantly more complicated than laminar flow. The governing equations on which laminar and turbulent flow are modeled are called the Navier-Stokes equations. They were originally developed to model laminar flow but it was later discovered that they allowed for additional

refinement in order to model turbulent flow (Chen & Jaw, 1998). The Navier-Stokes equations for continuity, momentum, and energy are shown as follows:

$$\frac{\partial U_i}{\partial X_i} = 0 \tag{4}$$

$$\rho \frac{DU_i}{Dt} = \rho G_i - \frac{\partial P}{\partial X_i} + \mu \frac{\partial^2 U_i}{\partial X_j X_j} \tag{5}$$

$$\rho C_p \frac{DT}{Dt} = k \frac{\partial^2 T}{\partial x_j x_j} + \mu \left(\frac{\partial U_i}{\partial x_j} + \frac{\partial U_j}{\partial x_i} \right) \frac{\partial U_i}{\partial x_j} \tag{6}$$

where U is the fluid velocity, x represents position, ρ is the fluid density, G is the generation rate of turbulent kinetic energy, P is pressure, μ is fluid dynamic viscosity, C_p is the fluid heat capacity, T is temperature, and k is turbulent kinetic energy.

In order to more easily define turbulent motion, the method of Reynolds Averaging is implemented. The following equations are the foundation of a majority of turbulence modeling methods used today and are called the Reynolds-Averaged Navier-Stokes (RANS) equations.

$$\frac{\partial}{\partial x_i} \left(\overline{U_i} \right) = 0 \tag{7}$$

$$\frac{\partial}{\partial x_j} \left(\rho \overline{U_i}\, \overline{U_j} \right) = - \frac{\partial \overline{p}}{\partial x_i} + \frac{\partial}{\partial x_j} \left[\mu \left(\frac{\partial \overline{U_i}}{\partial x_j} + \frac{\partial \overline{U_j}}{\partial x_i} \right) - \rho \overline{u_i u_j} \right] \tag{8}$$

where $U_i(t) = U_i = \overline{U_i} + u_i$, the velocity in the i direction is represented as the sum of the time-averaged velocity component and the fluctuating velocity component. Equation 7 above is known as the continuity equation while Equation 8 represents the Navier-Stokes momentum equations (Zaïdi, Fohanno, Taïar, & Polidori, 2010).

Beyond the RANS equations, there have been several methods developed for modeling the remaining unknown variables: the Reynolds stresses ($\overline{u_i u_j}$). The two most commonly used RANS models today are the $k-\varepsilon$ and $k-\omega$ turbulence models. The latter has been modified to better resolve near-wall boundary layer flow, where the $k-\varepsilon$ model requires the use of a dedicated wall function, through the introduction of specific dissipation rate, ω. The general form of the $k-\omega$ model is as follows:

$$\frac{\partial}{\partial x_j}\left(\rho k\overline{U_j}\right) = \frac{\partial}{\partial x_j}\left(\Gamma_k \frac{\partial k}{\partial x_j}\right) + P_k - Y_k \tag{9}$$

$$\frac{\partial}{\partial x_j}\left(\rho \omega\overline{U_j}\right) = \frac{\partial}{\partial x_j}\left(\Gamma_\omega \frac{\partial \omega}{\partial x_j}\right) + P_\omega - Y_\omega \tag{10}$$

where Γ_k and Γ_ω are the effective diffusivities of k and ω, and Y_k and Y_ω are the turbulent dissipation rates of k and ω (Wilcox, 1994; Zaïdi et al., 2010).

One commonly used optimization of the $k-\omega$ model is called the $k-\omega$ *SST* (Shear-Stress Transport) model. This model has been optimized within the aeronautics field to better resolve flow scenarios with flow separation and large pressure gradients (Kuntz & Ferreira, 2003). The optimization of the formula results in the addition of a blending function, F_1, and a transformation term, D_ω, resulting in the following modified equation for specific dissipation rate, ω (Bartosiewicz et al., 2003).

$$\frac{\partial}{\partial x_j}\left(\rho \omega\overline{U_j}\right) = \frac{\partial}{\partial x_j}\left(\Gamma_\omega \frac{\partial \omega}{\partial x_j}\right) + P_\omega - Y_\omega + (1 - F_1)D_\omega \tag{11}$$

Using this optimized equation, many different fluid dynamics problems may be accurately evaluated without excessive computational resources.

2 METHODOLOGY DEVELOPMENT

Upon the undertaking of this project, a pilot study was done to investigate the plausibility of the theory. To begin this study, a 3-D scan of a rider aboard a Trek TTX bicycle was captured with the Konica Minolta Vivid 910 non-contact 3-D digitizer. This device was provided with a user interface software package called Polygon Editing Tool (PET). This software was used to control camera settings, capture 3-D images, and export images for further processing. The rider was captured in two different riding positions. First, the rider assumed a conventional, symmetric time-trial riding position. Second, the rider adjusted the time-trial handlebars of the bicycle to shift one hand rearward, in an asymmetric riding position. Using Geomagic, a reverse engineering and 3-D inspection software, the 3-D images were assembled, and converted into STL file format (Geomagic, 2010). Significant time was needed in the generating of complete and closed 3-D models as inconsistencies in the scanned images required more time than expected for assembly – as much as 80% of the total work effort. It was therefore recommended that a better method of producing the 3-D model of bicycle and rider be determined. As many as 50 separate 3-D images were captured and assembled to produce each of the two 3-D models. The symmetric position model can be seen below, in Figure 2. It was also observed that small changes in posture occurred between laser scanning captures. The method used required the rider to dismount and rotate the bicycle several times while keeping the camera stationary in order to capture images from all necessary angles.

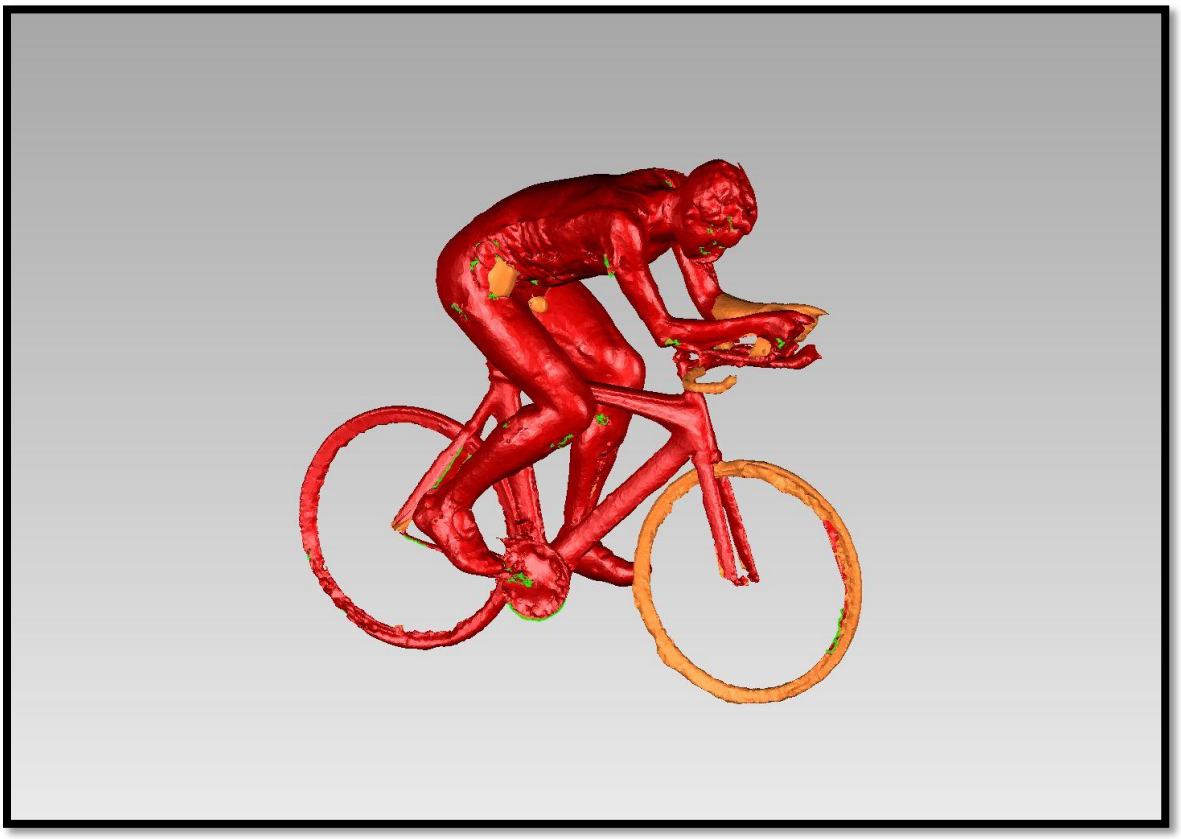

Figure 2 – Complete 3-D Scan of Rider and Bicycle

To perform the simulation, the CFD program Star-CCM+ was chosen. The 3-D models of each riding position were imported into Star-CCM+ and set up in various configurations. Each of the two riding positions was set up at various yaw angles from -45° (CW rotation of the bicycle and rider from top view) to 45° (CCW).

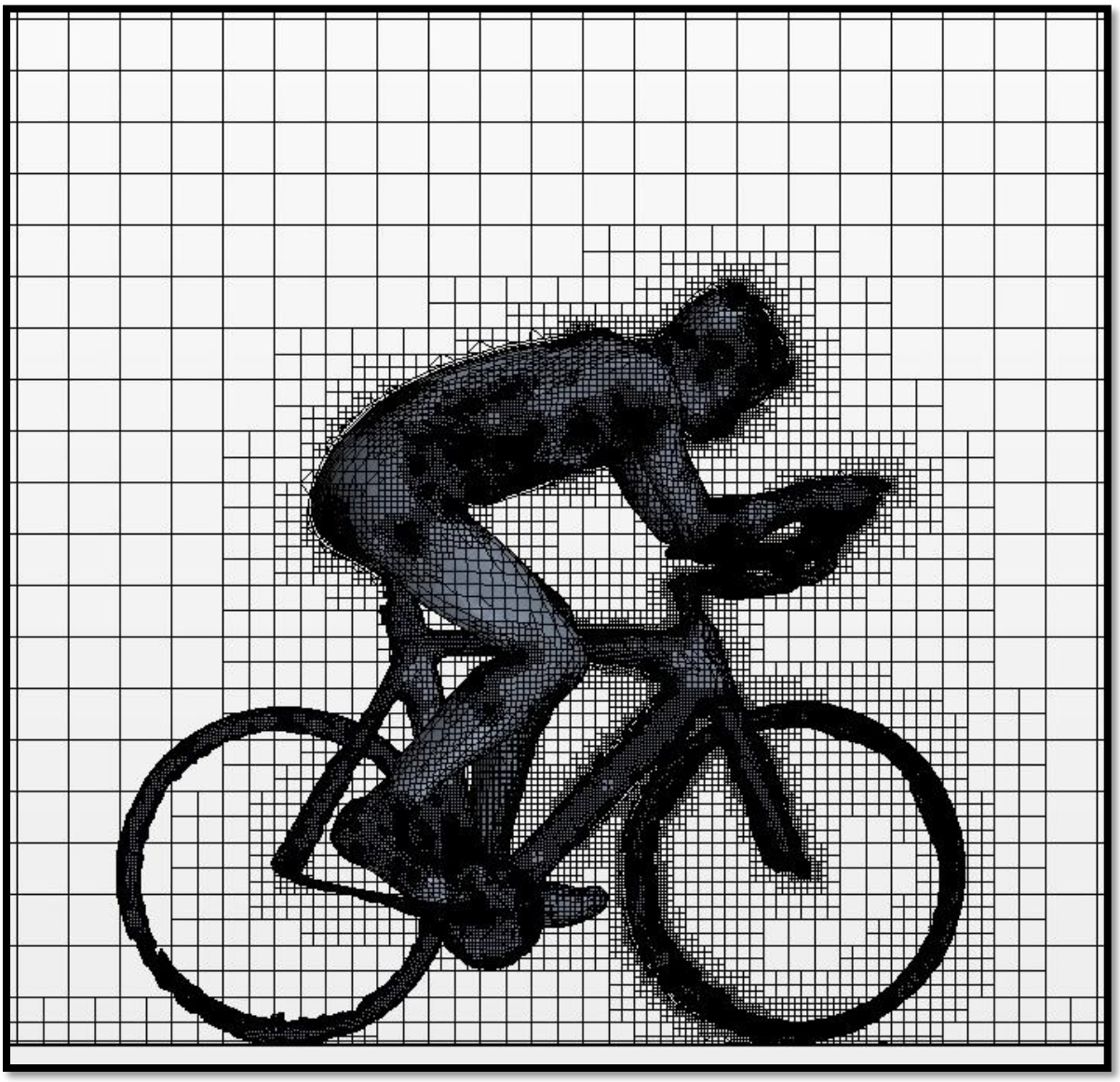

Figure 3 – Finite Element 3-D Mesh

A wind speed of 10m/s was used in the 4x4m test section, representing a common bicycle race speed (Defraeye et al., 2010a). No-slip condition was used on all surfaces, including walls and floor of the test section to align with subsequent wind tunnel experimentation. The turbulence model used was the

$k-\omega\ SST$ model as this is the accepted method for low Reynolds number cases and has proved best performing in bicycle CFD simulations (Defraeye, Blocken, Koninckx, Hespel, & Carmeliet, 2010b; Hucho, 1998). Meshing setup, shown in Figure 3, included the use of hexahedron volume cells with 2 prism layers on all test section boundaries while 4 prism layers were used on the rider and bicycle boundary. The prism layers retain parallel orientation to the surface, therefore allowing better resolution of boundary layer effects for more accurate drag approximations (Matsushima, 2001).

Finally, in order to verify the setup of the bicycle simulations, a CFD simulation of a sphere was configured using similar mesh and turbulence model parameters. The sphere was sized to yield a similar frontal area to the bicycle and rider model. Physics parameters were unchanged and the mesh was adjusted only slightly in order to assist convergence. The results of the simulations were then compared to experimental results obtained from textbook sources.

2.1 PILOT STUDY RESULTS

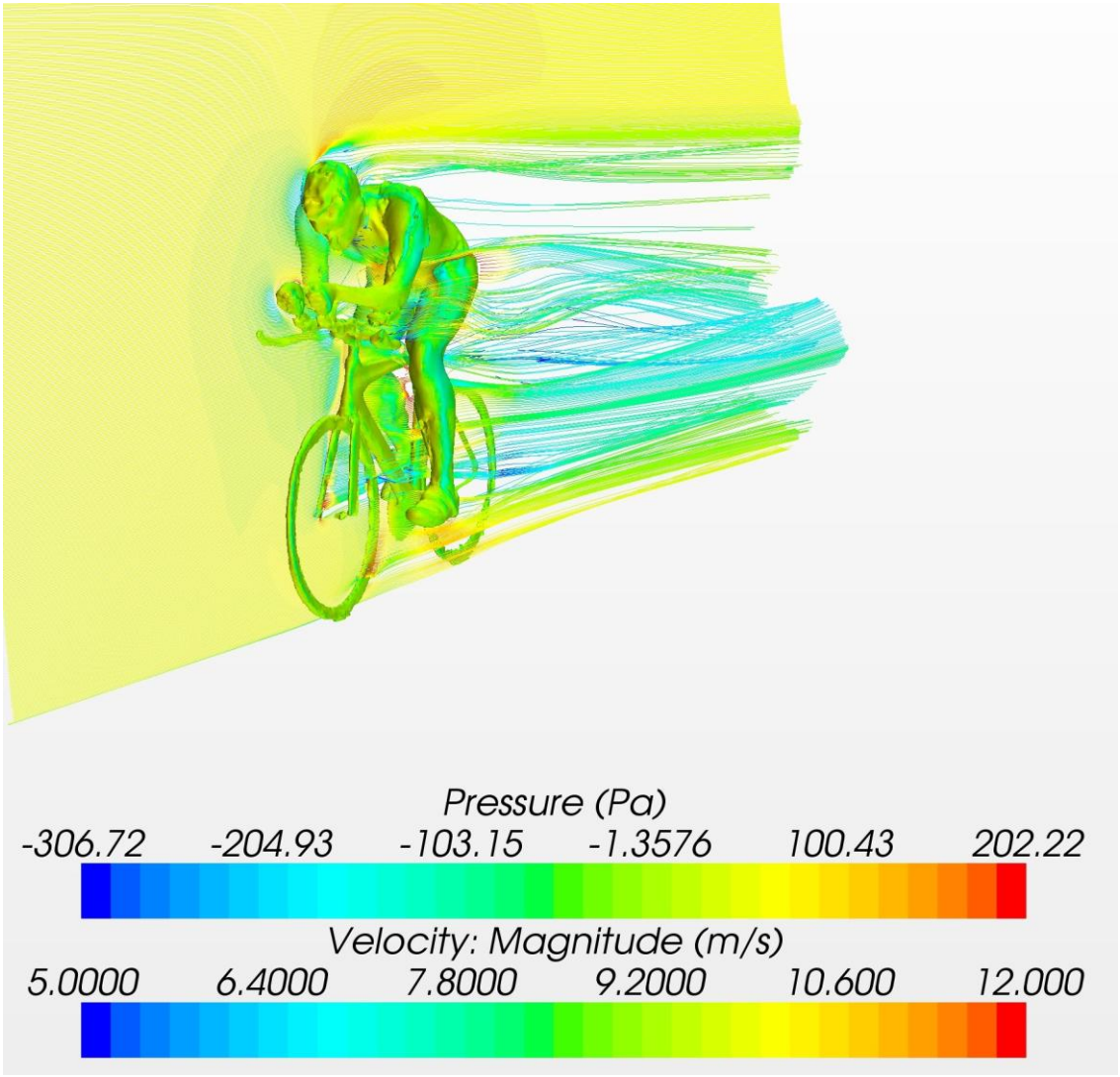

Figure 4 – Velocity and Pressure Profile of a Rider (Symmetric Posture)

2.1.1 VERIFICATION

In order to determine whether or not a specific CFD simulation accurately represents results that would be found through experimentation, it is often useful to perform a similar simulation on a simple object. In this case, a simple sphere

was modeled in similar flow to the bicycle and rider model to better understand the accuracy of the setup. Results from the sphere simulation yielded a drag coefficient of 0.18. When compared to easily accessible experimental data, this drag coefficient is within acceptable range of the true value: approx. 0.2 (Cengel & Cimbala, 2010).

2.1.2 SYMMETRIC POSTURE

First, the symmetric rider posture at different yaw angles was simulated as a baseline.

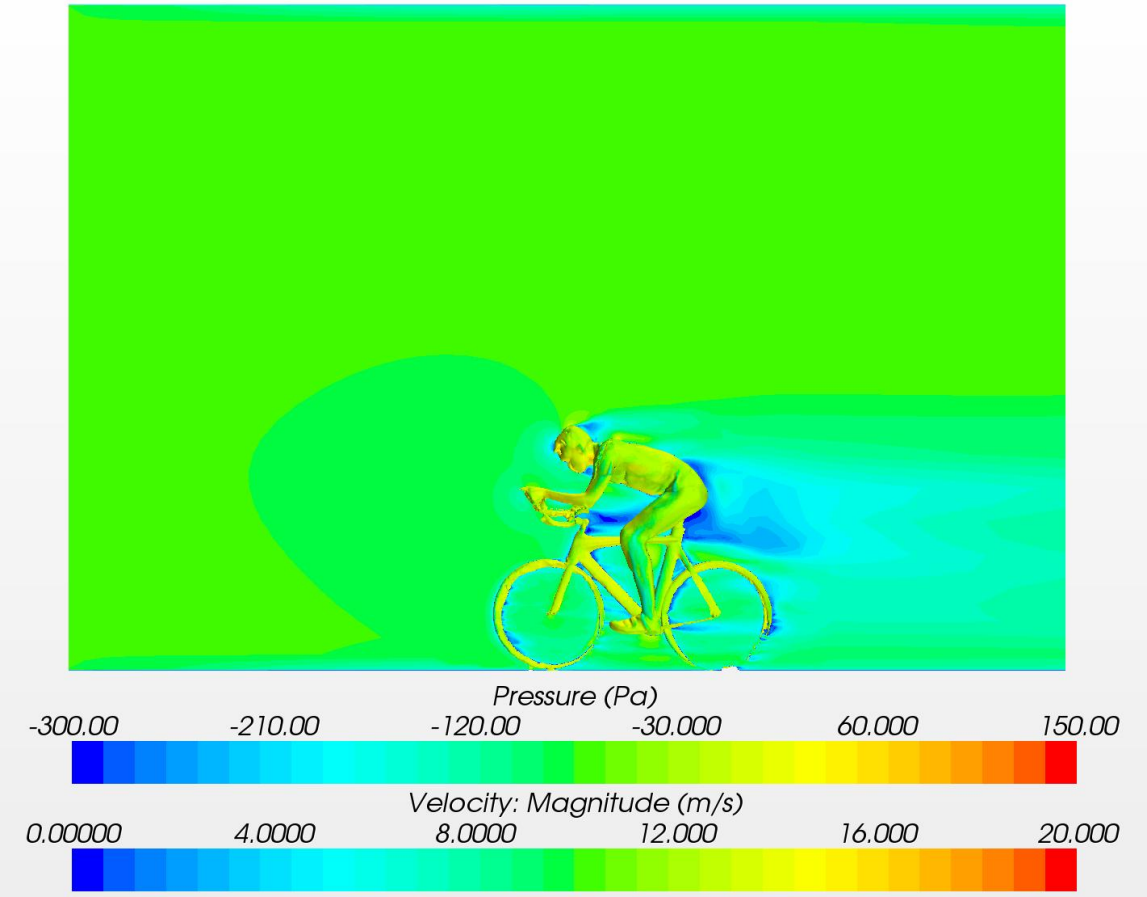

Figure 5 - Velocity Profile & Surface Pressure (Symmetric Posture, 0° Yaw)

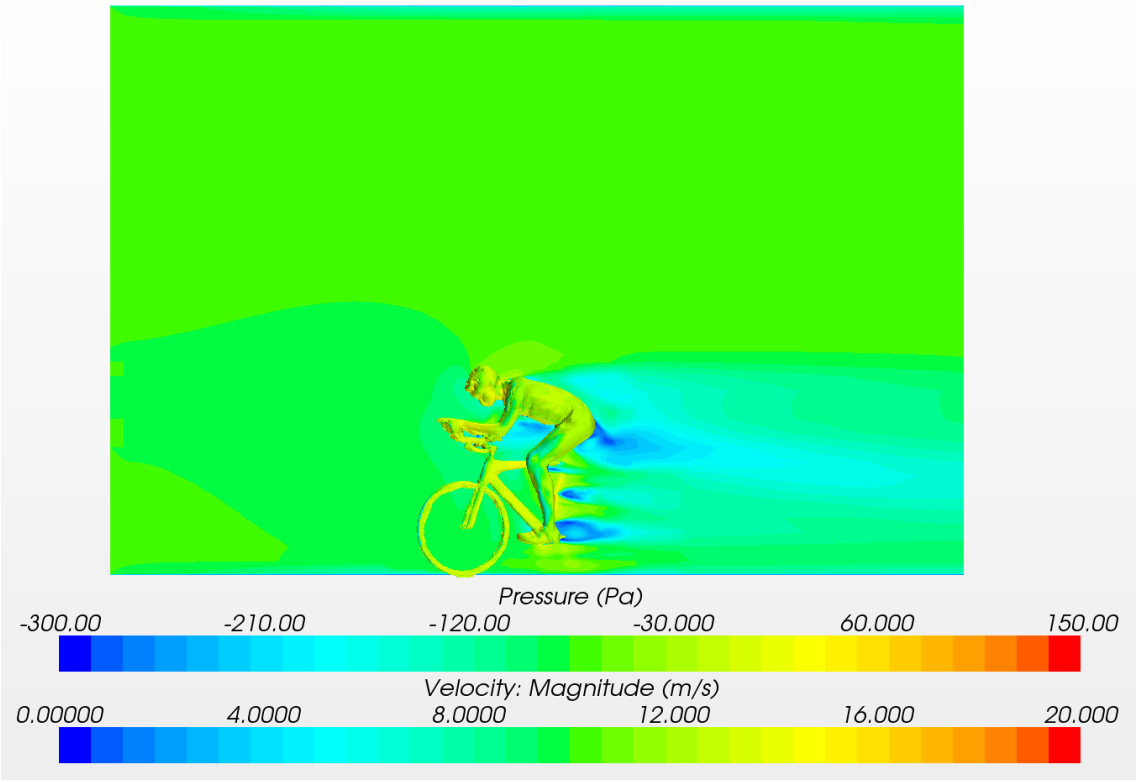

Figure 6 – Velocity Profile & Surface Pressure (Symmetric Posture, 15° Yaw)

The 0° yaw configuration of the symmetric riding position (Figure 5) showed lower drag coefficient than the asymmetric position. When rotated to a 15° yaw angle (Figure 6) the symmetric riding position experienced a roughly 4% increase in drag coefficient as shown in Table 1, surpassing the drag coefficient of the asymmetric position at the same yaw angle.

2.1.3 ASYMMETRIC POSTURE

Secondly, the asymmetric posture at various yaw angles was analyzed.

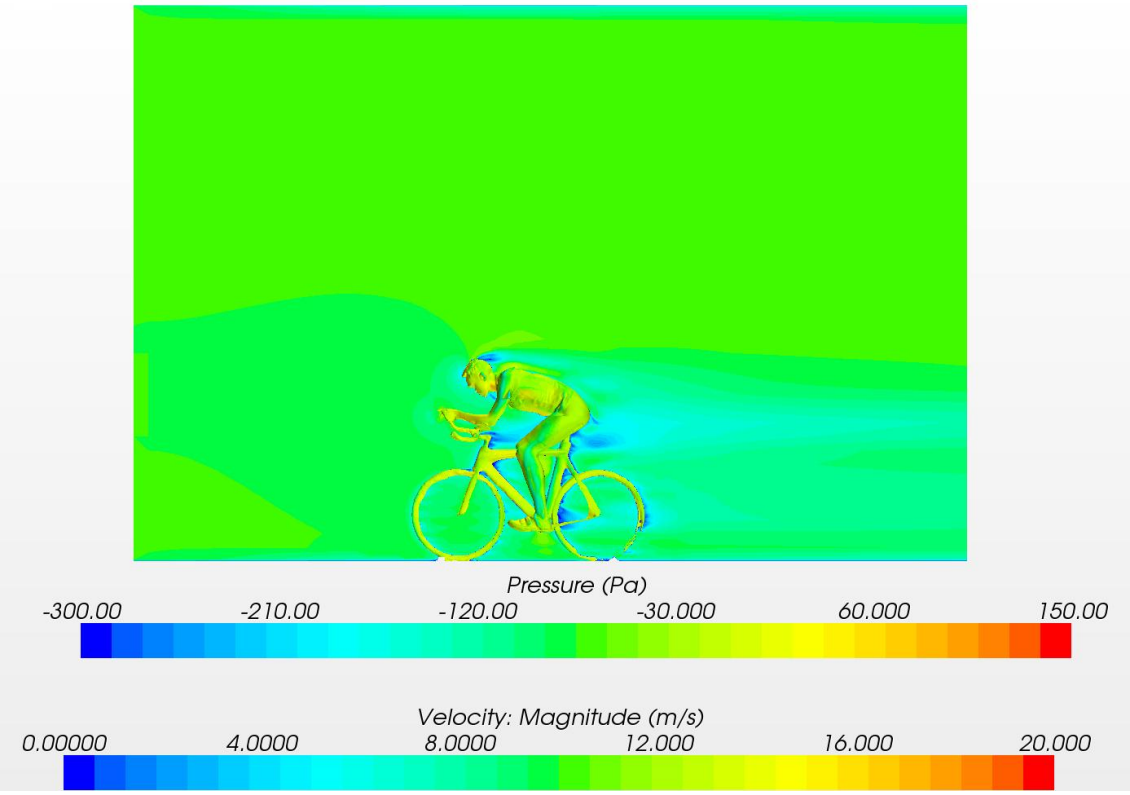

Figure 7 – Velocity Profile & Surface Pressure (Asymmetric Posture, 0° Yaw)

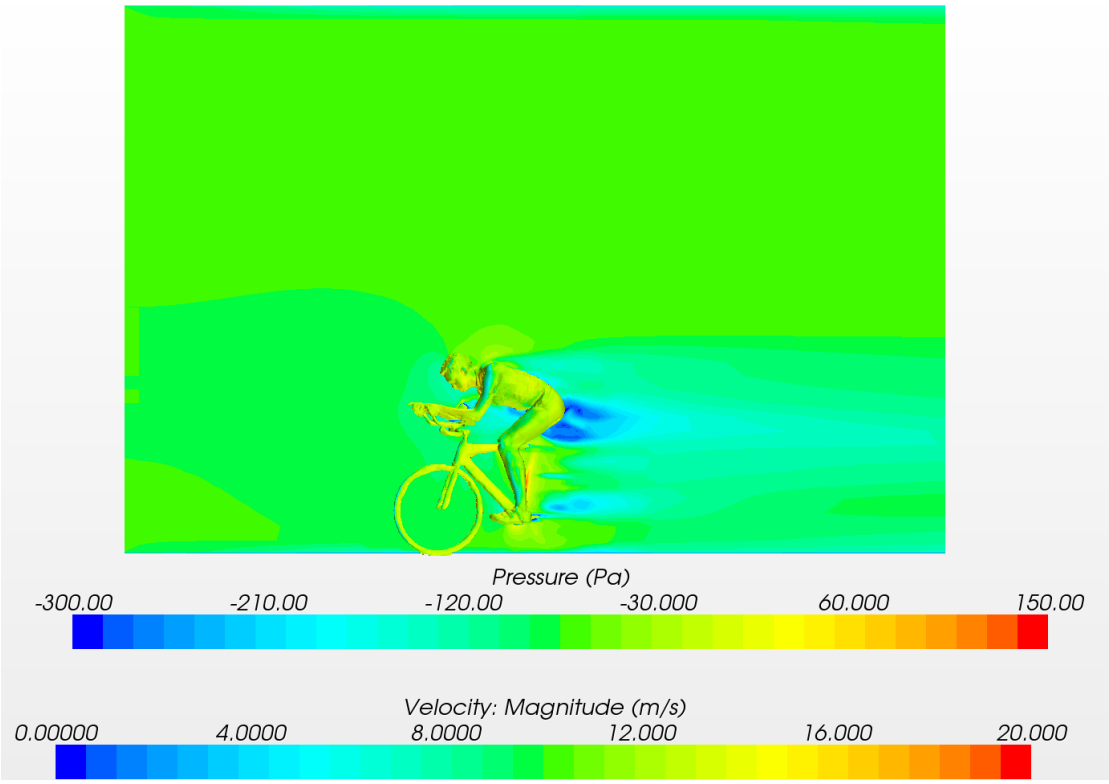

Figure 8 – Velocity Profile & Surface Pressure (Asymmetric Posture, 15° Yaw)

The asymmetric riding position, Figure 7 and Figure 8, showed higher drag than the symmetric position in the 0° yaw angle case but produced lower drag than the symmetric position at 15° yaw. This represents the desired and theorized result. As seen in Table 2, the drag coefficient initially decreased when the yaw angle was increased for the asymmetric position while the symmetric position produced increasing drag coefficient values for increasing yaw angles. It can also be seen that the rate of increase in drag with increase in yaw angle is greater for the symmetric position.

Table 1 – Drag Coefficient (FEA) for Symmetric Riding Position at Differing Yaw Angles

	Symmetric Posture (Baseline)		
Yaw	Drag Coefficient	% Increase from 0° Yaw	Number of Elements
-45°	0.7730	45.7	6,051,616
-30°	0.6286	18.5	5,983,202
-15°	0.5634	6.19	8,216,678
-10°	0.5651	6.52	5,942,410
0°	0.5306	0.00	5,912,338
10°	0.5333	0.52	5,909,950
15°	0.5507	3.80	5,905,791
30°	0.6817	28.5	5,987,493
45°	0.7445	40.3	6,054,895

Table 2 – Drag Coefficient (FEA) for Asymmetric Riding Position at Differing Yaw Angles

	Asymmetric Posture (Offset)		
Yaw	Drag Coefficient	% Increase from 0° Yaw	Number of Elements
-45°	0.6681	22.8	5,692,171
-30°	0.5788	6.41	5,678,536
-15°	0.5385	-0.99	5,605,316
-10°	0.5443	0.08	5,598,824
0°	0.5439	0.00	5,584,986
10°	0.5415	-0.44	5,603,489
15°	0.5118	-5.90	5,606,206
30°	0.6143	13.0	5,692,693
45°	0.6866	26.2	5,730,578

2.2 CONCLUSIONS

Initial CFD results seem very promising. When comparing drag coefficients of each riding position, the results uphold the theory. It was assumed that the asymmetric riding position would produce lower drag at any significant yaw angle. As the 10° angle was tried initially, the results were different than expected. This can be seen in Table 1 and Table 2, where the symmetric riding position produced a lower drag coefficient than the asymmetric position. However, after continuing iterations at other yaw angles, the desired results

became apparent. When looking at the change in drag coefficient of each position at different yaw angles, the desired trend is easily seen. As the yaw angle is increased, the asymmetric riding position produces a decreasing drag coefficient initially and then slowly increases with yaw angle. The drag coefficient of the symmetric riding position immediately increases with yaw angle and increases at a greater rate than the asymmetric position. This trend outlined in the results section gives justification to continue investigation of the theory. Further work refining the 3-D models of each riding position is recommended to reduce any inconsistencies beyond posture changes. It is also desired to further investigate additional yaw angles to determine maximum drag reduction for a given asymmetric posture. This could eventually be used to fine tune a rider's posture given the current wind trajectory.

Complete validation of the results of this experiment would warrant a wind tunnel test. Available at UW-Milwaukee is a wind tunnel with 4x4ft cross-section. To run a similar test in this wind tunnel, a scaled model of rider and bicycle would need to be built (rapid-prototyped). A small-scale model should yield useable comparison results if scale-sensitive factors like fluid density and velocity are adjusted from full to small scale models (Hucho, 1998). The work accomplished so far during this project has yielded promising results and has brought attention to areas needing improvement.

2.3 REVISED STUDY

The second study on this topic began with the same 3-D scanning equipment, Konica Minolta VIVID 910, but a new bicycle and rider were used as well as a slightly improved procedure. The bicycle used for this study was a Giant TCR 2 equipped with Tec9 Triathlon Aero Time-Trial clip-on handlebars. In addition to the new bicycle and rider, a Specialized TT2 Aero Helmet was used to further match a time-trial bicycle race setup. It was desired that this study include more than one alternative riding position to the symmetric position. Therefore, three riding positions were scanned – a symmetric position (Figure 9) where the handlebars were both adjusted evenly in the fore-aft direction, an extreme position (Figure 10) where the left handlebar was adjusted in the fully aft position while the right was adjusted fully forward (160mm difference from left hand to right hand in the fore-aft direction), and a middle position (Figure 11) which was a midpoint between the two previous positions.

Figure 9 – Symmetric Position

Figure 10 – Extreme Position

Figure 11 – Mid Position

Initially, it was desired to utilize a motorized turntable, which was interfaced with the PET software to capture the 3-D images. The turntable is controlled through the software and eases the scanning process greatly by automatically indexing by a specified angle between each scan. After a full revolution is completed, the images are registered to one another based on a calibration chart. This process allows an object to be scanned from 0-360 degrees and the images then assembled with the correct angle offset. An initial problem encountered in this process was the modification of the turntable to support the weight of the bicycle and rider. The supplied motor proved too weak and frequently failed to spin the rider the desired degree increment. The next issue with the implementation of the turntable procedure was the focal range of the scanner. In

order to capture the entire bicycle and rider in one frame, the scanner would have to be placed more than 3 meters away from the subject. Through experimentation and the provided documentation from Konica Minolta, it was discovered that the surface quality of the scan is not sufficient at this distance. Based on the two main issues above, it was decided to abandon the use of a turntable and simply move the scanner to the desired locations around the subject. Afterward, the images could be aligned and merged.

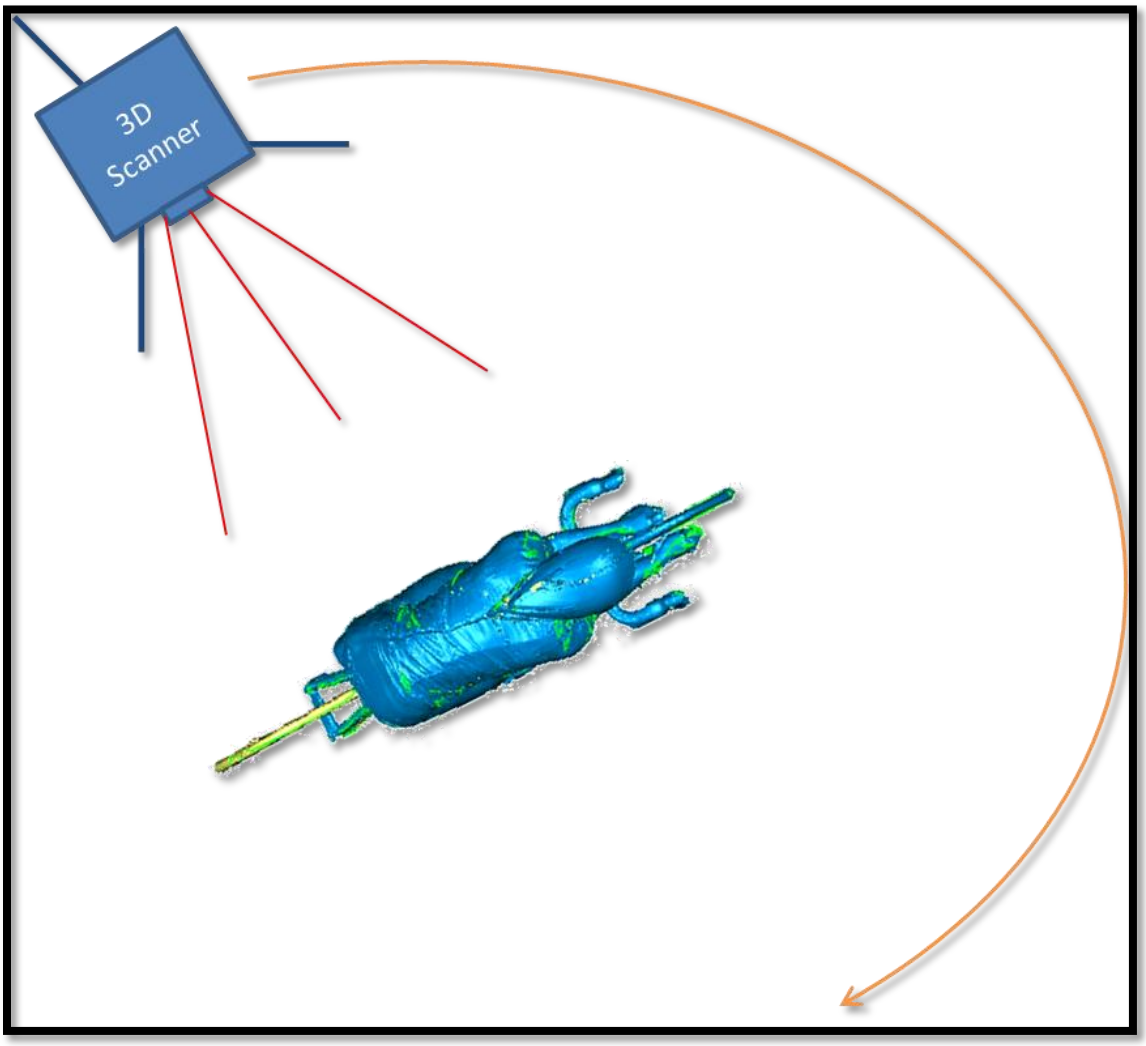

Figure 12 – 3-D Scanning Procedure

With the practice and knowledge from the pilot study, it was assumed that a better model could be created this time. During the scanning process of the pilot study, the rider dismounted several times between scans to relocate the bicycle when a scan from a new angle was desired. For the second study, the rider and bicycle were kept in the same position and the scanner was moved to each location needed to obtain a complete scan (Figure 12). This method seemed to produce a better model that was easier to assemble from the group of separate 3-D images. Using Geomagic once again to assemble the images, each model, consisting of approximately 60 3-D images, was assembled to create a closed 3-D surface. The separate scans, which were assembled into larger portions of the overall model, are shown in Figure 13, Figure 15, Figure 17, Figure 19, and Figure 21. These larger sections are displayed in Figure 14, Figure 16, Figure 18, Figure 20, and Figure 22. Finally, the larger sections of the model were aligned and merged to create the final 3-D model of the rider-bicycle system, seen in Figure 23. The capturing of the different handlebar positions can also be seen in Figure 24, Figure 25, and Figure 26. Significant time was still necessary to clean up the surfaces, remove noise, fill holes and delete small details which could result in high computational effort during CFD analysis. Those detailed areas included the spokes of the wheels and the brake and shifting cables on the bicycle. Once complete, the 3 models were exported from Geomagic in STL format and imported into Star-CCM+ to begin setup for the CFD analysis.

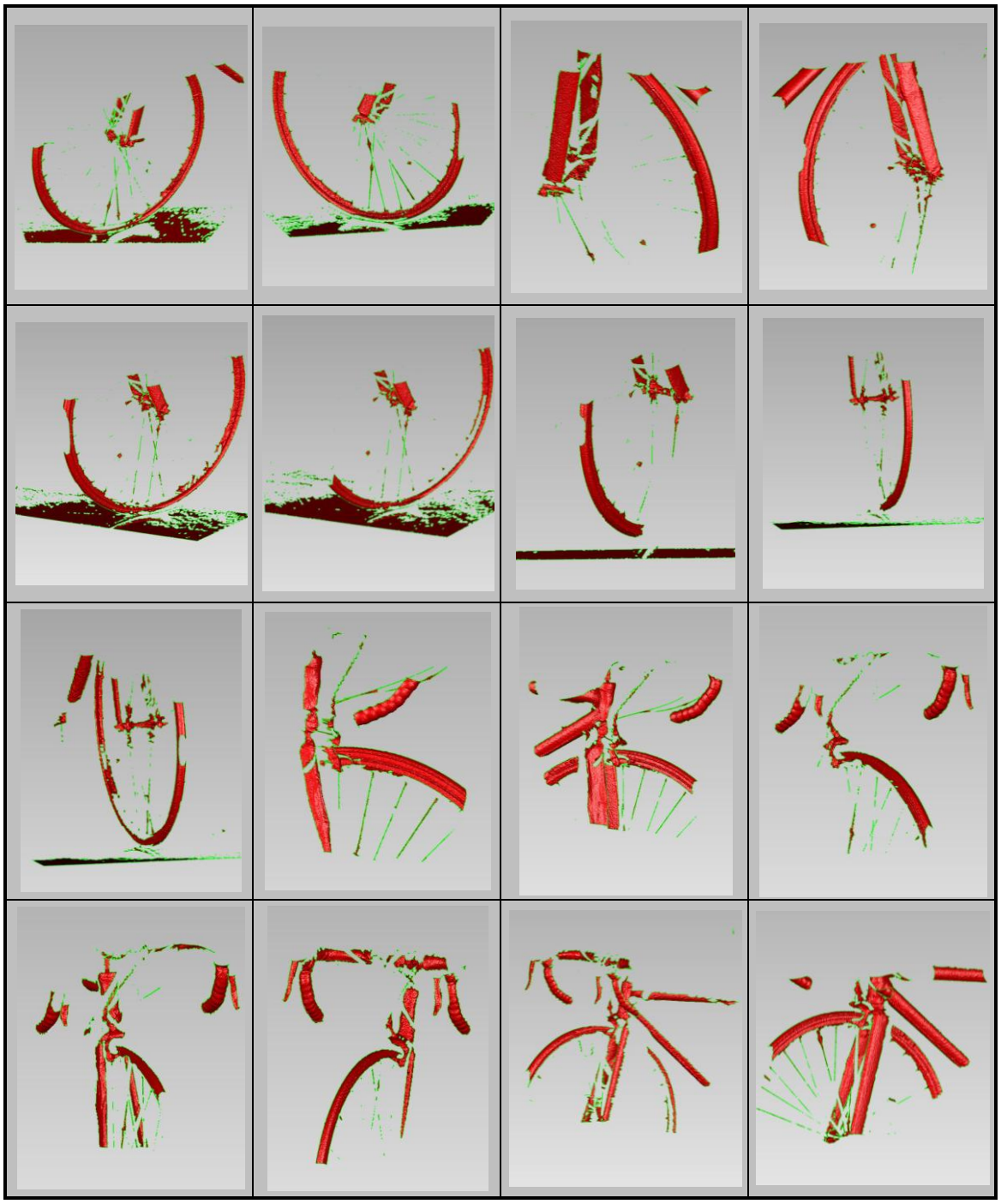

Figure 13 – Single Scans of Front Wheel

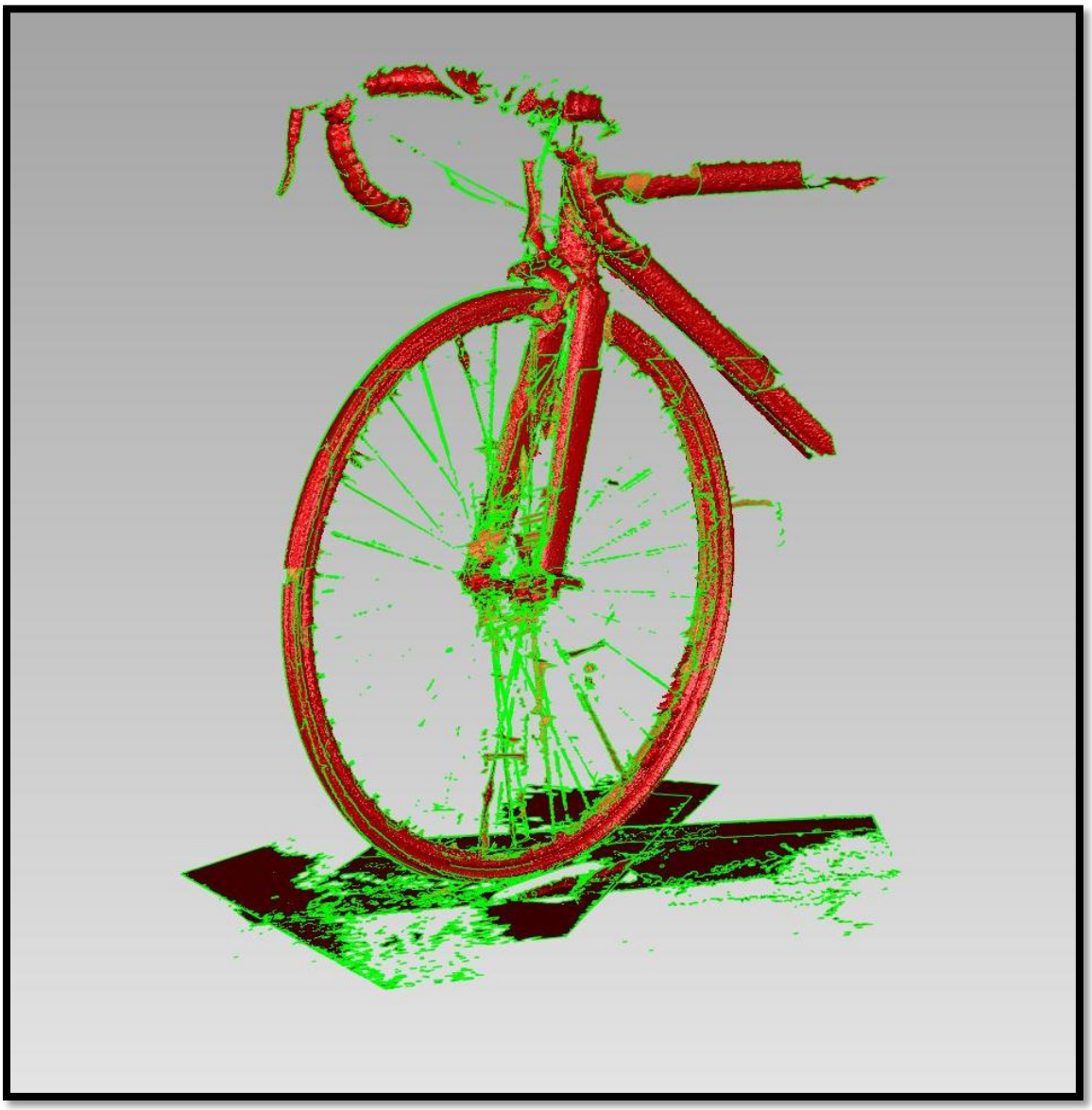

Figure 14 – Assembled Scans of Front Wheel

Figure 15 – Single Scans of Lower Portion of Bicycle

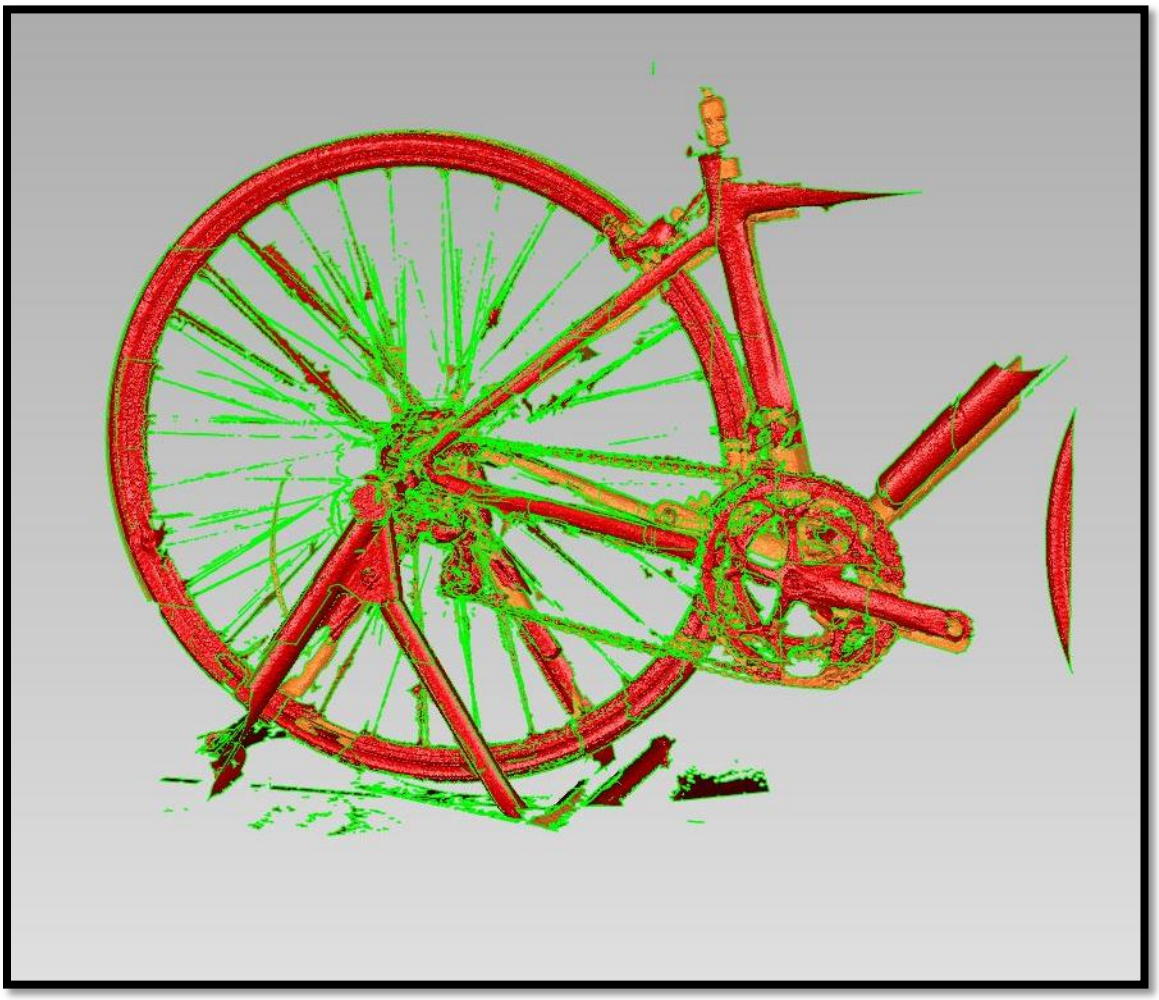

Figure 16 – Assembled Scans of Lower Portion of Bicycle

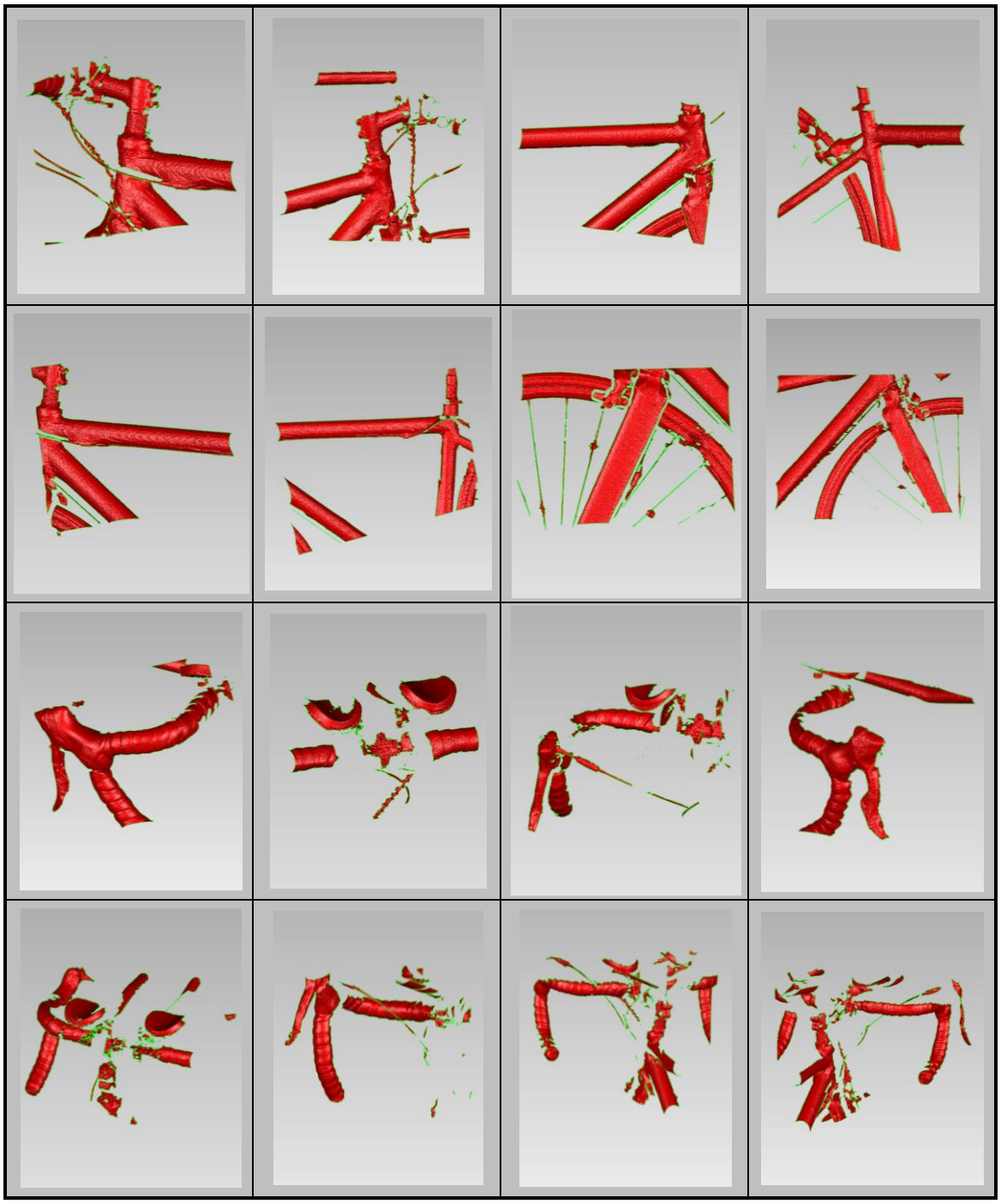

Figure 17 – Single Scans of Upper Portion of Bicycle

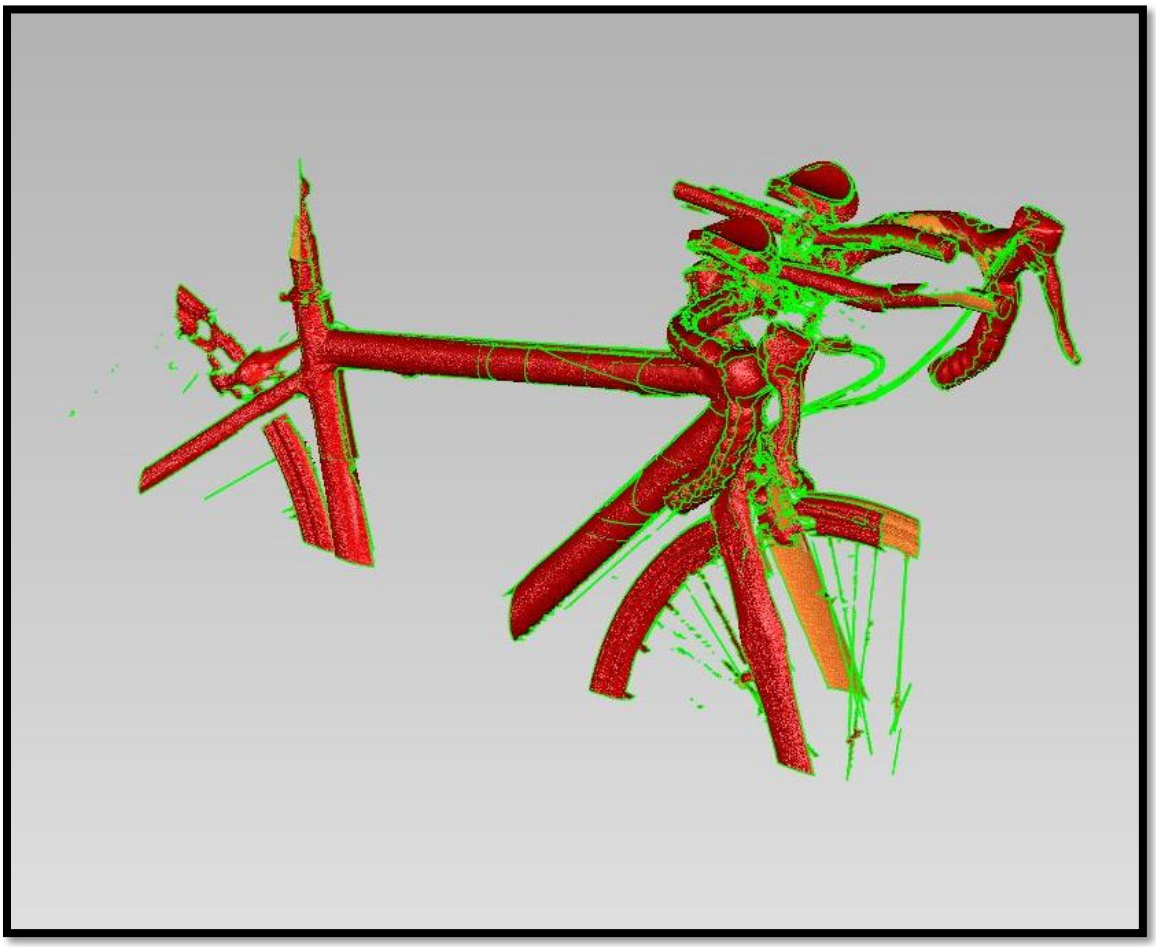

Figure 18 – Assembled Scans of Upper Portion of Bicycle

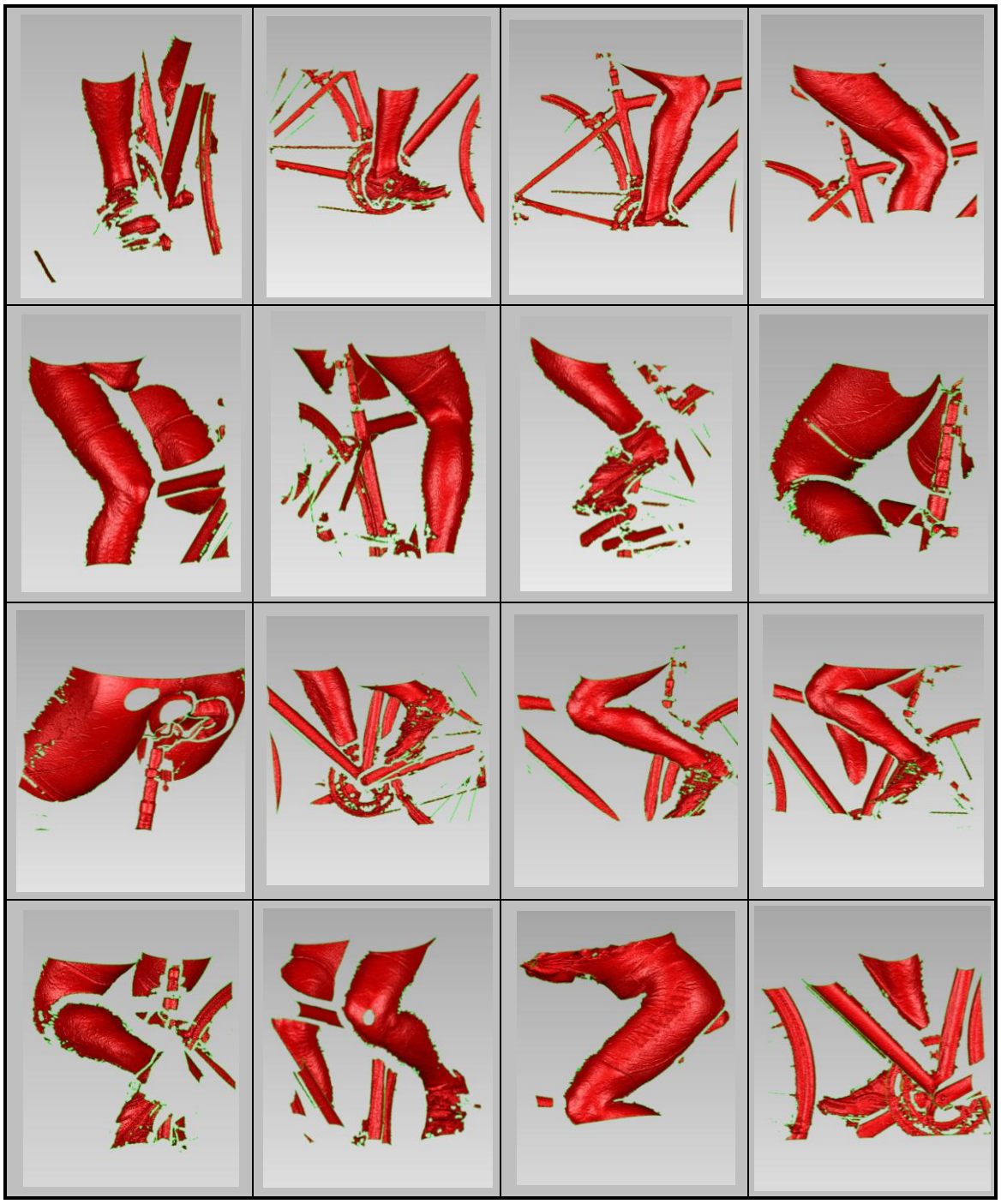

Figure 19 – Single Scans of Lower Portion of Rider

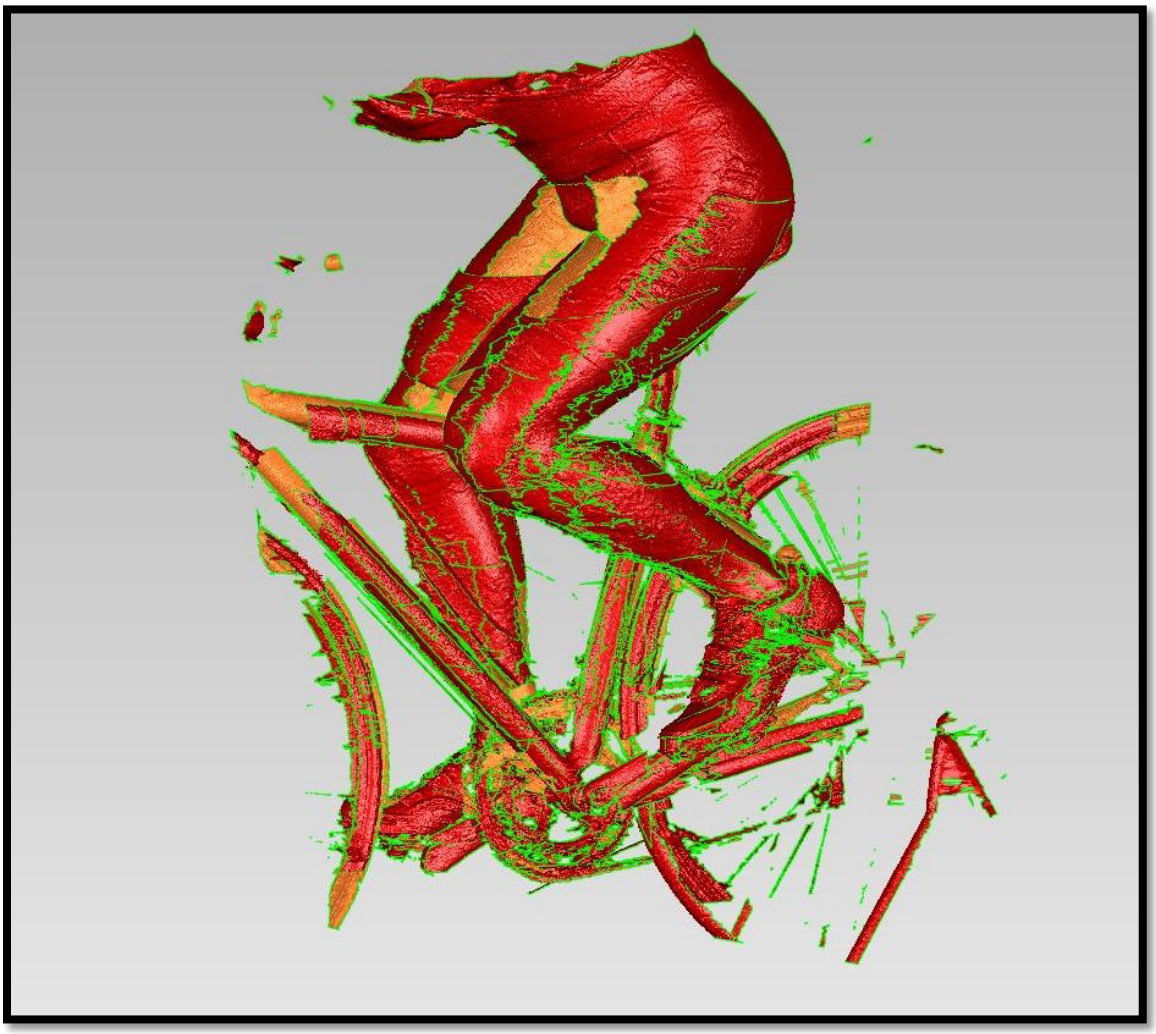

Figure 20 – Assembled Scans of Lower Portion of Rider

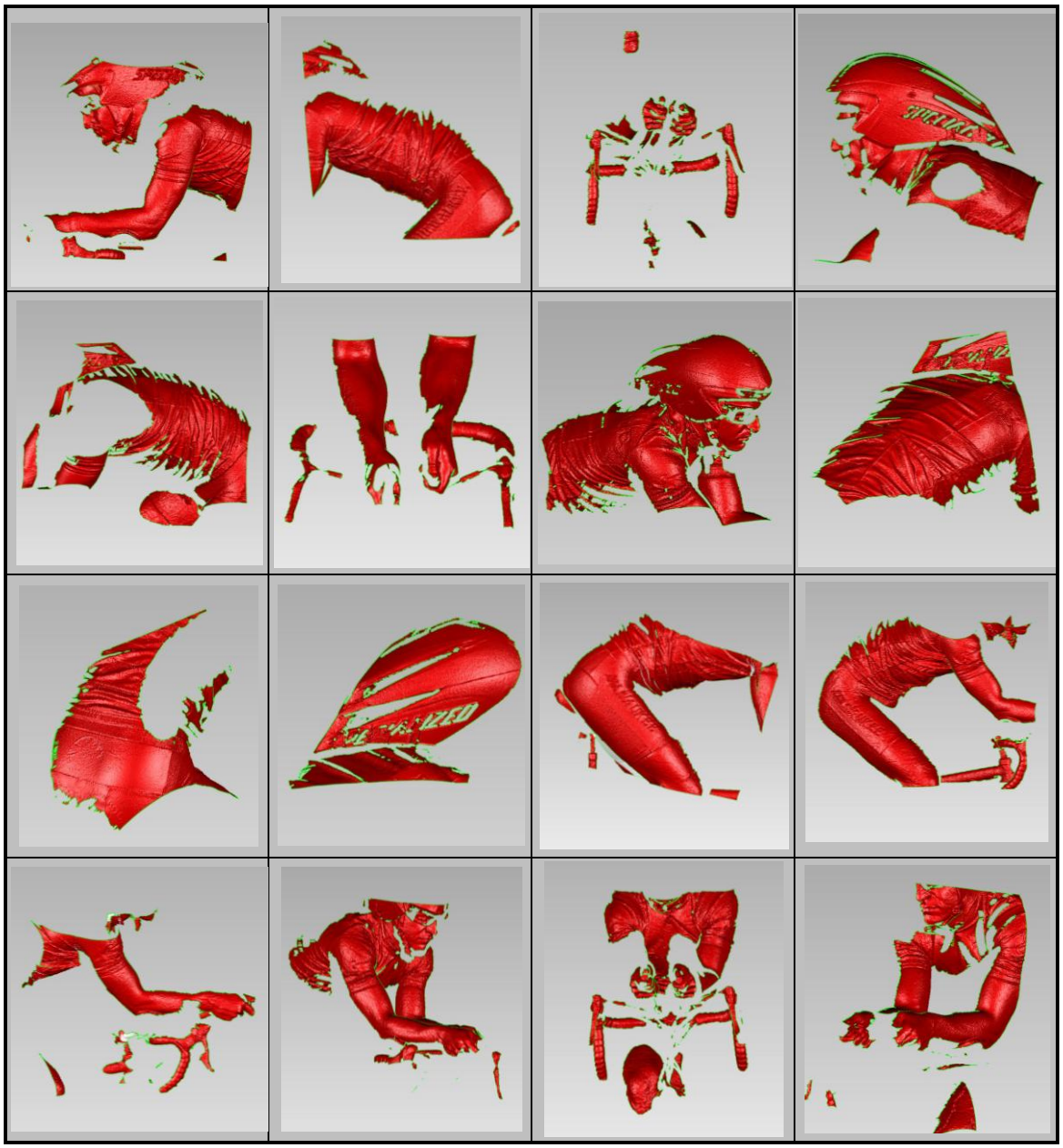

Figure 21 – Single Scans of Upper Body of Rider

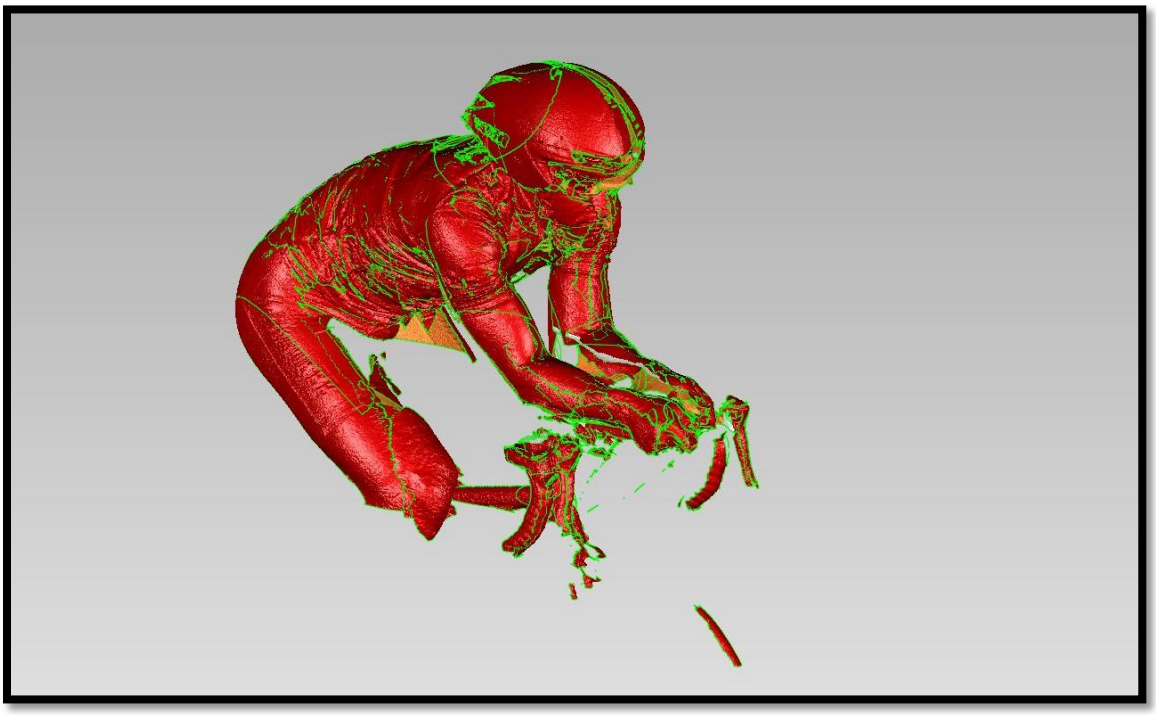

Figure 22 – Assembled Scans of Upper Body of Rider

Figure 23 – Final Assembled Scan of Rider and Bicycle (After Significant Smoothing and Filling of Holes)

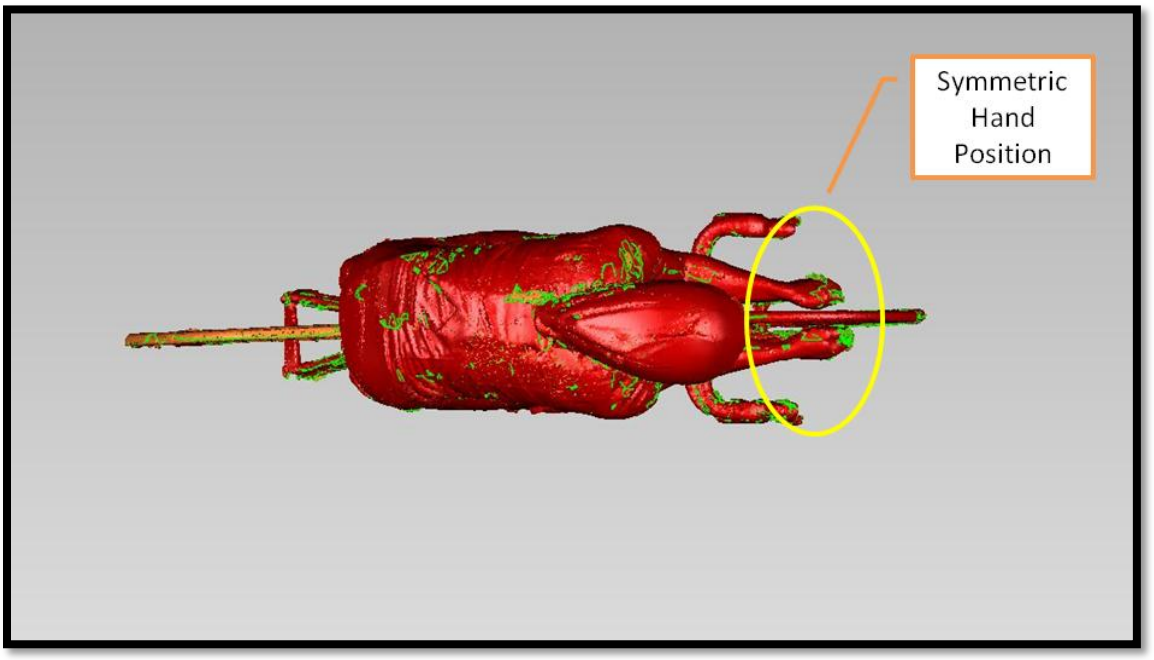

Figure 24 – Top View of Symmetric Hand Position

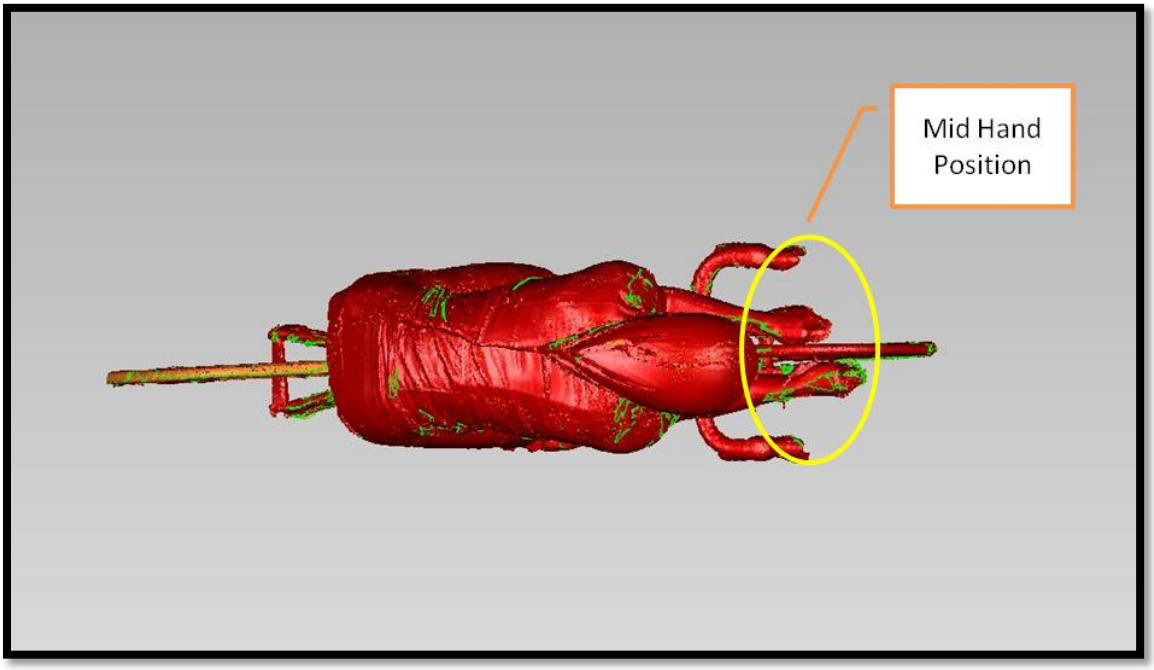

Figure 25 – Top View of Mid Hand Position

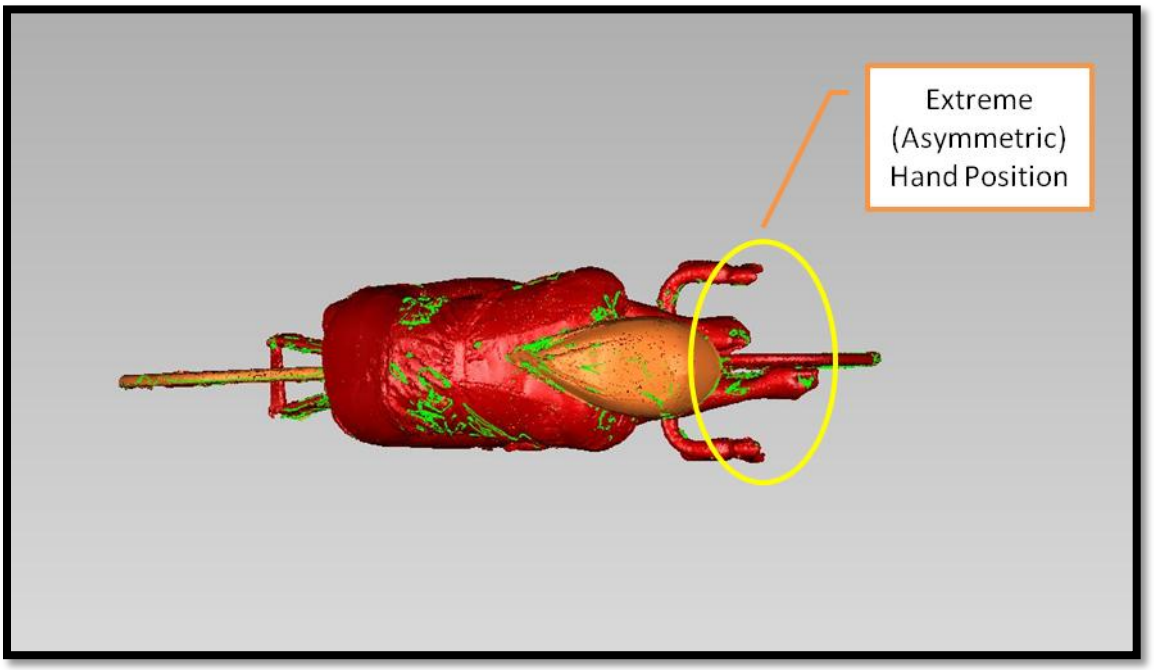

Figure 26 – Top View of Extreme Hand Position

The simulations from the pilot study were a starting point for the setup of the new models. Since no specific wind tunnel tests were planned for correlation to this study, the setup of the simulations was altered to better represent real-world conditions. For this reason, the test section was expanded to a size of 12m in length, 6m in width, and 4.75m in height. Slip condition was also applied to all walls of the test section to lessen the effects of the boundaries on the model. Through initial test runs, it did not seem that the boundaries were affecting the solution at the surface of the bicycle and rider model. The number of prism layers used on the surface of the bicycle and rider was raised from 4 – 6 in an attempt to better resolve the boundary layer. The above parameters yielded a volume cell count in the range of 2,150,000 cells for each configuration. This volume mesh

can be seen in Figure 27, which also illustrates the varying mesh size throughout the fluid region. Further detailed views of the mesh near the rider-bicycle boundary are shown in Figure 28, Figure 29, and Figure 30, the latter showing the layout of the prism layer cells on the surface of the helmet.

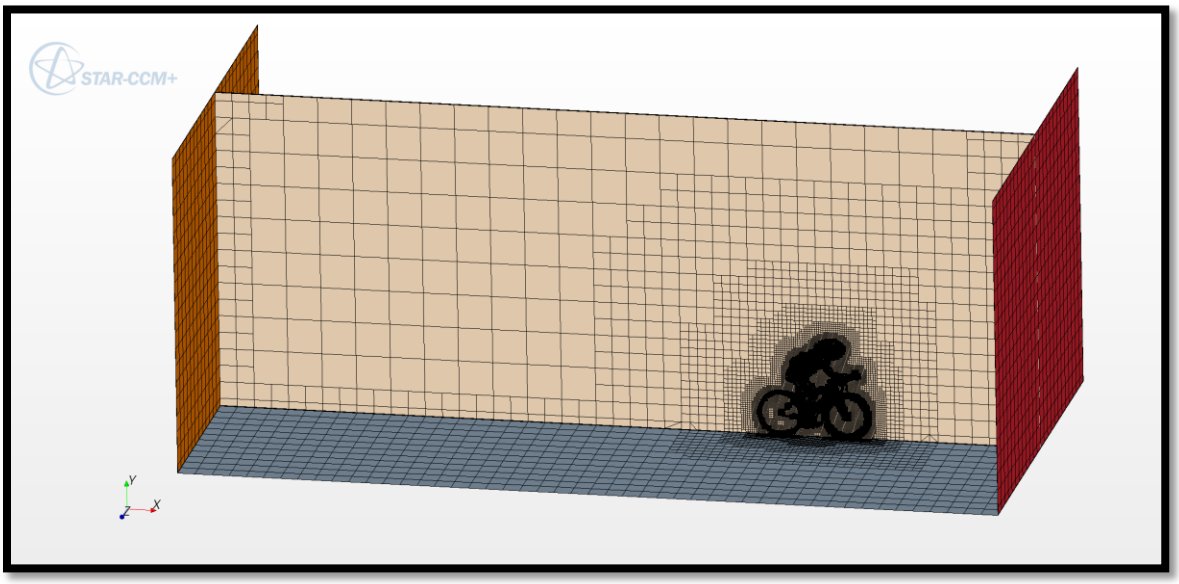

Figure 27 – Fluid Region Volume Mesh

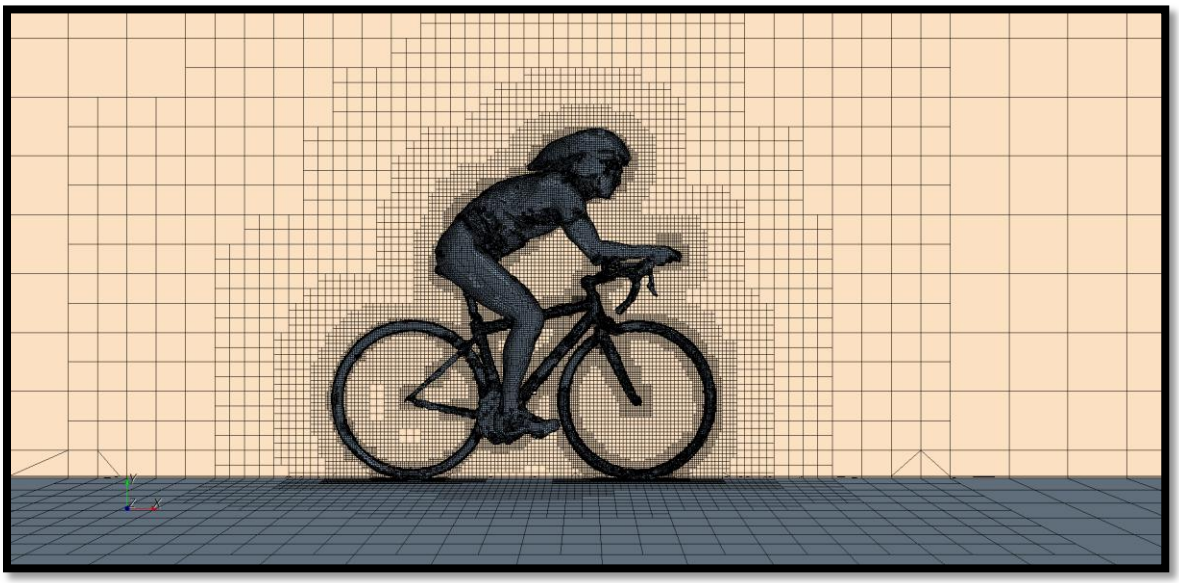

Figure 28 – Fluid Region Volume Mesh – Rider Detail

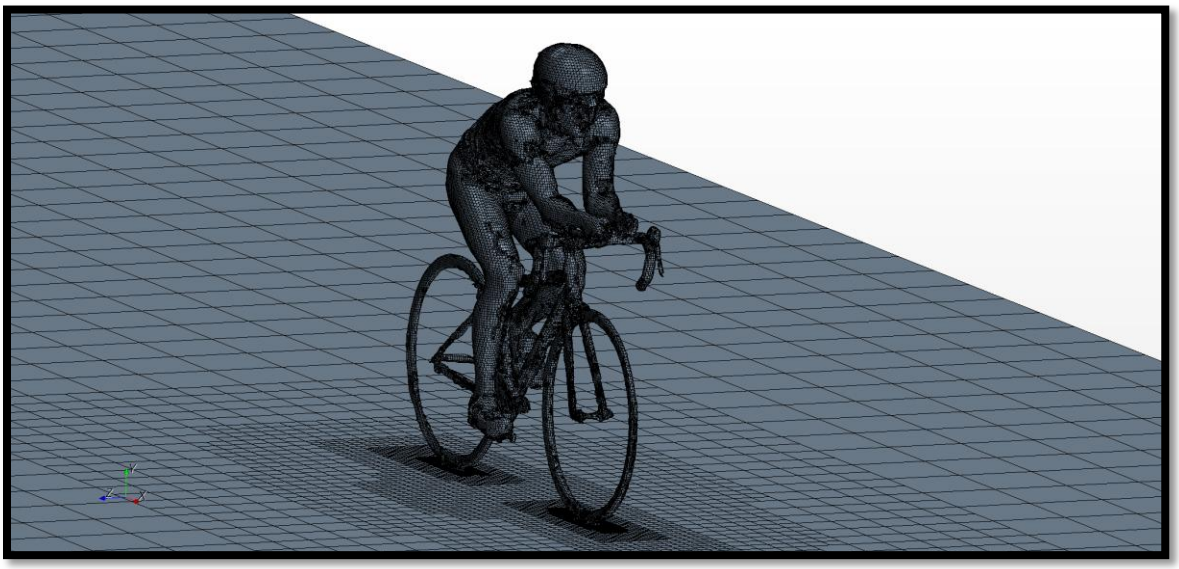

Figure 29 – Fluid Region Volume Mesh - Rider Iso View

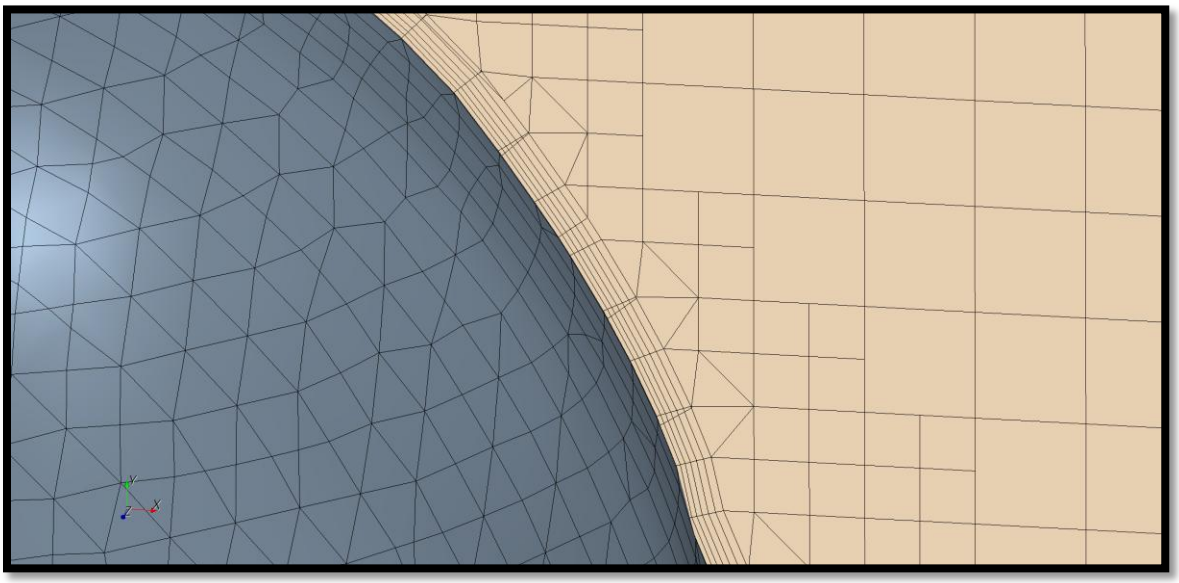

Figure 30 – Fluid Region Volume Mesh – Prism Layer Detail

As no significant conclusions were drawn from using symmetric yaw angles (-45° to +45°) during the pilot study, it was decided to use only angles in the positive direction (CCW rotation of the rider and bicycle). As experimental data shows wind yaw angles normally do not exceed 10° at a race pace, it was decided to narrow the studied range of yaw angles to capture data at every 2.5° interval from 0° to 15°.

3 RESULTS

3.1 VERIFICATION

Once again, as was the case for the pilot study, it was desired to run a simplified CFD simulation to gauge the accuracy of the model setup. In this case, a cone was chosen as the simple shape to use in place of the scanned rider-bicycle

model. Experimental data from text was referenced and used as comparison for this simulation. Using identical meshing parameters while replacing the rider-bicycle model with a cone of comparable frontal area, the fluid region was meshed with only 50,000 volume cells (Figure 31). This simply means the software needed significantly less fine cells to obtain the same surface mesh fidelity.

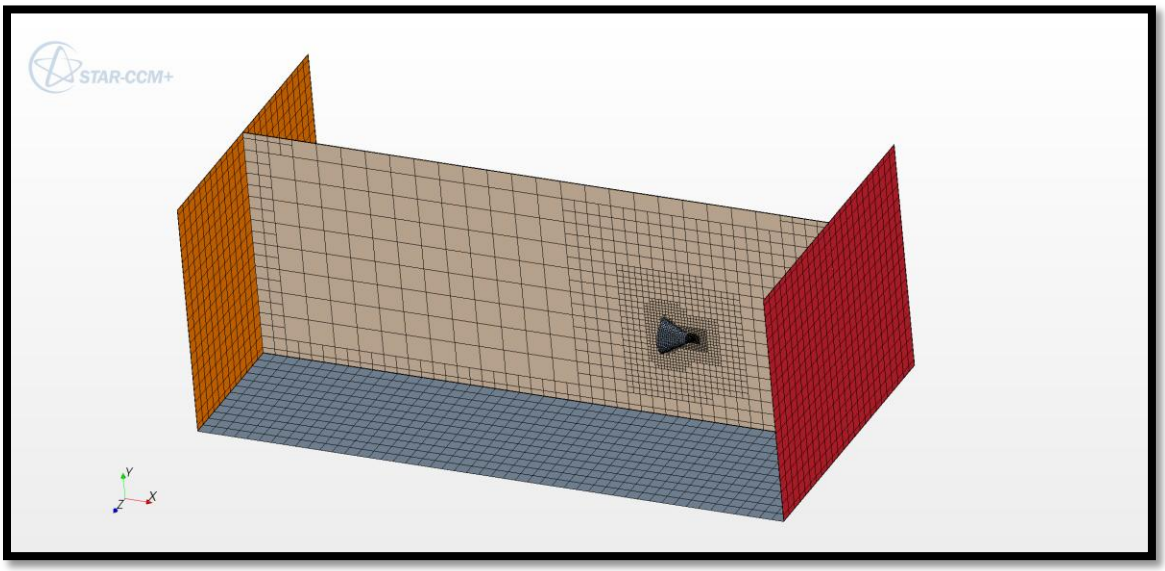

Figure 31 – Fluid Region Volume Mesh of Cone

This initial mesh was run and yielded a drag coefficient of 0.67, which is a significant error from the true value of 0.5 (Cengel & Cimbala, 2010). A second mesh of the cone model was then created, this time making some simple mesh refinements. The surface cell size of the cone was reduced to a range of 1-10mm and the mesh was also refined in the wake region behind the cone, since there are

more significant pressure changes in this case than with the rider-bicycle system. These refinements yielded a volume mesh cell count of nearly 600,000.

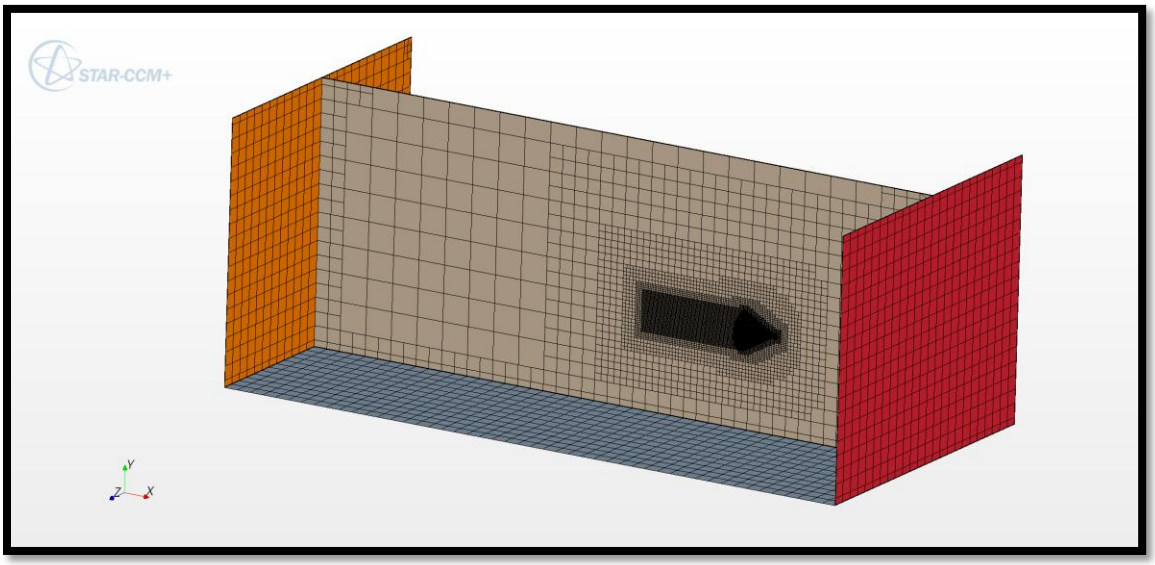

Figure 32 – Refined Fluid Region Volume Mesh of Cone

The following simulation then yielded a drag coefficient of 0.56, a much smaller error when compared to the true value of 0.5. These results lead to some concerns regarding the mesh sensitivity of the rider-bicycle model. This issue was briefly addressed, within the computing limits available, and is discussed in the following section.

3.2 MESH SENSITIVITY

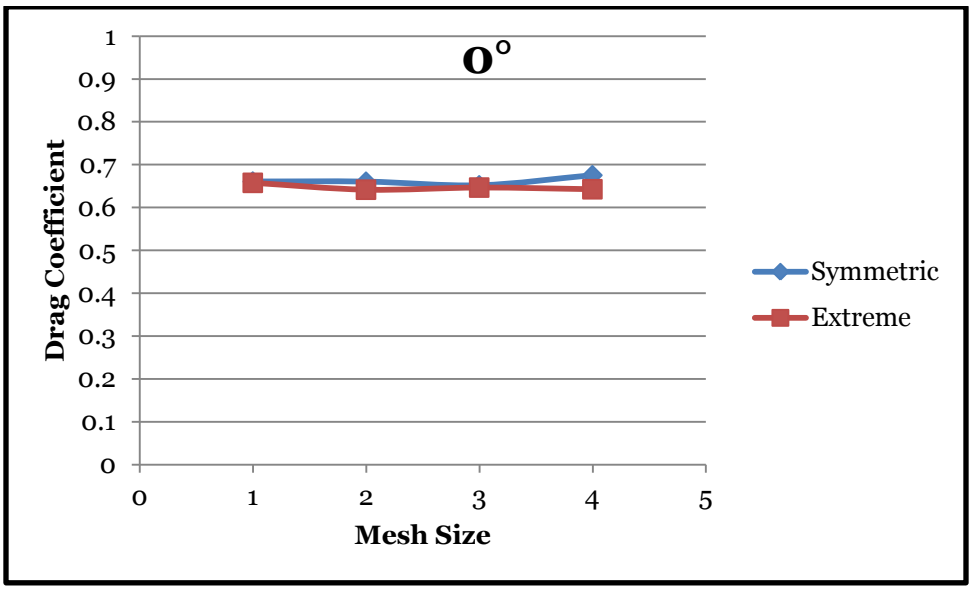

Figure 33 – Mesh Sensitivity at 0°

Table 3 – Mesh Sensitivity Data Points at 0°

Mesh Sensitivity	Cell Count	500,000	900,000	1,100,000	2,200,000
Position	Symmetric	0.660509	0.660245	0.651767	0.67528
	Extreme	0.65762	0.641606	0.646584	0.642668

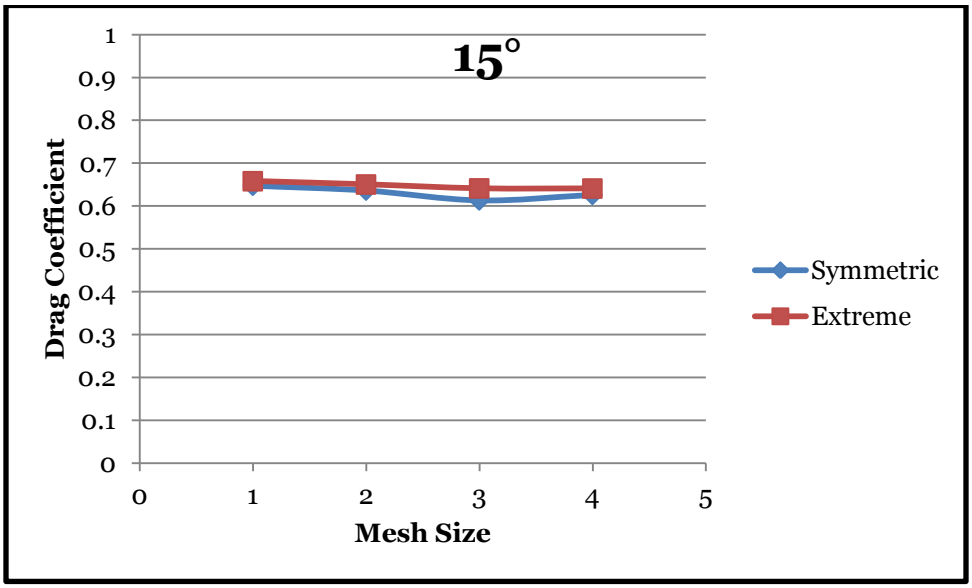

Figure 34 – Mesh Sensitivity at 15°

Table 4 – Mesh Sensitivity Data Points at 15°

Mesh Sensitivity	Cell Count	500,000	900,000	1,100,000	2,200,000
Position	Symmetric	0.647572	0.636368	0.613382	0.62622
	Extreme	0.658195	0.650528	0.641347	0.641113

To better understand the sensitivity of the solution to mesh size, the symmetric and extreme position models were further evaluated at 0° and 15° with varied volume mesh sizes. The mid position was omitted to simplify this step. Considering the constraints in computing resources, only models with a coarser mesh than the model used for the full analysis were created to evaluate mesh sensitivity. Based on the data displayed in Figure 33 and Table 3, it can be said that the drag coefficient solution at 0° is not highly sensitive to mesh size. This conclusion is upheld when the data Figure 34 and Table 4 is considered,

where yaw angle is at 15°. Based on these findings, it was determined that the mesh size chosen for analysis was sufficient.

3.3 RIDER – BICYCLE MODEL

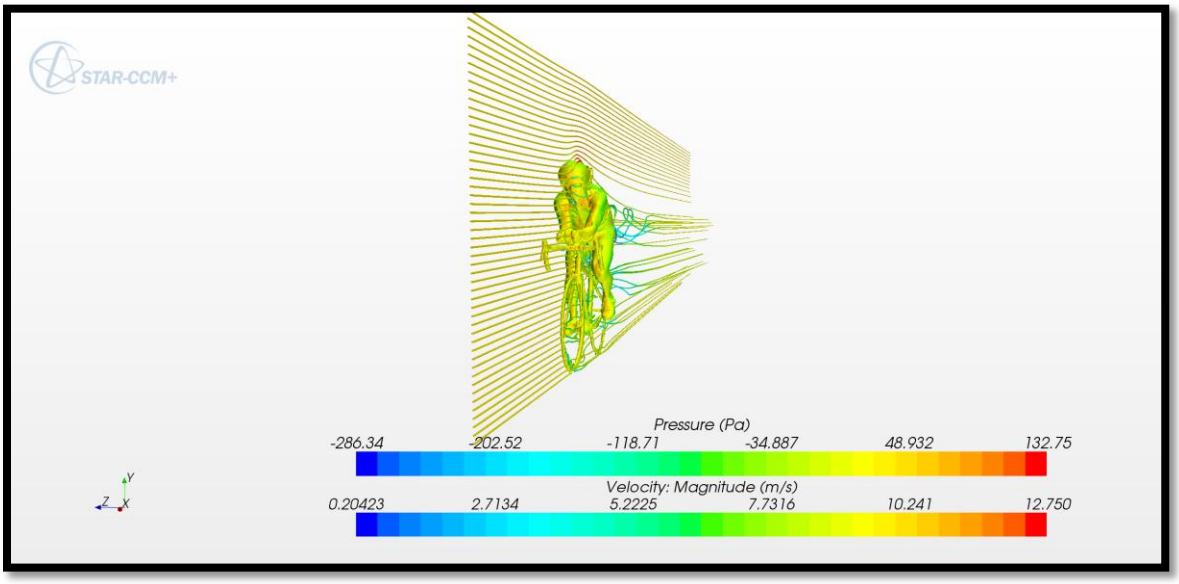

Figure 35 – Solution Plot for Symmetric Position at 0° Yaw

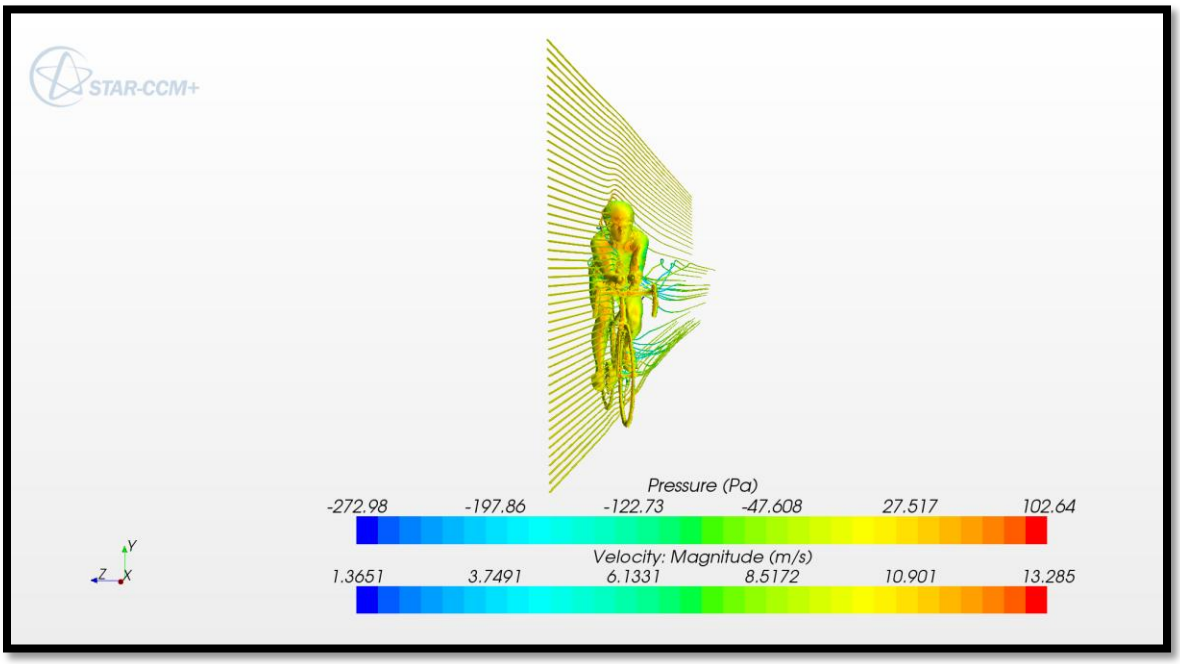

Figure 36 – Solution Plot for Symmetric Position at 15° Yaw

Figure 35 and Figure 36 were included to help illustrate the difference between the 0° yaw angle and the 15° yaw angle configurations. The streamlines show how the fluid flows over the surface of the model while the pressure plot on the surface of the rider can show where significant pressure drag is being created. Below, in Figure 37, a comparison of drag coefficients for the entire data set is shown. Based on this table, no conclusive trend can be observed from the data set. Only small details are observed such as the asymmetric positions yielding lower drag near 0° and the symmetric position seeming to yield reduced drag near 15°. It can also be said that the symmetric position drag results seem more sensitive to changing yaw angles.

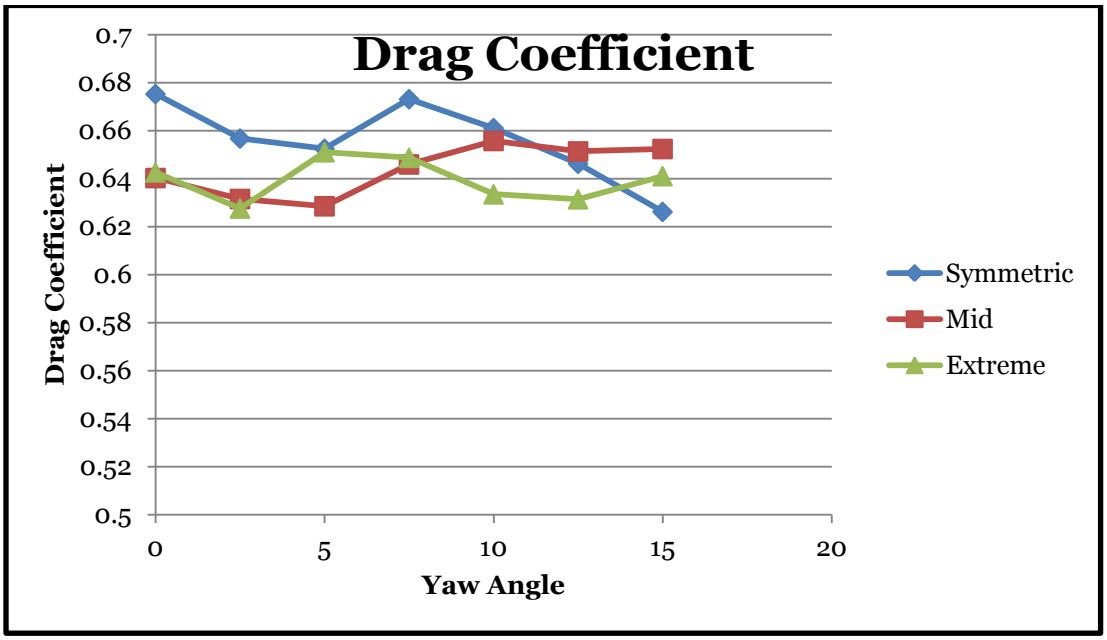

Figure 37 – Drag Coefficient Comparison

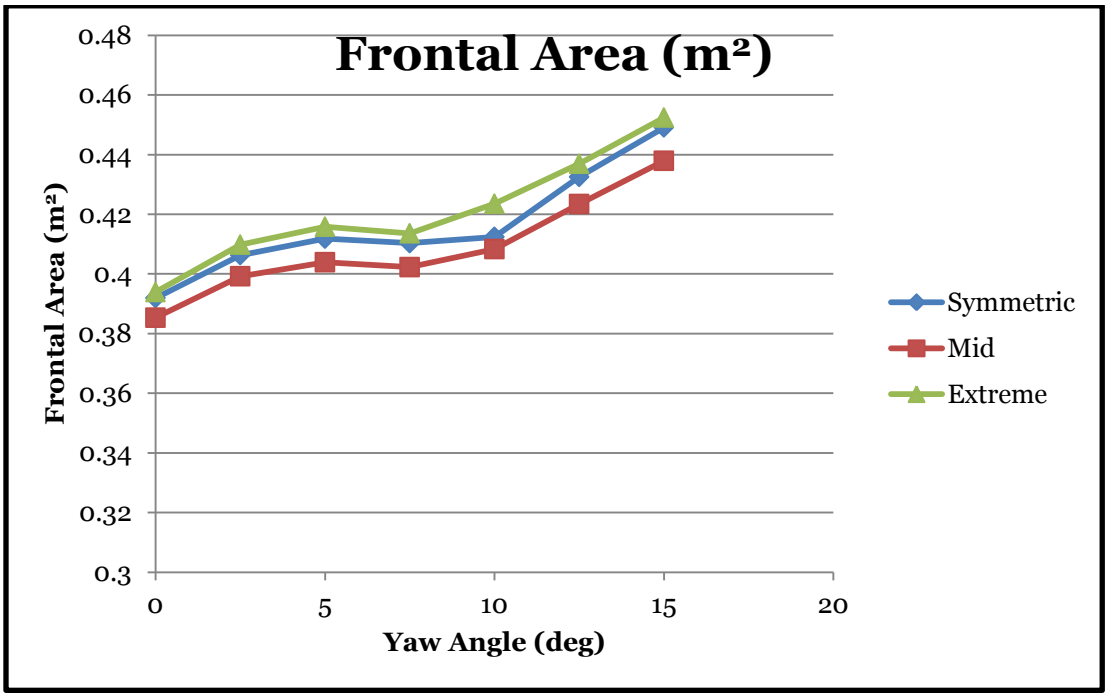

Figure 38 – Frontal Area Comparison

Since drag coefficient relies on a reference (frontal) area to be determined, it is helpful to also see a comparison of such values for each of the configurations (Figure 38). This figure shows the frontal area increasing as the yaw angle is increased. Although there is a slight deviation between 5° and 10°, the expected trend is observed.

Table 5 – Drag Coefficient Comparison

Drag Coefficient		Angle						
		0°	2.5°	5°	7.5°	10°	12.5°	15°
Position	Symmetric	0.6752	0.6567	0.6524	0.6731	0.6610	0.6462	0.6262
	Mid	0.6403	0.6315	0.6285	0.6459	0.6557	0.6513	0.6524
	Extreme	0.6426	0.6276	0.6510	0.6487	0.6335	0.6314	0.64111

Table 6 – Frontal Area Comparison

Frontal Area (m^2)		Yaw Angle						
		0°	2.5°	5°	7.5°	10°	12.5°	15°
Position	Symmetric	0.3919	0.4063	0.4118	0.4103	0.4124	0.4325	0.4491
	Mid	0.3853	0.3992	0.4039	0.4022	0.4083	0.4234	0.4379
	Extreme	0.3939	0.4098	0.4158	0.4136	0.4235	0.4369	0.4524

Seen in Table 5 is the data set represented in Figure 37. The raw numbers also do not reveal an obvious trend as they appear almost randomly distributed around the mean. However, the drag results from this study do more closely agree with general drag coefficient values seen in several outside sources. Table 6 shows the data set represented in Figure 38. Here, the trend seen is as expected – as the rider-bicycle system is rotated, the area exposed to the fluid direction grows. Additional plots, including velocity and surface pressure for each simulation and drag coefficient convergence for each simulation can be seen in Appendix A and Appendix B, respectively.

4 CONCLUSIONS

A large-scale, virtual aerodynamic testing instrument was developed and applied to a specific problem in this project. Below is the summary of my contributions and project findings:

1. Investigated and developed 3-D scanning methods to digitize a live system where no parametric geometry files are available.
    1.1. Two separate rider-bicycle systems were successfully scanned with a 3-D laser scanner.
    1.2. Using Geomagic software, separate 3-D images were aligned and merged to created complete, closed, and smooth models.
2. Developed CFD analysis methods optimized for aerodynamic analysis of large systems, mimicking a full-scale wind tunnel test.

2.1. Rider-bicycle models were imported into a CFD software package, and simulations at different yaw angles were conducted.

2.2. Simple shape CFD validation was run to help verify simulation setup.

2.3. Mesh sensitivity analysis was conducted to gauge the sensitivity of the solution on mesh size.

3. The developed methodology was applied to study the effect of different riding positions on drag force acting on a time-trial bicycle rider when a wind yaw angle is present.

3.1. Plausible conclusions were drawn from initial study results supporting the theory of optimized rider position for significant wind yaw angles.

3.2. A second study showed better correlation in drag coefficient to experimental values obtained from outside sources but yielded less conclusive results to support drag reduction theory.

3.3. Directions for future work were discussed including the use of structured light scanning and a robust turntable for improved scanning quality and efficiency.

4. Feasibility of the virtual wind tunnel instrument for use on large systems was supported and future recommendations were made.

4.1. Use of structured light may be more useful in the case of large systems where focal range is important.

4.2. Investigation of other 3-D scan alignment and merging software may allow more accurate model creation.

4.3. Computing resources was a limiting factor and acquisition of additional computing power would allow for further mesh sensitivity analysis and more robust CFD simulations.

Valuable information was collected throughout this project on the key subjects of 3-D scanning and CFD analysis and progress was made regarding the use of these design tools in conjunction. It is easily concluded that this approach can be much more economical than strict wind tunnel experiments as one 3-D scanner and one desktop computer were used for all work. With advancements in computing technologies continuing at such a high pace today, this price gap between virtual testing and real wind tunnel testing will only grow. A possible compromise for companies who still wish to validate CFD analysis through wind tunnel experiments would be the use of small-scale models in wind tunnel experiments. This, however, uncovers additional considerations which cannot be ignored, such as conserving important scale-dependent, dimensionless parameters which characterize the flow. In order to accurately apply small-scale findings to a full-scale design, one must adjust variables, such as fluid density and velocity, to compensate for the smaller scale within which the experiment is being conducted. Compensations of this kind may require a variable density wind tunnel, which may not be a feasible option for many companies (Contini, Cesari, Donateo, & Robins, 2009). With the addition of possible errors associated in

scaled testing and the resources needed for full-scale testing, large system CFD will continue to be a valuable and necessary design tool.

Comparing results from the pilot study to those in the second, revised study, it becomes unclear whether the theory could provide a significant reduction in drag for bicycle racing. The theory was not disproved, but in order to conclude that the theory yields significant results, additional effort and resources will be required. It was desired to use the revised study to collect data which could confirm the pilot study results; however, this conclusion cannot be drawn from the current data set at this time. Many variables were changed between the first and second studies, including the rider, the bicycle, the use of a time-trial helmet, and some updates to the CFD model. An area with perhaps the most variability is how a rider adjusts his/her posture based on the position of the handlebars. The proposed theory could greatly benefit from additional research into this area as well as an ergonomic evaluation of the suggested riding positions. A drastically asymmetric riding position could result in instability and increased fatigue for the rider. This would, of course, detract from the advantages in drag reduction. It is believed that this theory still holds valuable contributions toward bicycle racing and that additional work will confirm the theory. When wins and losses come down to seconds, or fractions of seconds, at the highest level of bicycle racing, any reduction in drag could prove significant.

Recommendations for future work can also be made in both the areas of 3-D scanning and CFD modeling of large systems. If the subsequent use of a 3-D

scanned model is to be CFD analysis, much consideration must be placed on obtaining a high quality surface representation. Devices that may produce significant noise and surface inaccuracies will cause problems during CFD simulations. Additionally, the focal range of the scanner must also be considered to allow for each image to capture a large portion of the object or system. This would greatly ease the process of assembling and merging images as well as reducing the error occurring from this process. Seams and holes between overlapping images were areas that required a great amount of post-processing work. It is recommended that structured light scanning be investigated for this purpose. It was also found that the incorporation of the final 3-D model into a CFD program was very simple and as easy as importing any general CAD (Computer-Aided Design) model. With a more efficient scanning process, many different models could be simulated without requiring significant time investment. Additional refinements could be investigated within the CFD analysis step of the study. There are numerous parameters used for adjusting physics and mesh conditions which could provide a more stable solution. With additional computer resources available, extremely refined meshes could be investigated to better understand the mechanics of the study. Both areas, 3-D scanning and CFD analysis, were studied and refined throughout this project. Clear contributions were made to each technology and recommendations for future work have been laid out. With these lessons as resources, continued research into large system

CFD analysis may be conducted to advance the aerodynamic efficiency of systems in several industries.

BIBLIOGRAPHY

Bartosiewicz, Y., Aidoun, Z., Canada, N. R., Box, P. O., Lionel-boulet, B., Jx, V. Q., Desevaux, P., et al. (2003). CFD-Experiments Integration in the Evaluation of Six Turbulence Models for Supersonic Ejectors Modeling. *Integrating CFD and Experiments* (Vol. 1). Glascow.

Boehnen, C., & Flynn, P. (2005). Accuracy of 3D Scanning Technologies in a Face Scanning Scenario. *Fifth International Conference on 3-D Digital Imaging and Modeling (3DIM'05)*, 310–317. doi:10.1109/3DIM.2005.13

Cengel, Y. A., & Cimbala, J. M. (2010). *Fluid Mechanics: Fundamentals and Applications* (2nd ed.). McGraw-Hill.

Chen, C. J., & Jaw, S.-Y. (1998). *Fundamentals of Turbulence Modeling*. Taylor & Francis.

Contini, D., Cesari, D., Donateo, A., & Robins, A. G. (2009). Effects of Reynolds Number on Stack Plume Trajectories Simulated with Small Scale Models in a Wind Tunnel. *Journal of Wind Engineering and Industrial Aerodynamics*, 97(9-10), 468–474. doi:10.1016/j.jweia.2009.07.007

Cote, M. (2008). *Aerodynamics of Time Trial versus Road Configurations (Transition vs . Tarmac SL2)* (pp. 1–11).

DAVID 3D Solutions. (2012). David-LaserScanner. Retrieved from http://www.david-laserscanner.com/

Debraux, P., Grappe, F., Manolova, A. V., & Bertucci, W. (2011). Aerodynamic Drag in Cycling: Methods of Assessment. *Sports Biomechanics*, 10(3), 197–218. doi:10.1080/14763141.2011.592209

Defraeye, T., Blocken, B., Koninckx, E., Hespel, P., & Carmeliet, J. (2010a). Aerodynamic Study of Different Cyclist Positions: CFD Analysis and Full-Scale Wind-Tunnel Tests. *Journal of biomechanics*, 43(7), 1262–8. doi:10.1016/j.jbiomech.2010.01.025

Defraeye, T., Blocken, B., Koninckx, E., Hespel, P., & Carmeliet, J. (2010b). Computational Fluid Dynamics Analysis of Cyclist Aerodynamics: Performance of Different Turbulence-Modelling and Boundary-Layer Modelling Approaches. *Journal of biomechanics*, 43(12), 2281–7. doi:10.1016/j.jbiomech.2010.04.038

Drag (Physics). (2012).*Wikipedia*. Retrieved from http://en.wikipedia.org/wiki/Drag_(physics)

Gentes, J. J., & Sasaki, S. K. (1990). Aerodynamically Streamlined Bicycle Racing Helmet.

Geomagic. (2010). Geomagic Studio. Retrieved from http://geomagic.com/en/products/studio/overview

Godo, M. N. (2010). An Aerodynamic Study of Bicycle Wheel Performance using CFD. *STAR European Conference*. Intelligent Light.

Gross, A. C., Kyle, C. R., & Malewicki, D. J. (1983). The Aerodynamics of Human-Powered Land Vehicles. *Scientific American*, 249(6), 142–152. doi:10.1038/scientificamerican1283-142

Hanna, K. (2011). *CAE in Sport – Performance Enhancement without Drugs*. Surry, UK.

Harder, P., Cusack, D., Matson, C., & Lavery, M. (2010). *Airfoil Development for the Trek Speed Concept Triathlon Bicycle* (pp. 1–29).

Hucho, W. H. (1998). *Aerodynamics of Road Vehicles: from Fluid Mechanics to Vehicle Engineering* (4th ed.). Society of Automotive Engineers.

IHPVA Official Land Speed Records. (2009). Retrieved from http://www.ihpva.org/hpvarec3.htm#nom12

Knupe, J., & Farmer, D. (2009). *Aerodynamics of High Performance Race Bicycle Wheels* (pp. 1–15).

Kuntz, M., & Ferreira, J. C. (2003). Simulation of Fluid-Structure Interactions in Aeronautical Applications. *3rd FENET Annual Industry Meeting*. ANSYS.

LG. (2012). Aerodynamic Development of a Time-Trial Bicycle Helmet: from CFD to Tour de France. *STAR GLOBAL Conference*. Retrieved from http://www.cd-adapco.com/downloads/sgc2012/

Matsushima, T. (2001). An Automatic Mesh Generator Based CFD System to be Used as a Design Tool. *SAE*, 1(37). Retrieved from http://www.shenmo.sh.cn/industry/CFD Paper-1.pdf

Paquette, S. (1996). 3D Scanning in Apparel Design and Human Engineering. *IEEE Computer Graphics and Applications*, 16(5), 11–15.

Peterbilt Motors Company. (2001). *Truck Aerodynamics and Fuel Efficiency*. Retrieved from http://www.peterbilt.com/eco/pdf/Aero WHITE PAPER-2.pdf

Rutberg, J. (2008, December). Wind Tunnel Vision. *Triathlete*, (December), 145–148.

Shahbazi, K. (2007). Pressure Drag Reduction System with an Internal Duct.

Sidorovich, I. (2012). Cervelo P5. *STAR GLOBAL Conference*. Cervelo. Retrieved from http://www.cd-adapco.com/downloads/sgc2012/

Underwood, L., & Schumacher, J. (2011). Aerodynamic Drag and Biomechanical Power of a Track Cyclist as a Function of Shoulder and Torso Angles. *Sports Engineering*, 14(2-4), 147–154. Retrieved from http://www.springerlink.com/index/u21740503r296448.pdf

Wilcox, D. (1994). *Turbulence Modeling for CFD*. DCW Industries, Inc.

Zaïdi, H., Fohanno, S., Taïar, R., & Polidori, G. (2010). Turbulence Model Choice for the Calculation of Drag Forces when Using the CFD Method. *Journal of biomechanics*, 43(3), 405–11. doi:10.1016/j.jbiomech.2009.10.010

APPENDIX A – VELOCITY AND PRESSURE CONTOUR PLOTS FOR EACH SIMULATION

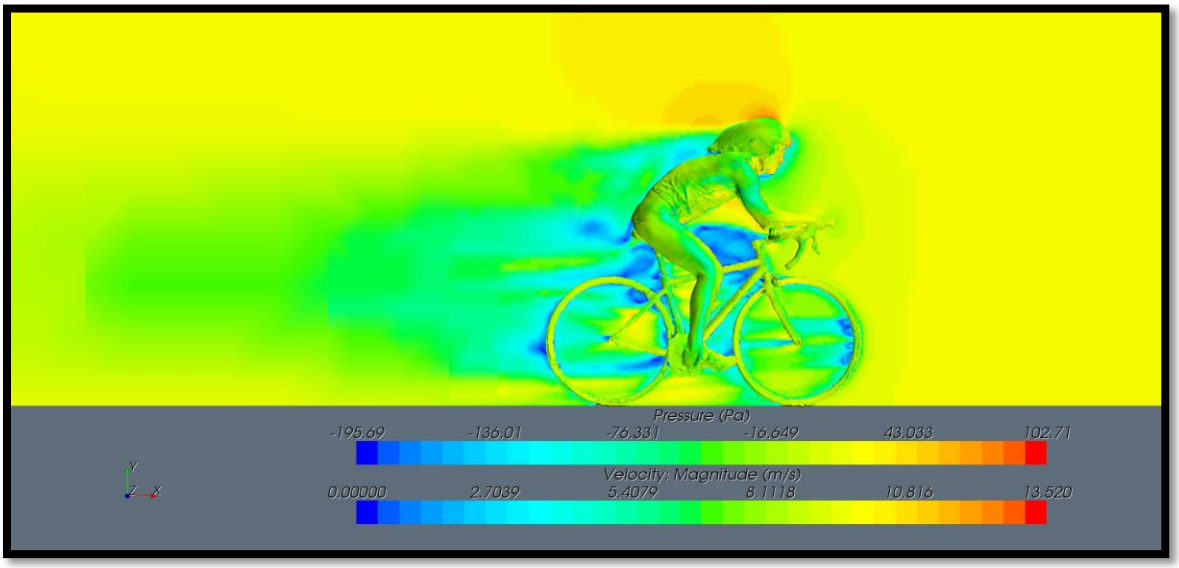

Figure 39 – Velocity and Pressure Plot of Symmetric Position at 0°

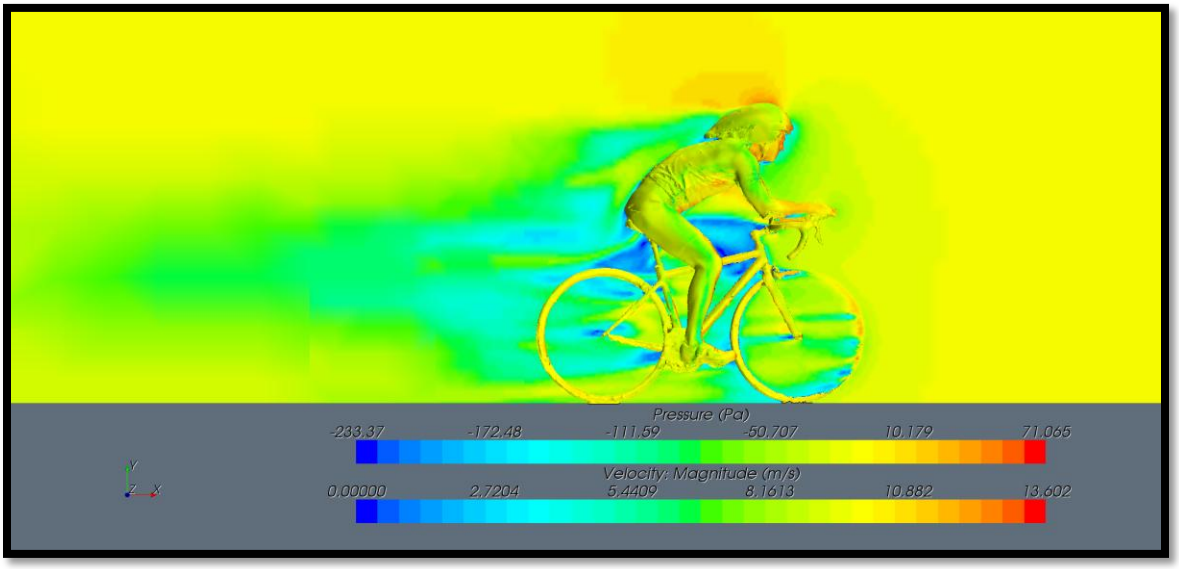

Figure 40 – Velocity and Pressure Plot of Symmetric Position at 2.5°

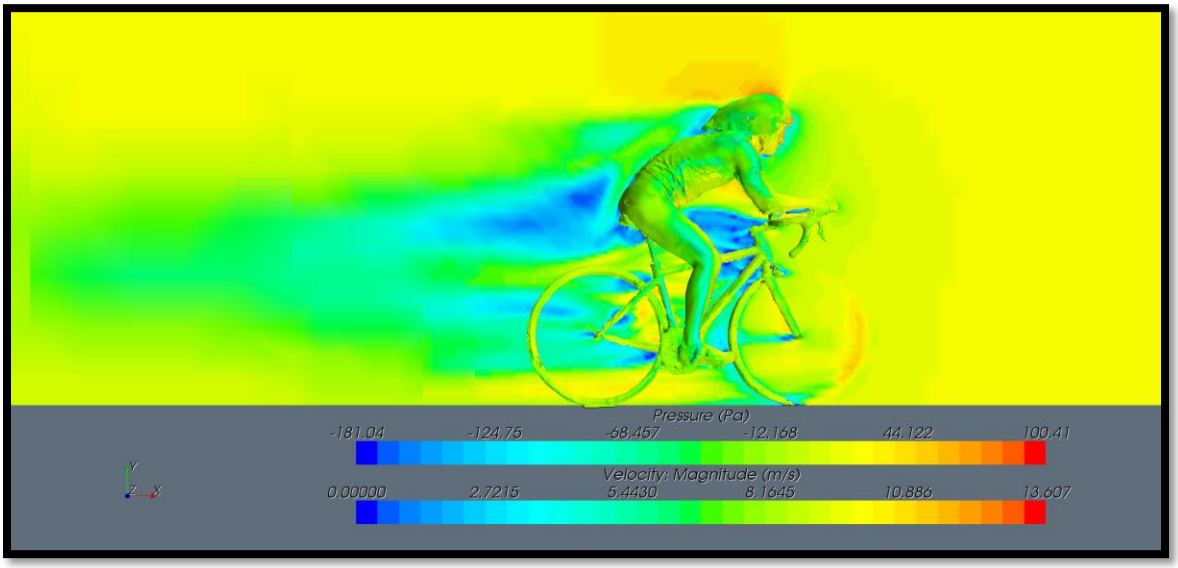

Figure 41 – Velocity and Pressure Plot of Symmetric Position at 5°

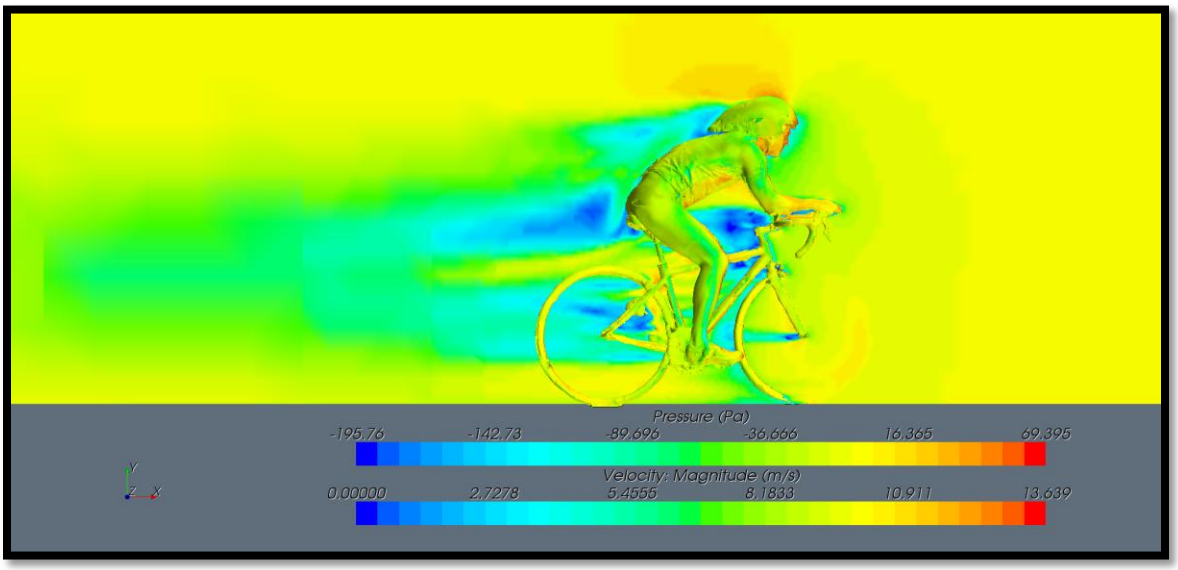

Figure 42 – Velocity and Pressure Plot of Symmetric Position at 7.5°

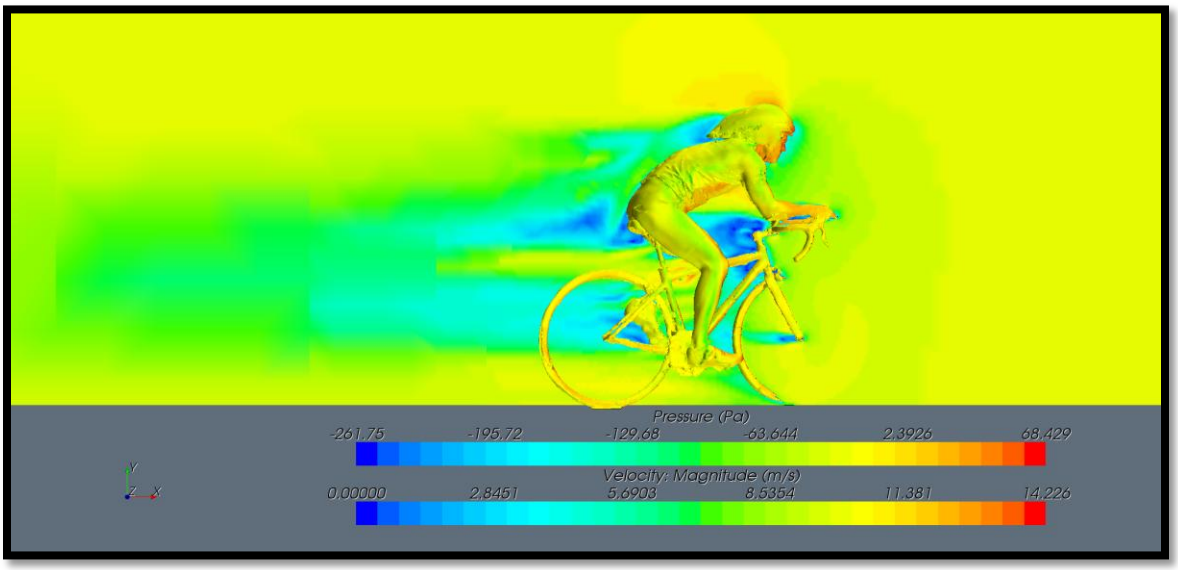

Figure 43 – Velocity and Pressure Plot of Symmetric Position at 10°

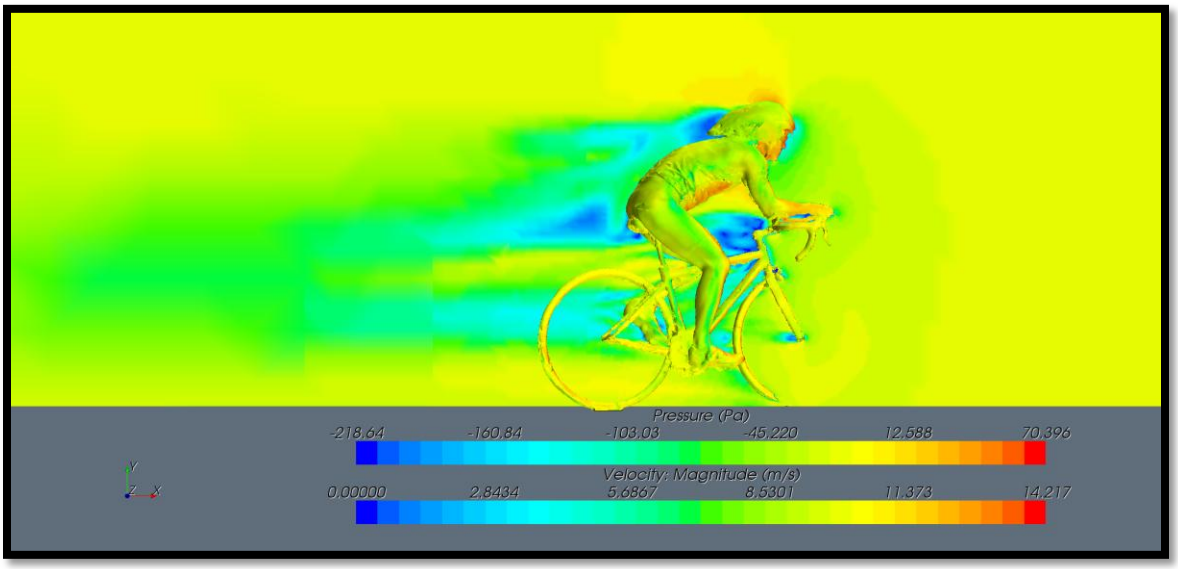

Figure 44 – Velocity and Pressure Plot of Symmetric Position at 12.5°

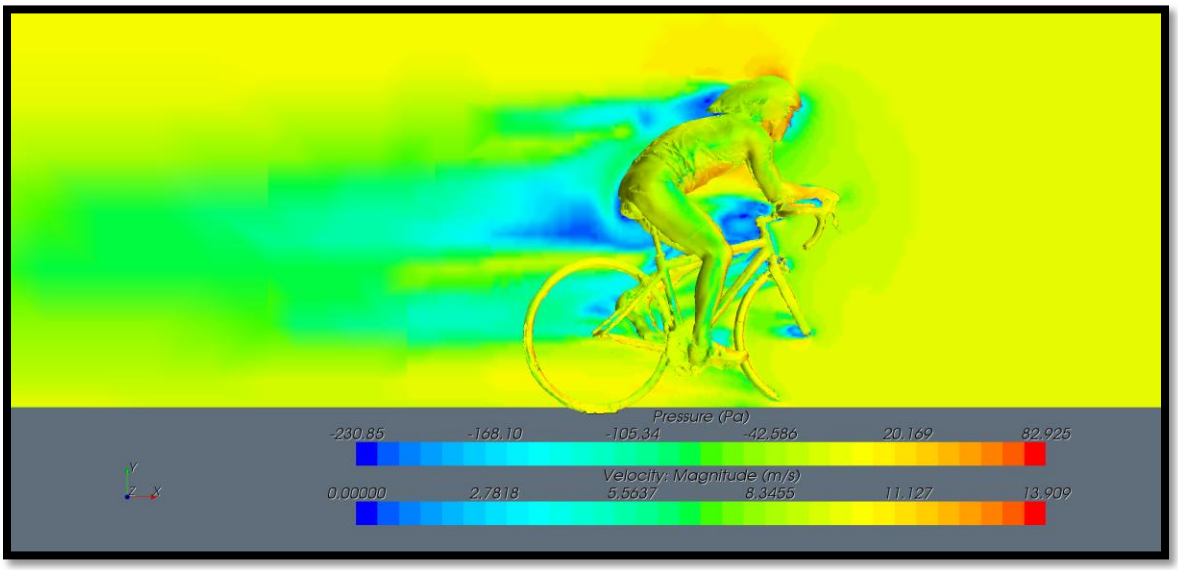

Figure 45 – Velocity and Pressure Plot of Symmetric Position at 15°

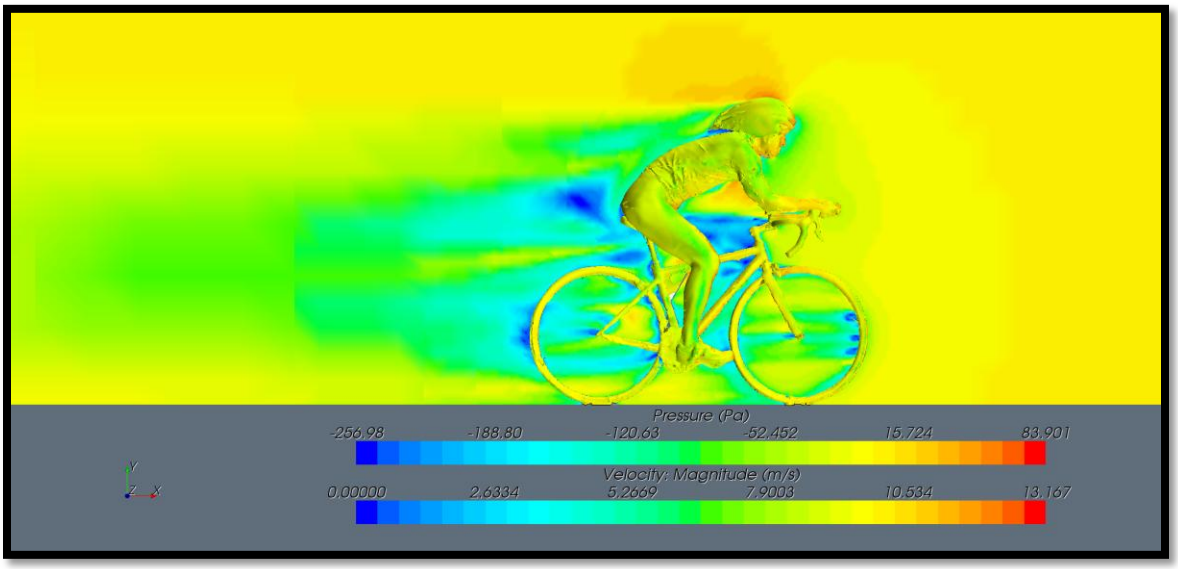

Figure 46 – Velocity and Pressure Plot of Mid Position at 0°

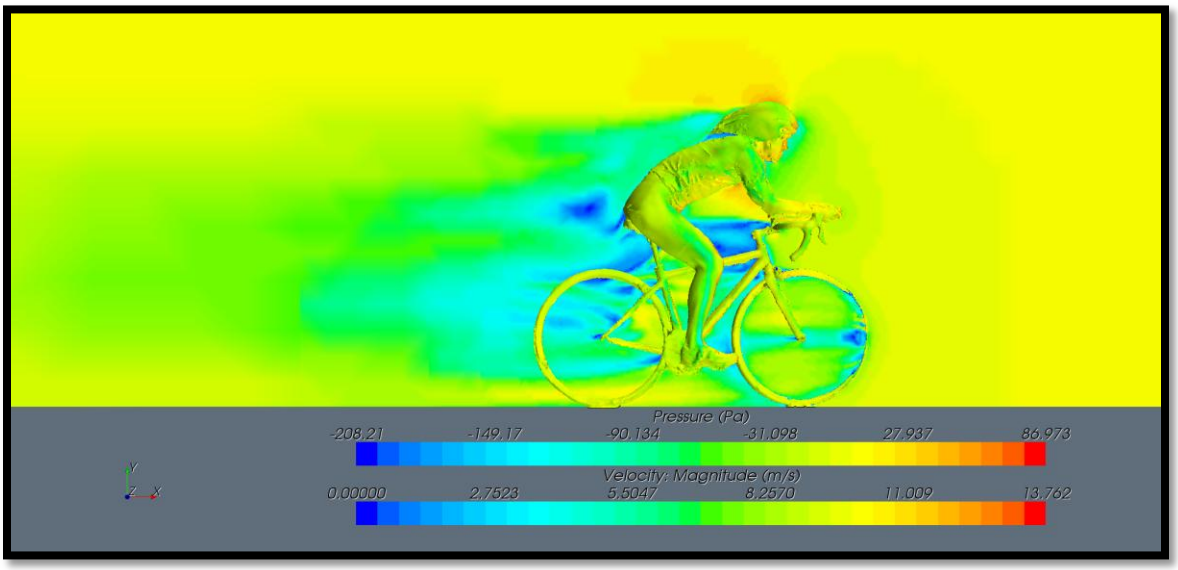

Figure 47 – Velocity and Pressure Plot of Mid Position at 2.5°

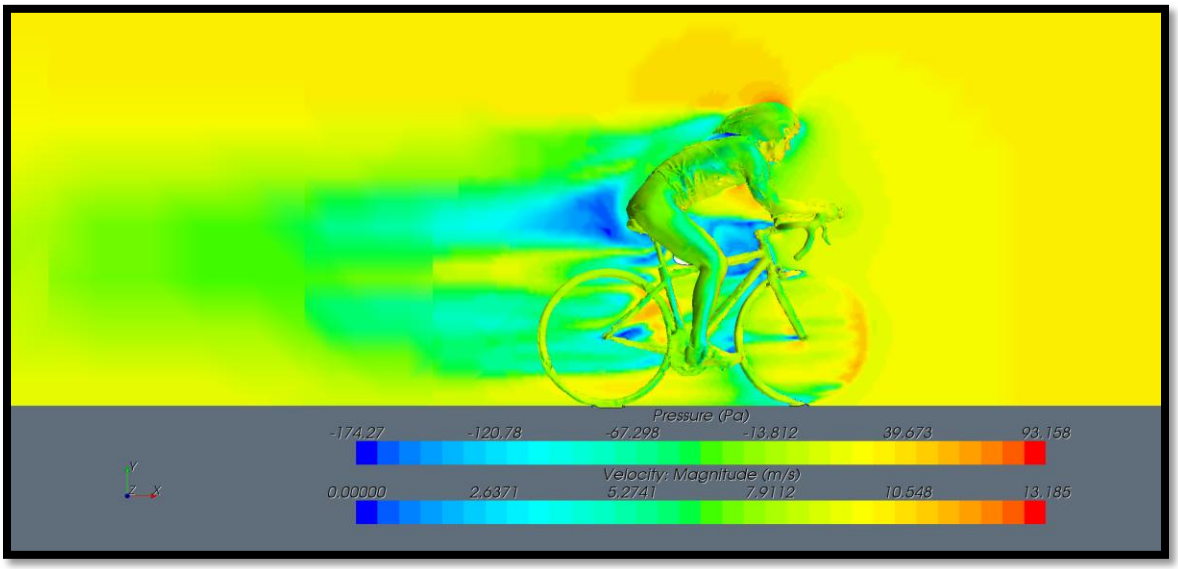

Figure 48 – Velocity and Pressure Plot of Mid Position at 5°

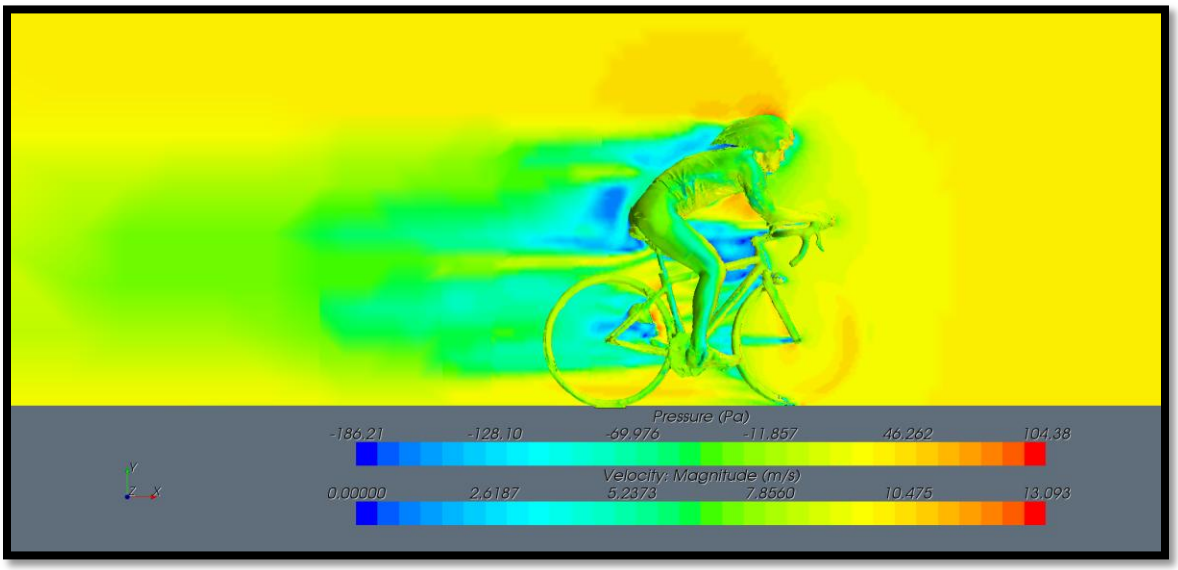

Figure 49 – Velocity and Pressure Plot of Mid Position at 7.5°

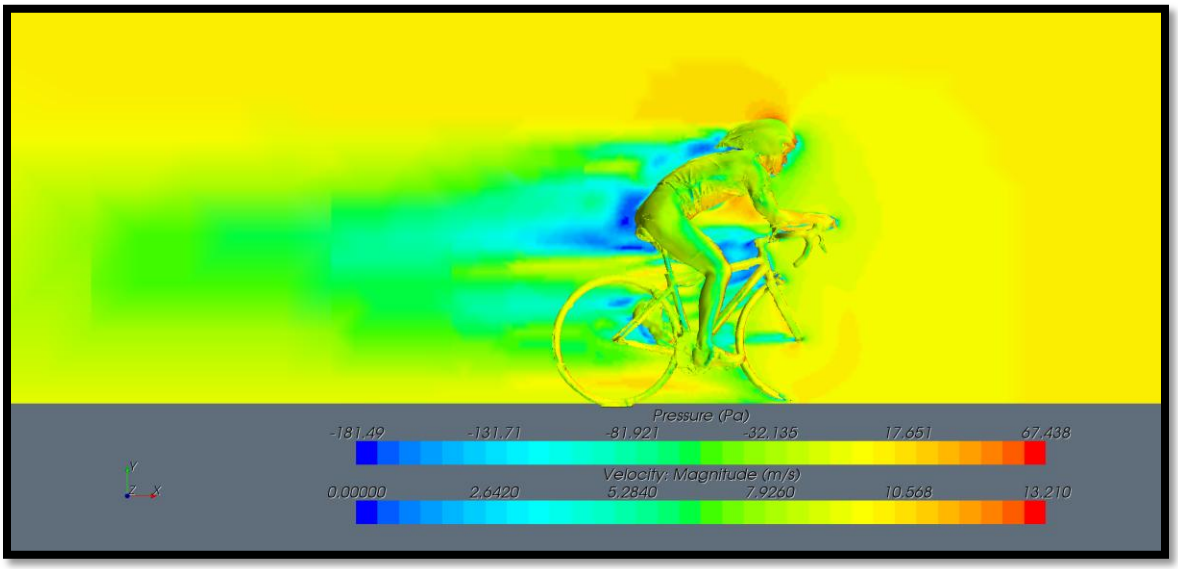

Figure 50 – Velocity and Pressure Plot of Mid Position at 10°

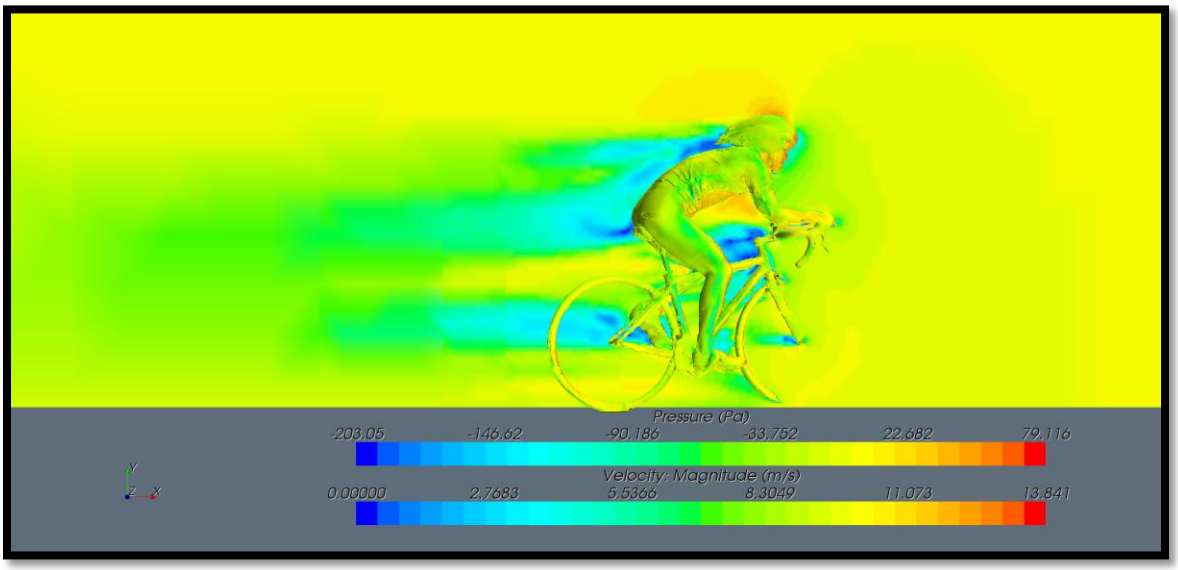

Figure 51 – Velocity and Pressure Plot of Mid Position at 12.5°

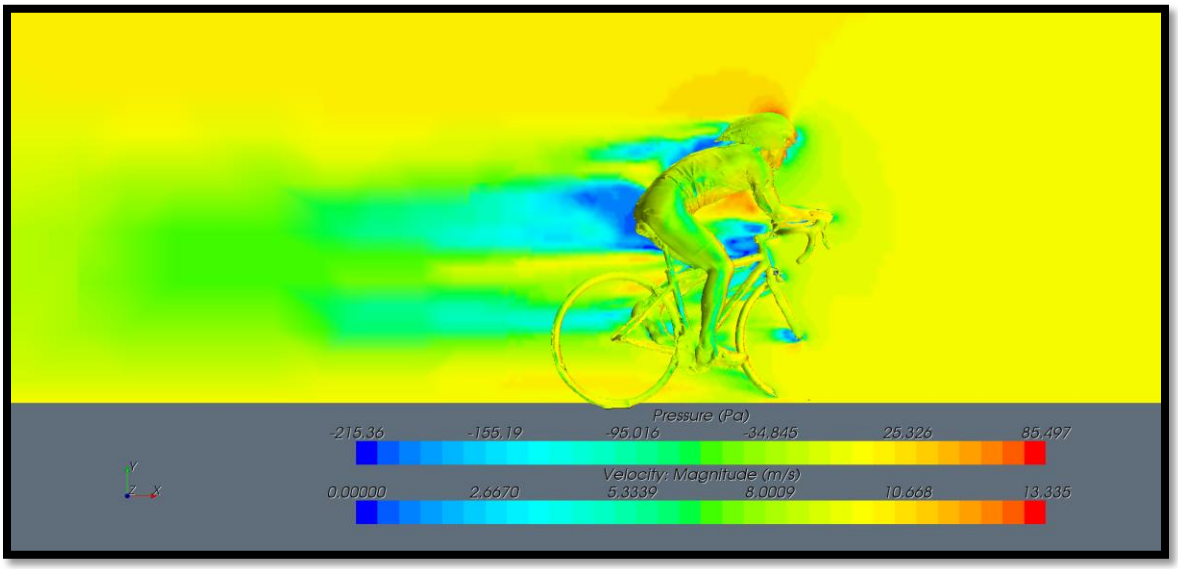

Figure 52 – Velocity and Pressure Plot of Mid Position at 15°

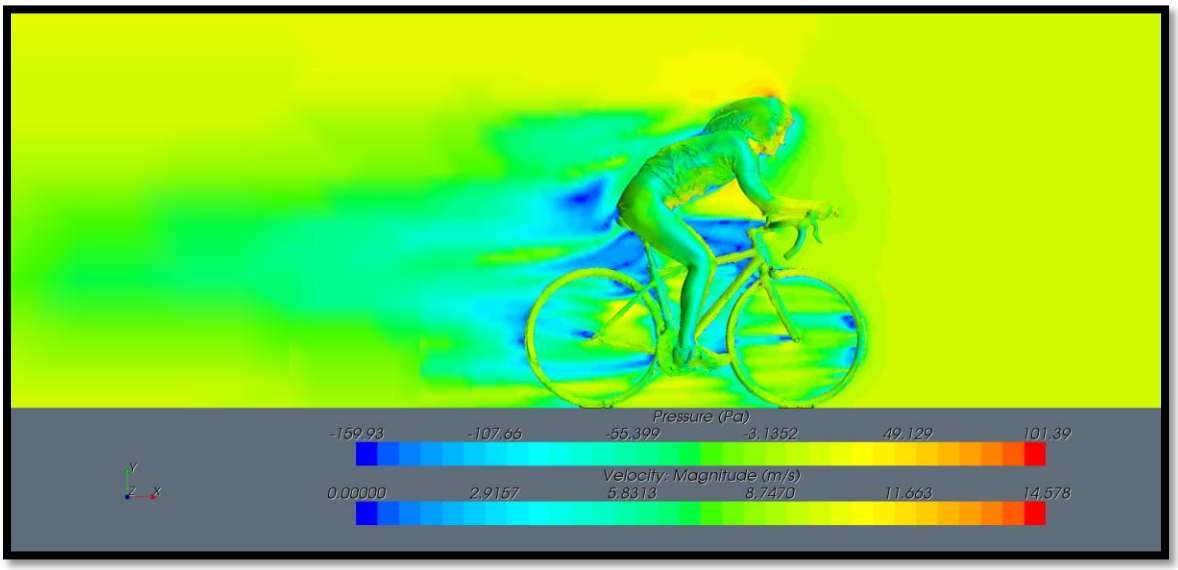

Figure 53 – Velocity and Pressure Plot of Extreme Position at 0°

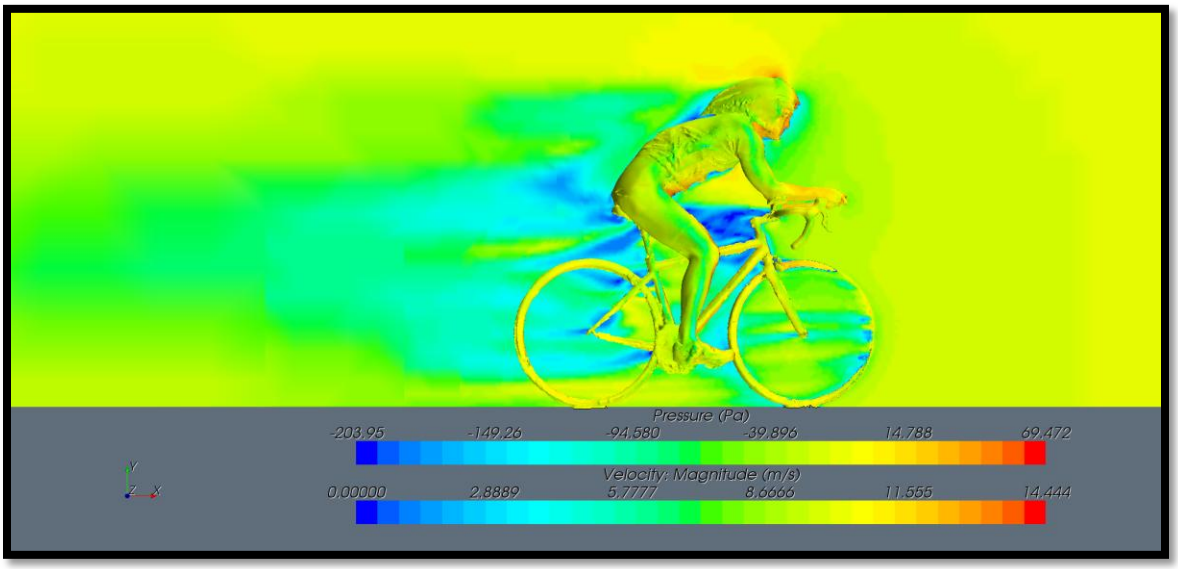

Figure 54 – Velocity and Pressure Plot of Extreme Position at 2.5°

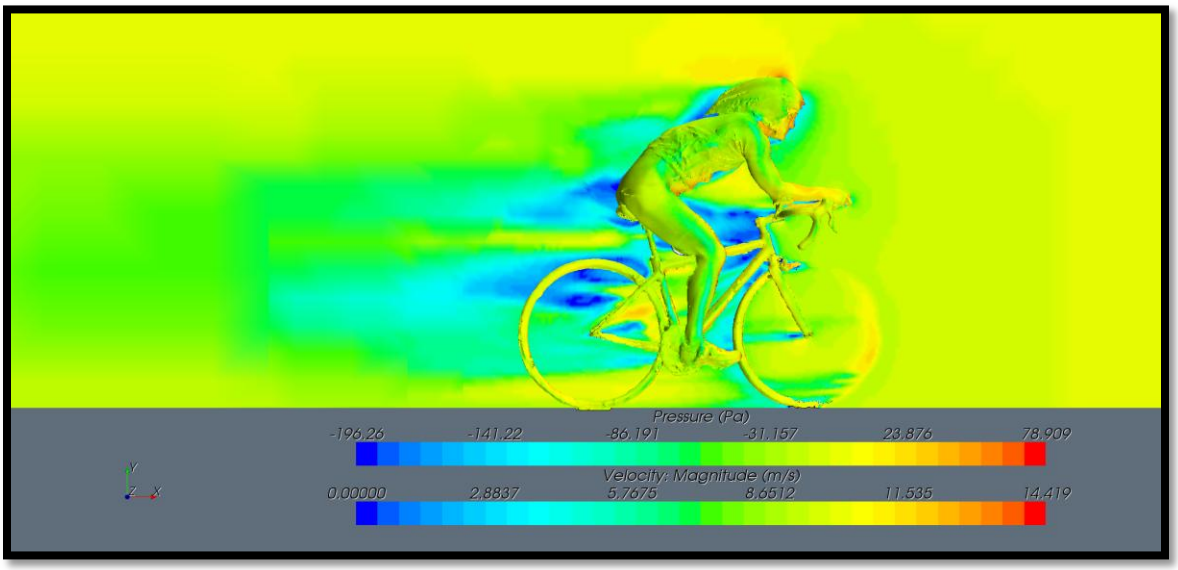

Figure 55 – Velocity and Pressure Plot of Extreme Position at 5°

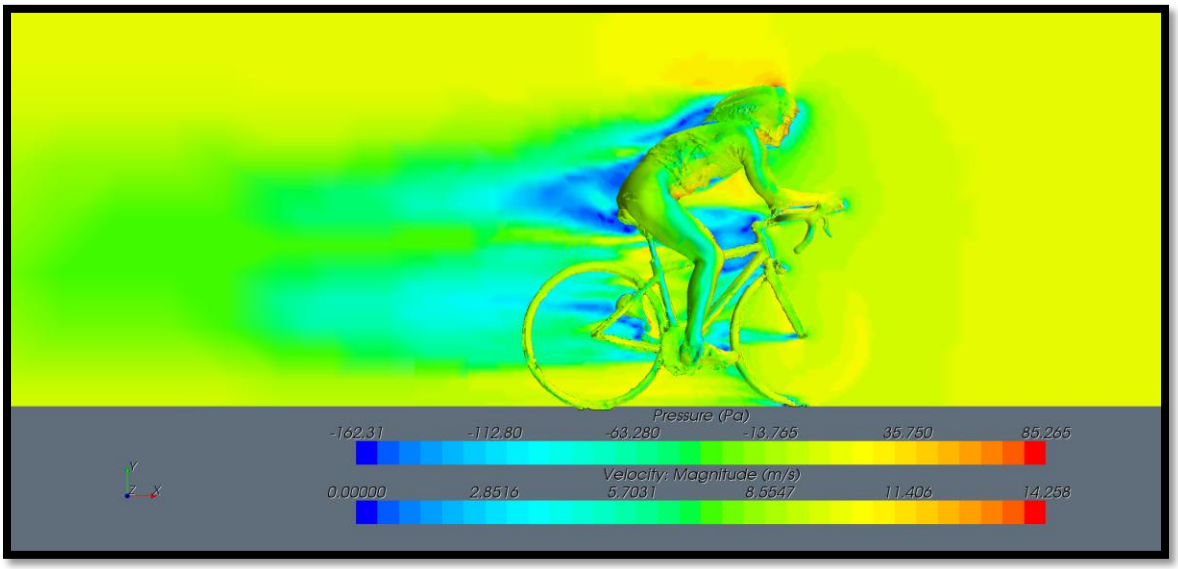

Figure 56 – Velocity and Pressure Plot of Extreme Position at 7.5°

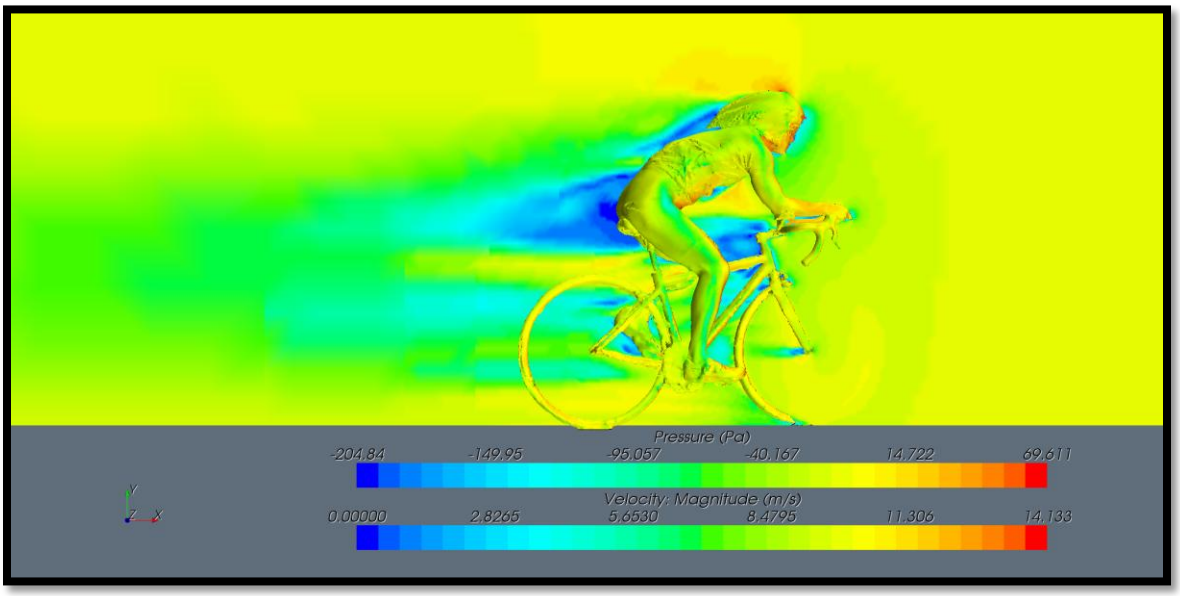

Figure 57 – Velocity and Pressure Plot of Extreme Position at 10°

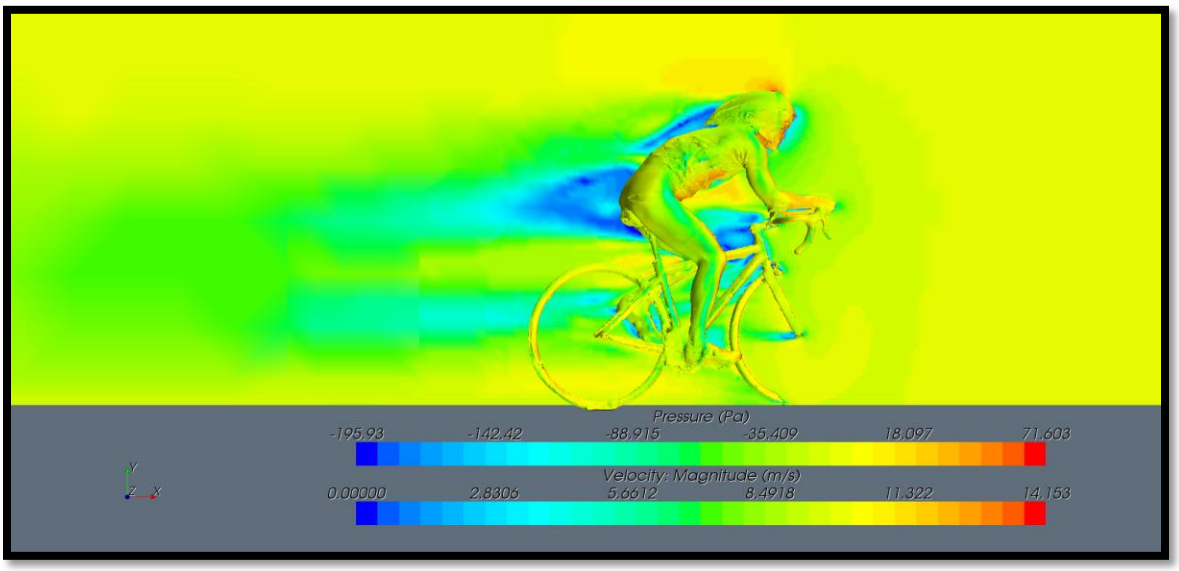

Figure 58 – Velocity and Pressure Plot of Extreme Position at 12.5°

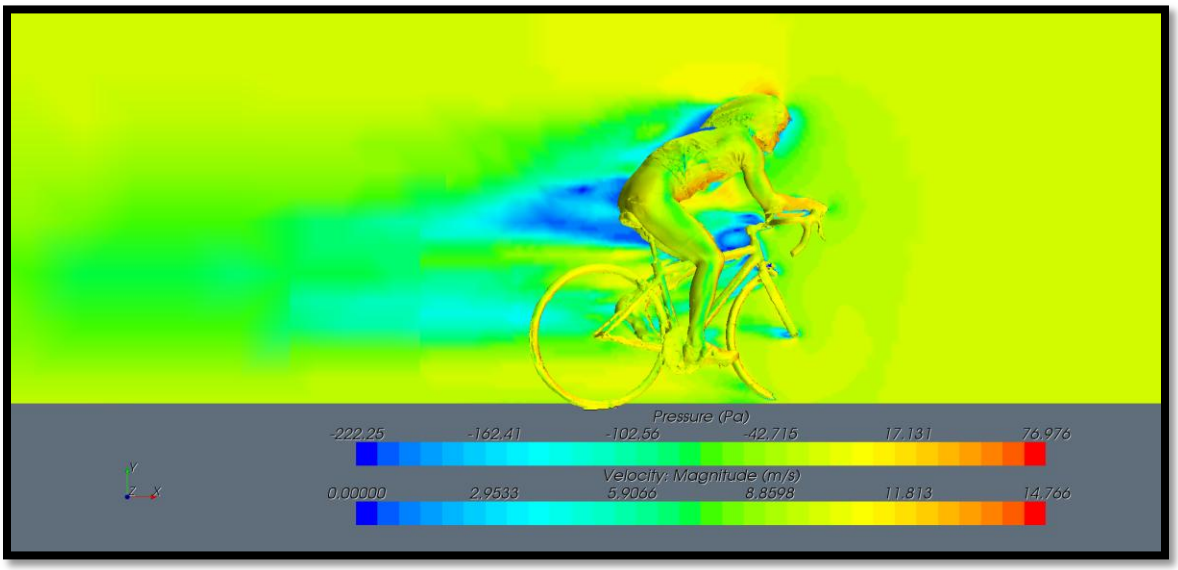

Figure 59 – Velocity and Pressure Plot of Extreme Position at 15°

APPENDIX B – DRAG COEFFICIENT PLOTS FOR EACH SIMULATION

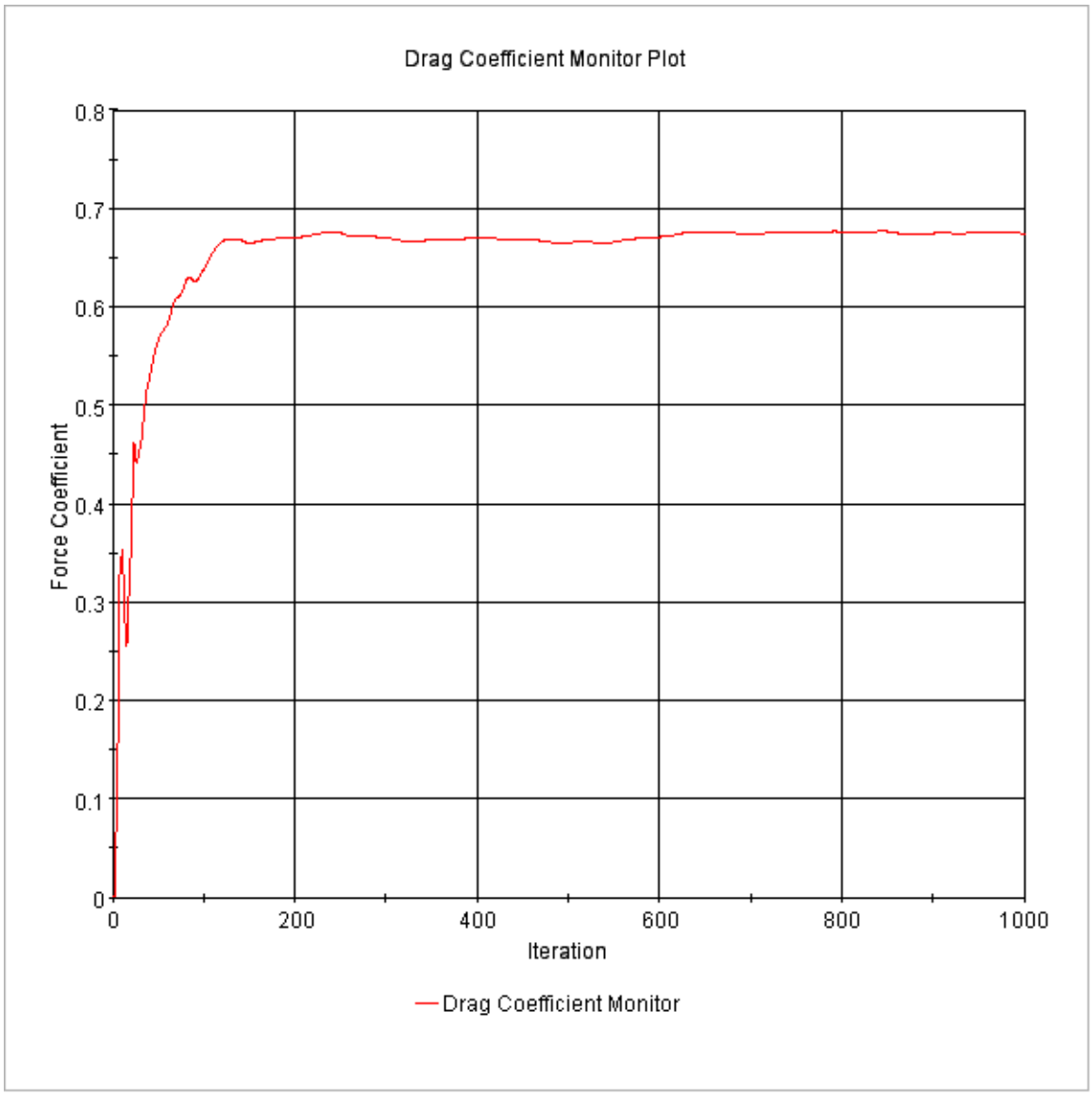

Figure 60 – Drag Coefficient Plot for Symmetric Position at 0° Yaw

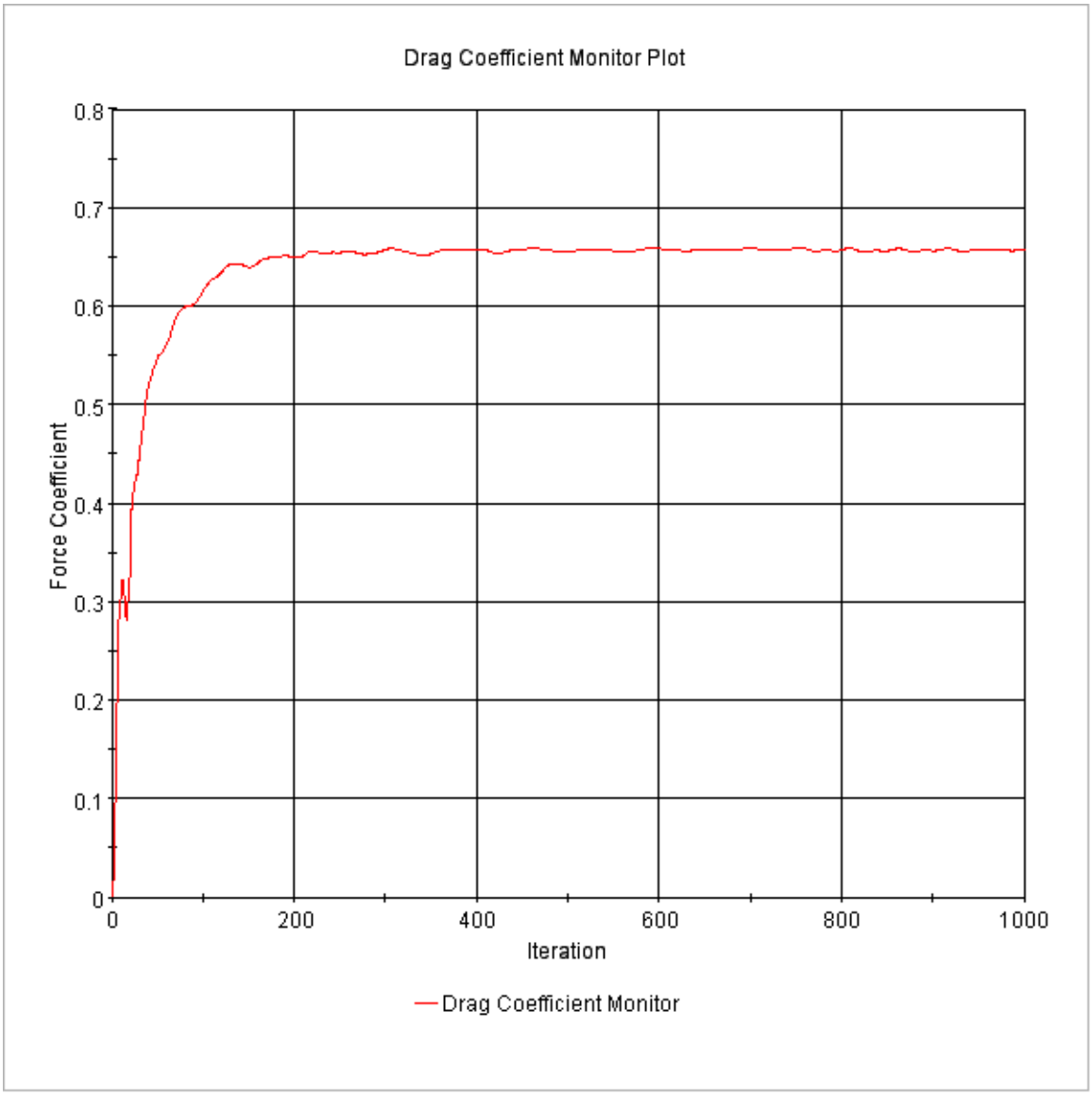

Figure 61 – Drag Coefficient Plot for Symmetric Position at 2.5° Yaw

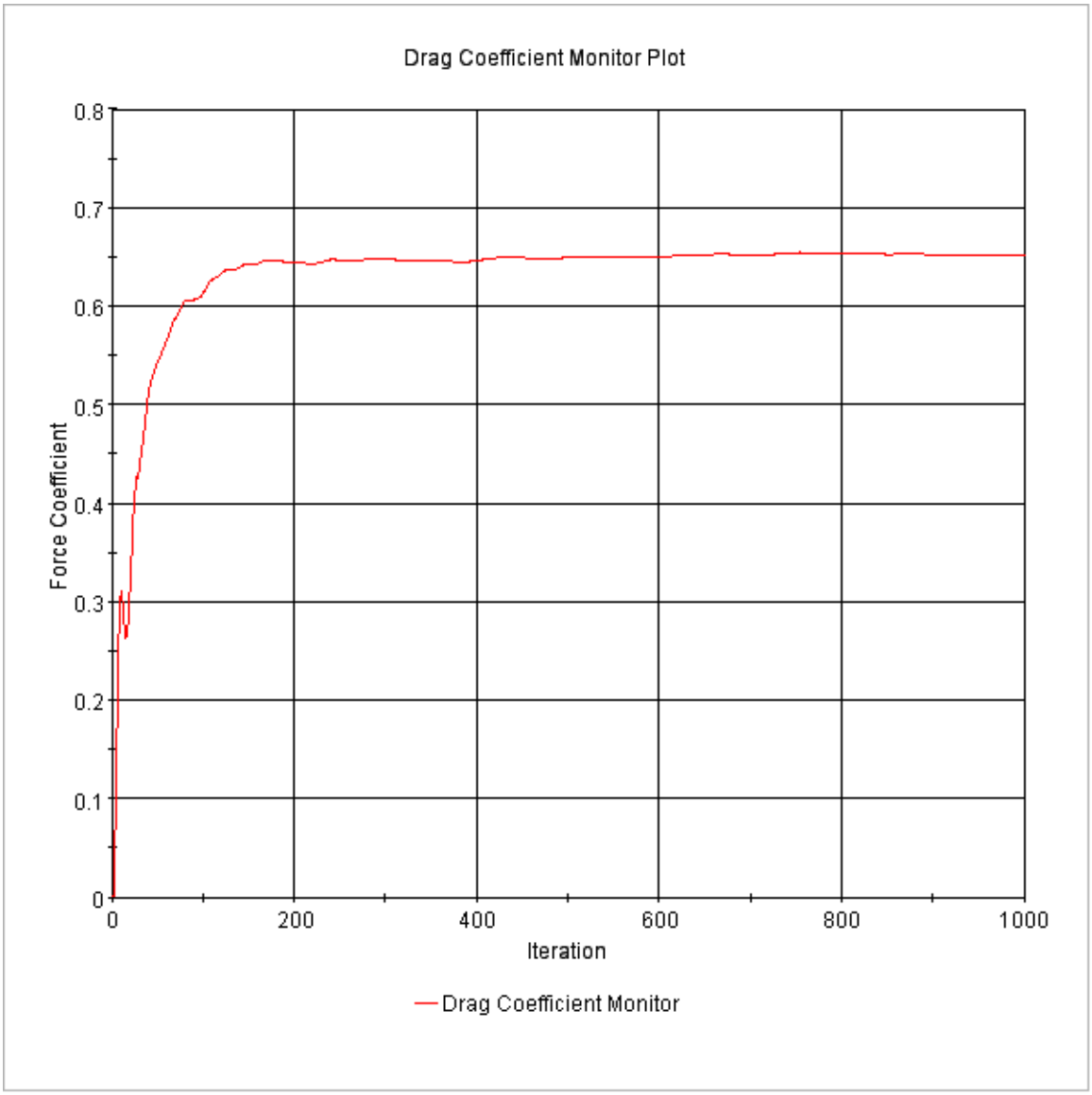

Figure 62 – Drag Coefficient Plot for Symmetric Position at 5° Yaw

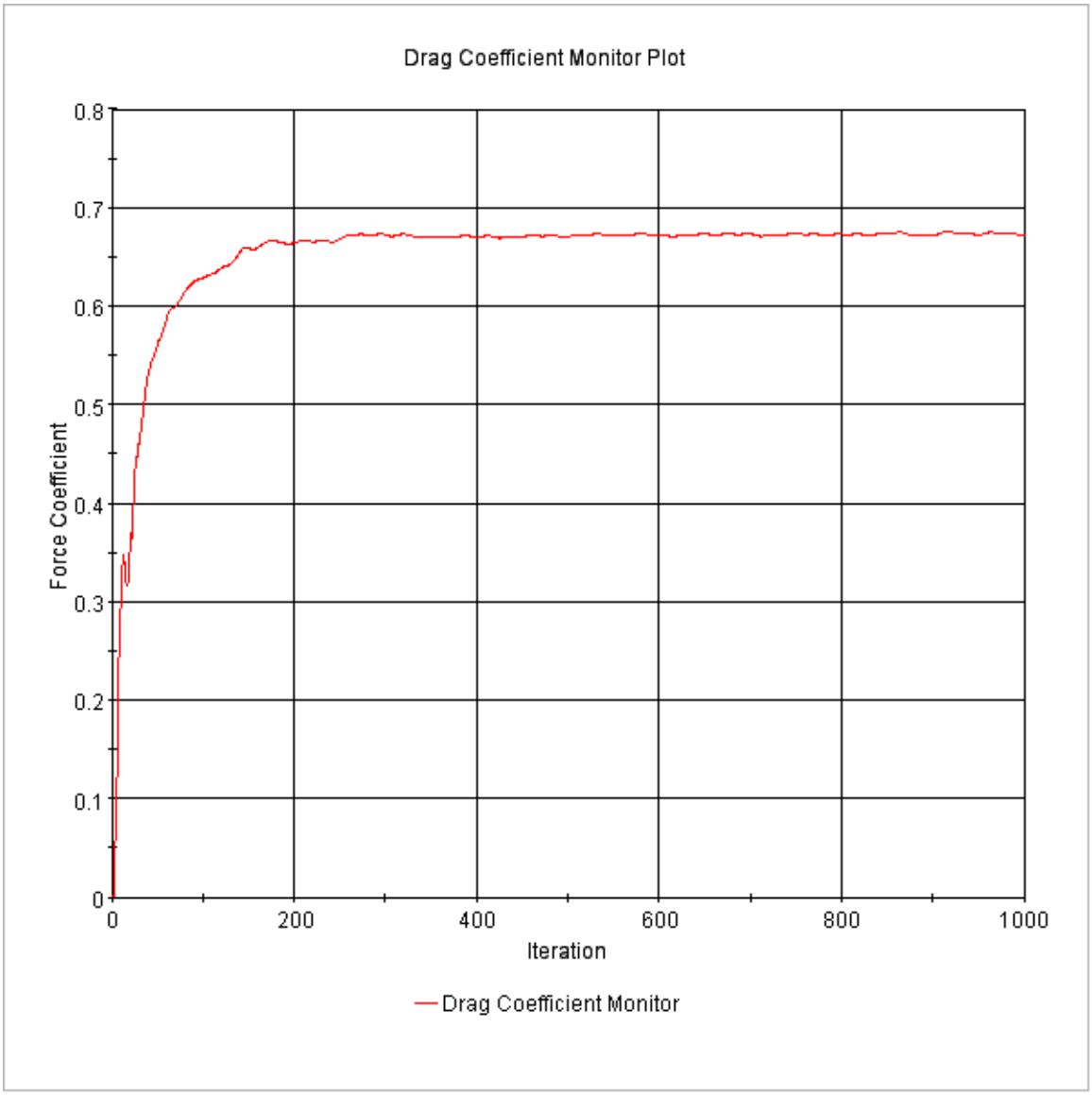

Figure 63 – Drag Coefficient Plot for Symmetric Position at 7.5° Yaw

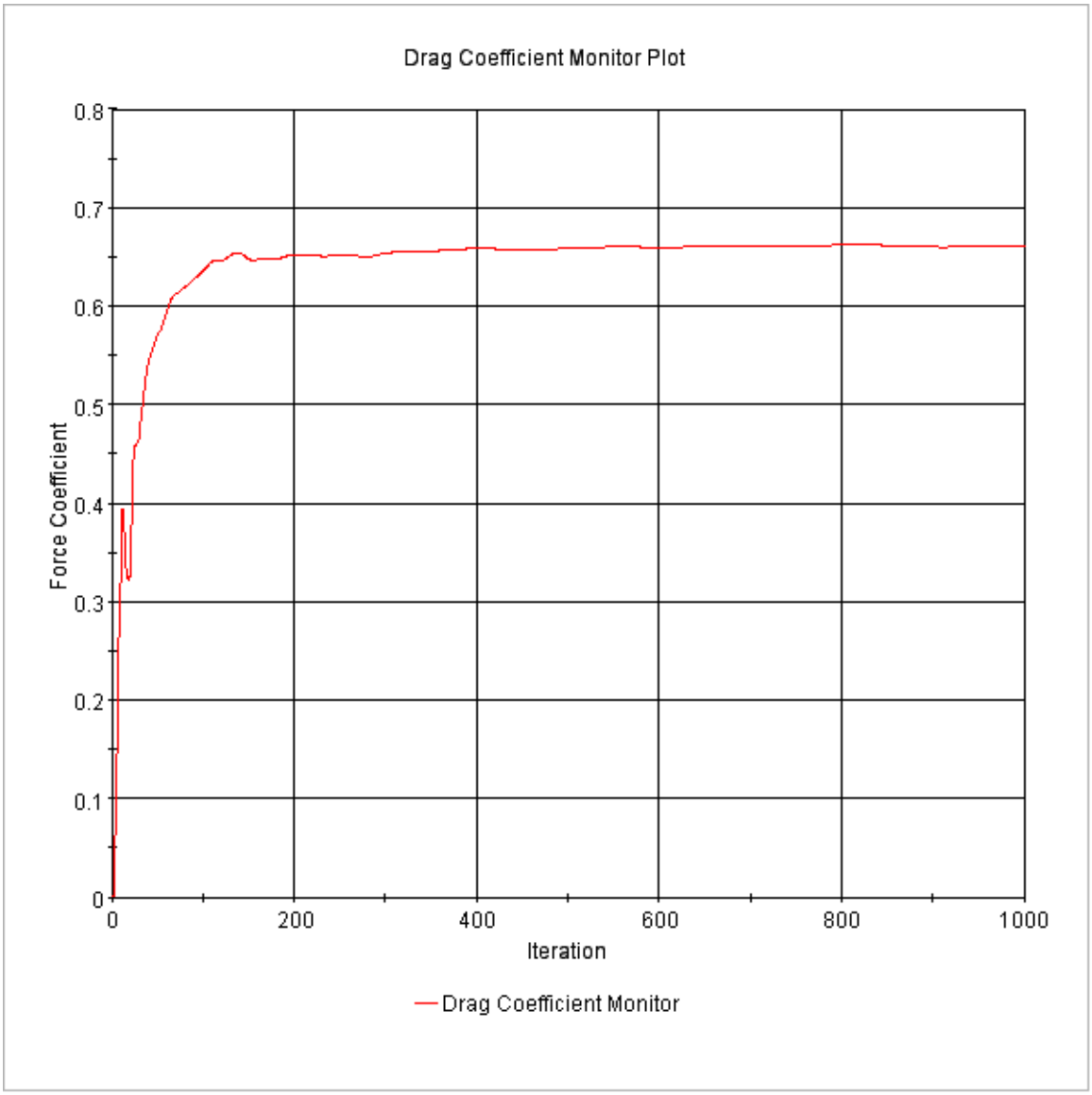

Figure 64 – Drag Coefficient Plot for Symmetric Position at 10° Yaw

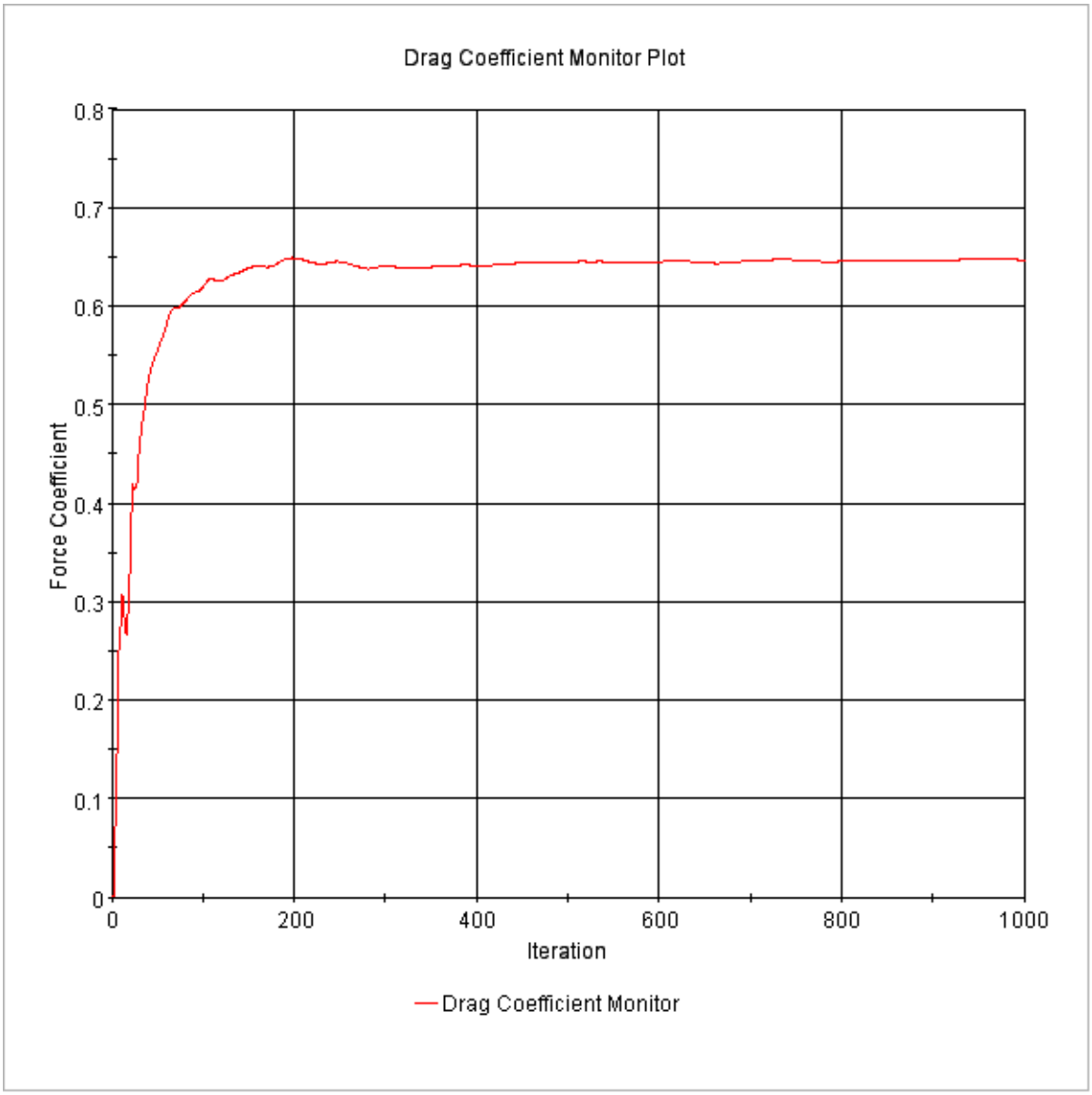

Figure 65 – Drag Coefficient Plot for Symmetric Position at 12.5° Yaw

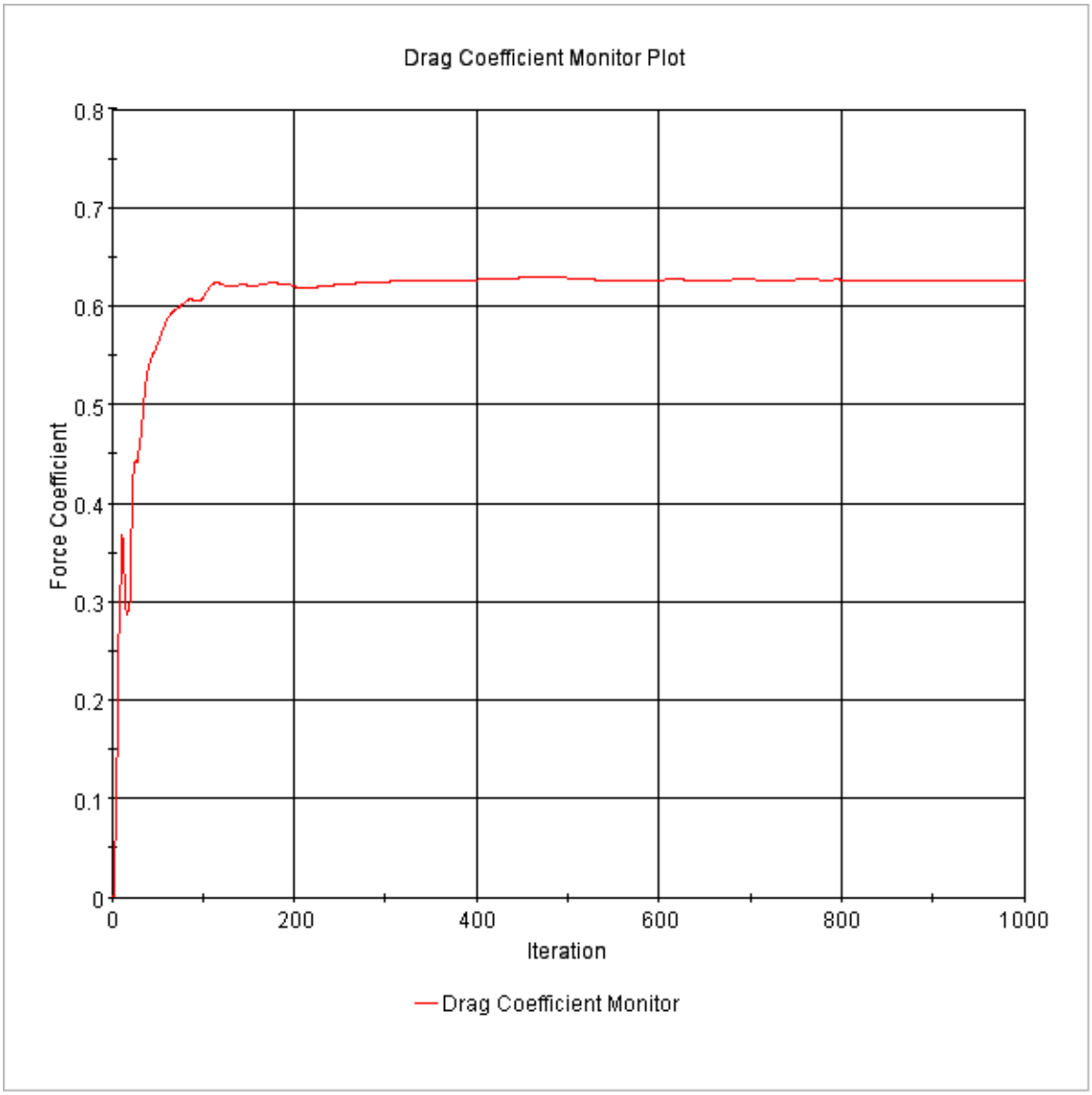

Figure 66 – Drag Coefficient Plot for Symmetric Position at 15° Yaw

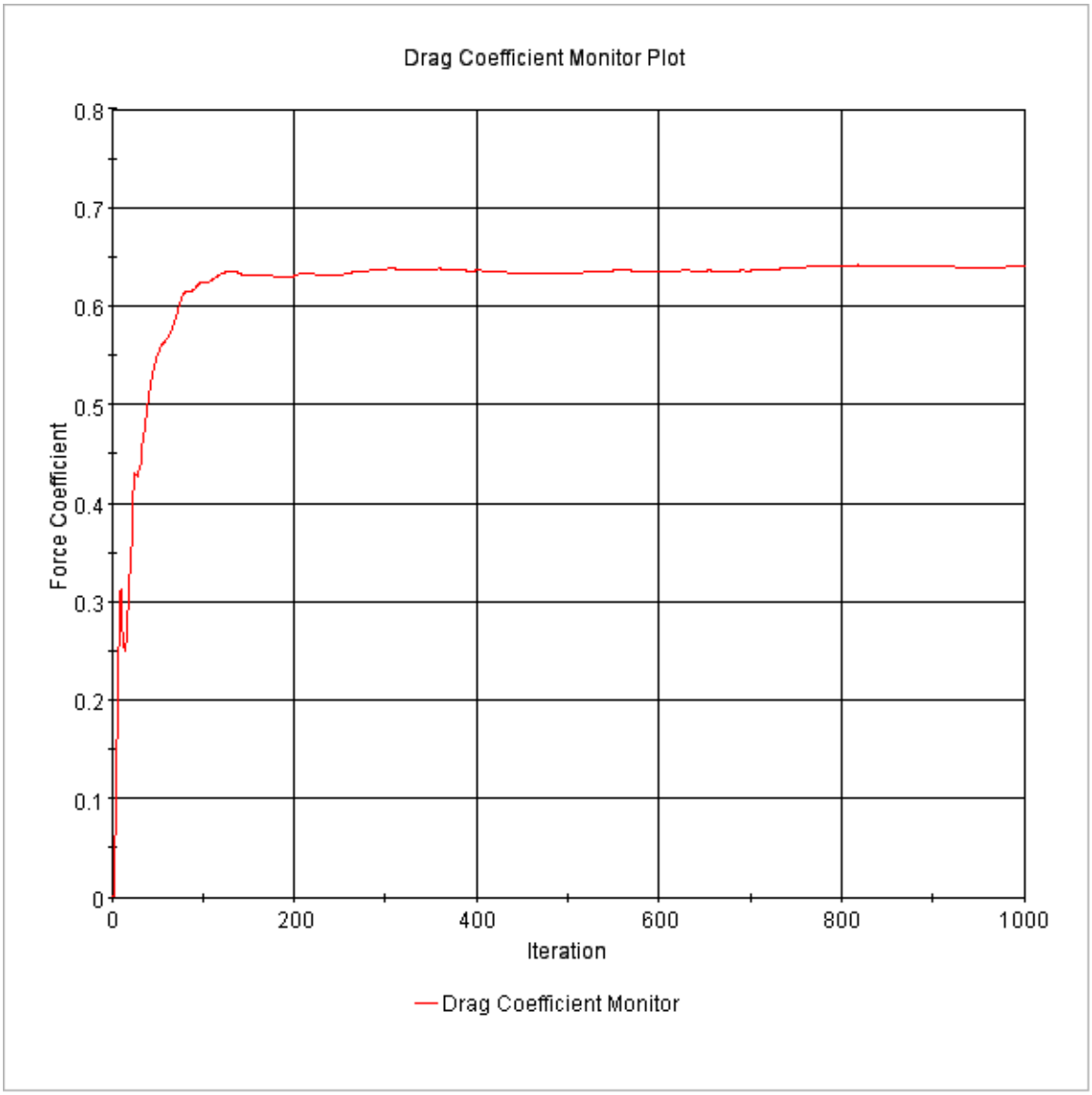

Figure 67 – Drag Coefficient Plot for Mid Position at 0° Yaw

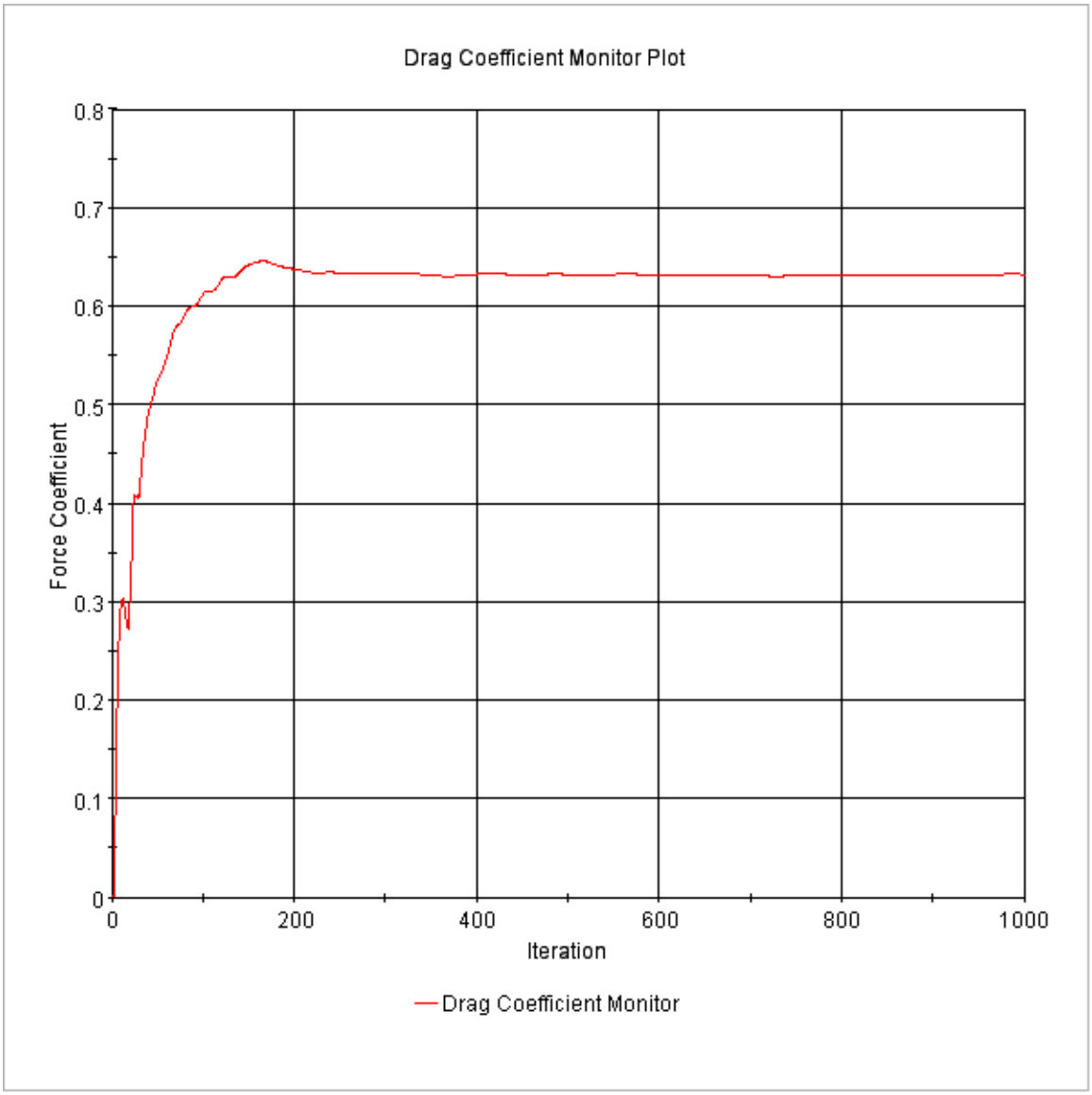

Figure 68 – Drag Coefficient Plot for Mid Position at 2.5° Yaw

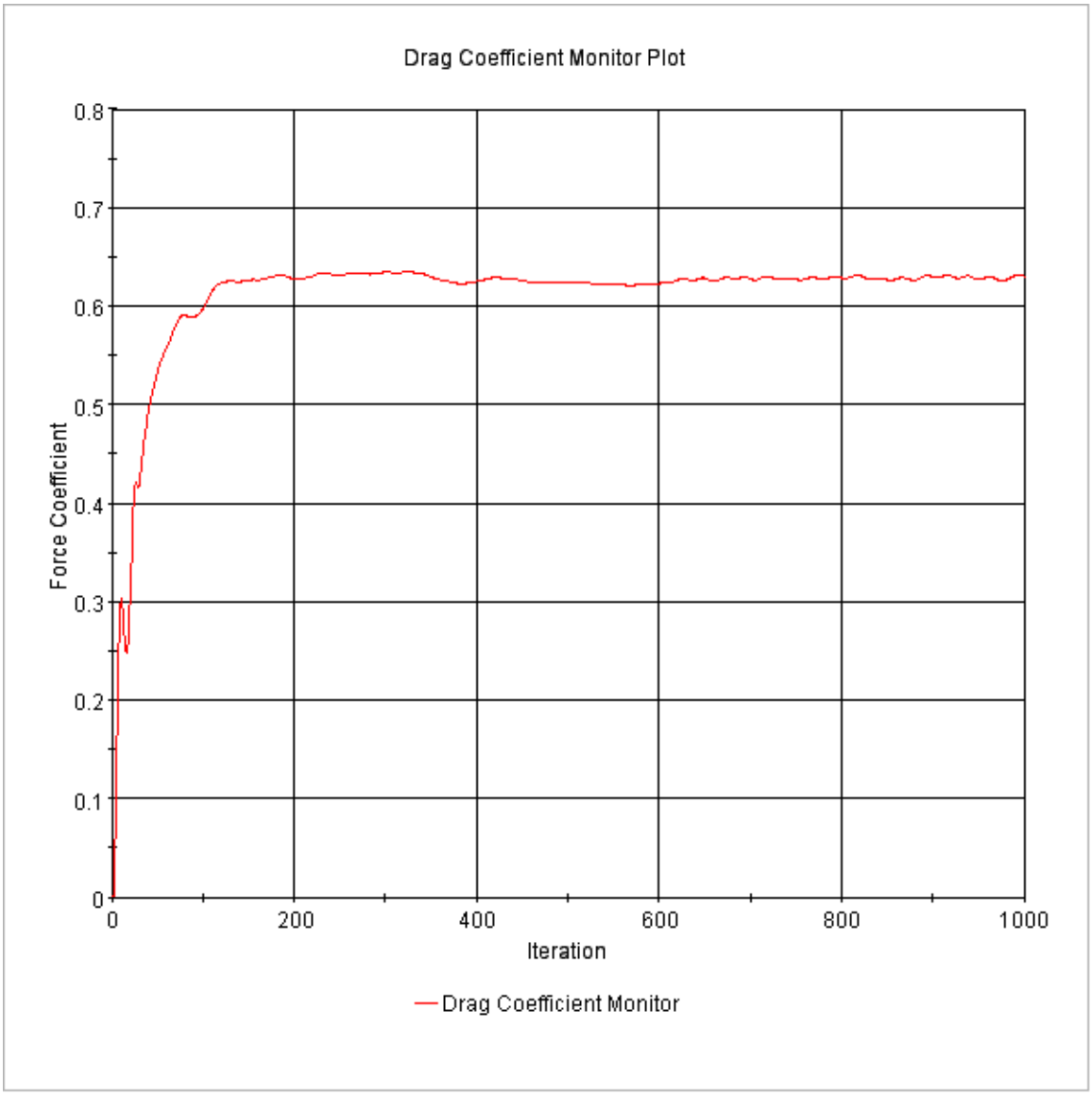

Figure 69 – Drag Coefficient Plot for Mid Position at 5° Yaw

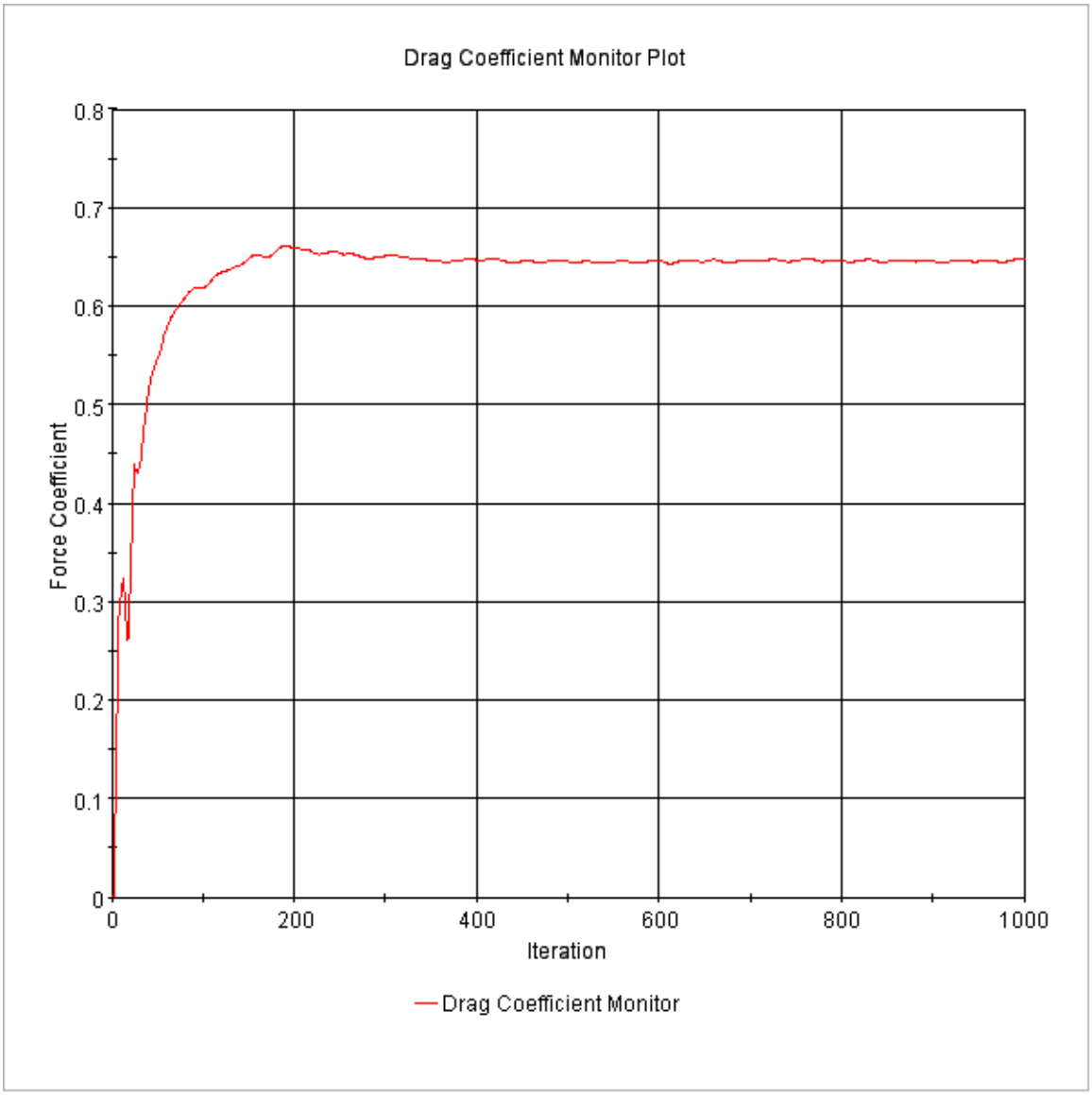

Figure 70 – Drag Coefficient Plot for Mid Position at 7.5° Yaw

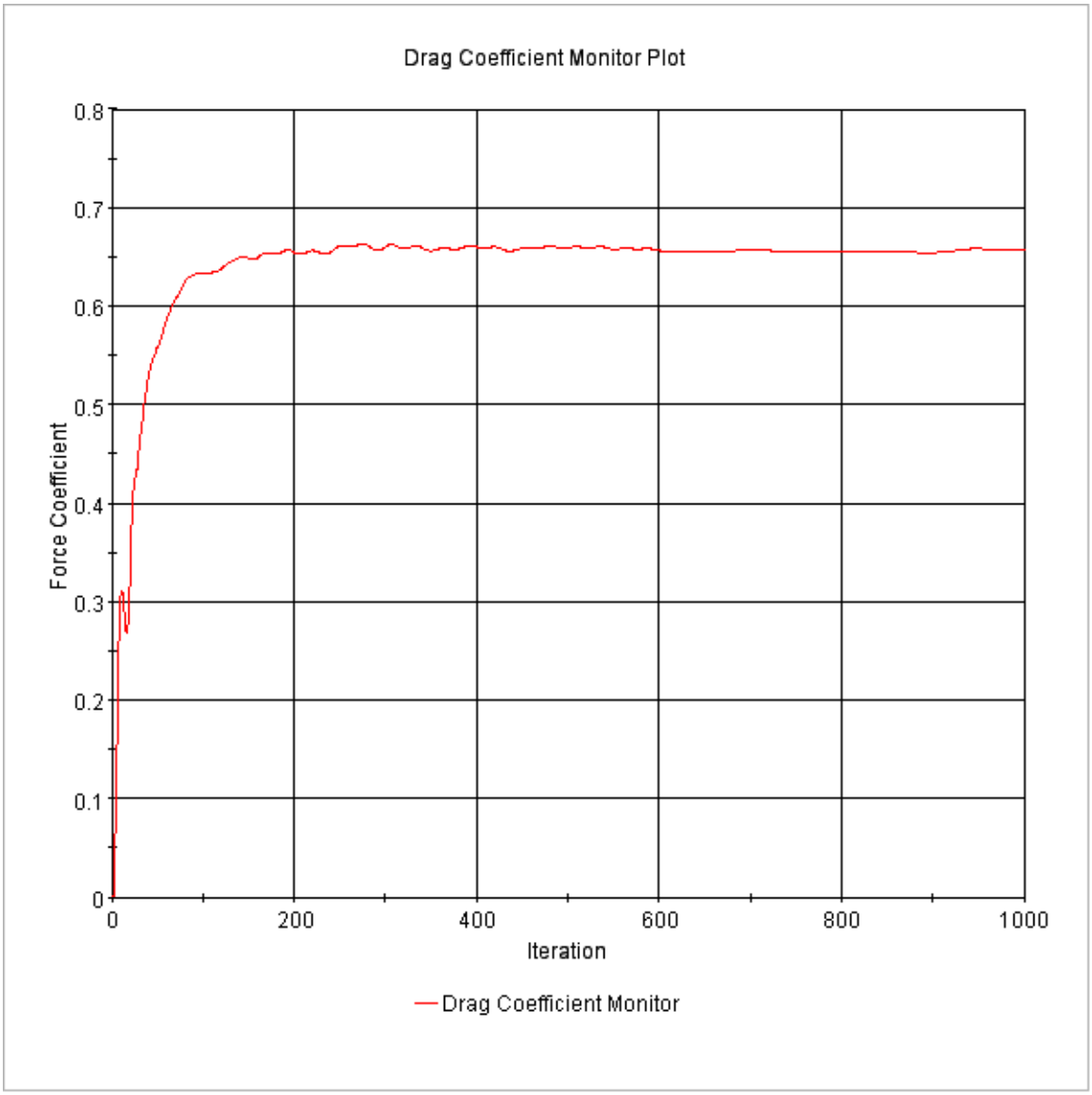

Figure 71 – Drag Coefficient Plot for Mid Position at 10° Yaw

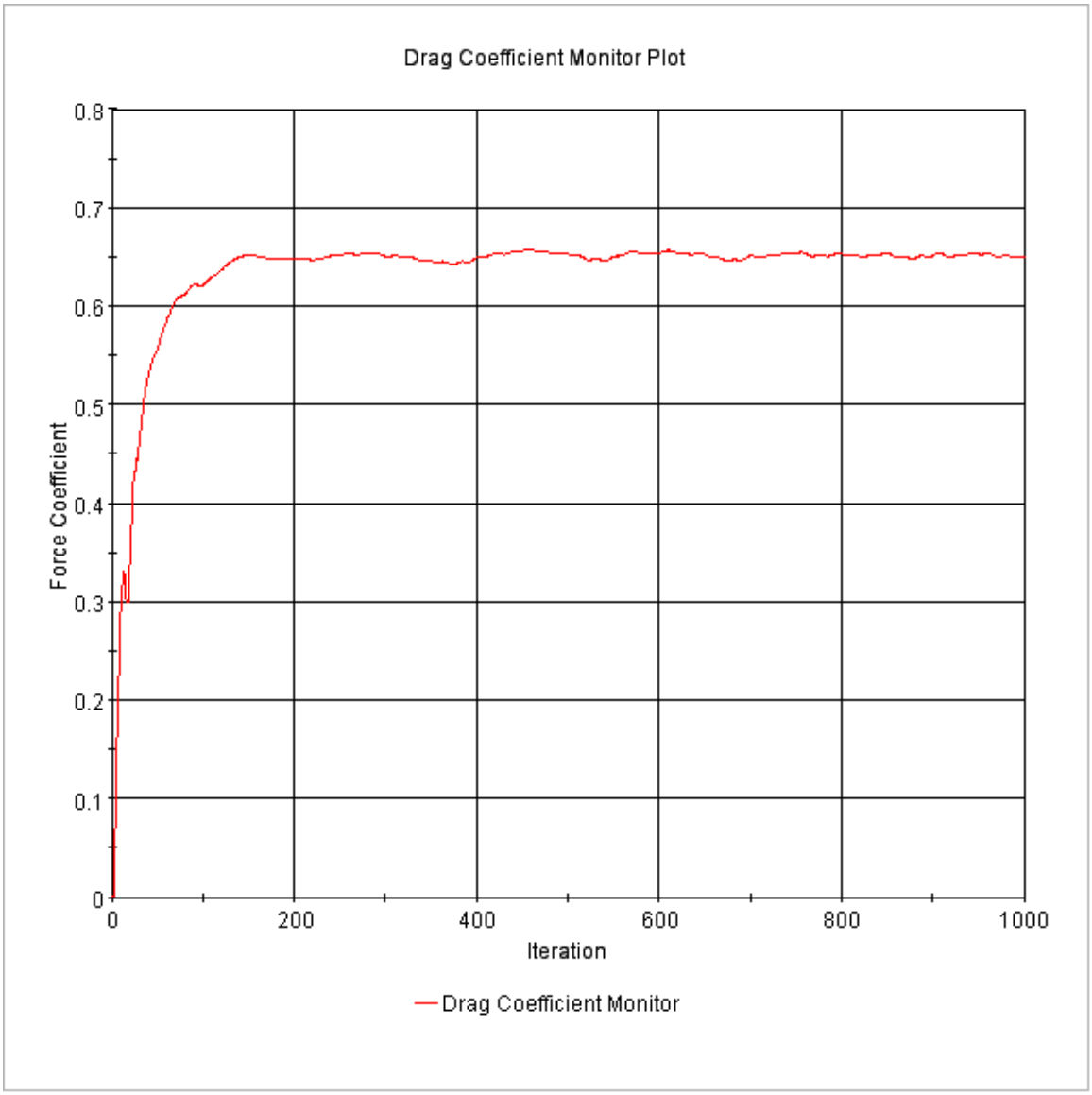

Figure 72 – Drag Coefficient Plot for Mid Position at 12.5° Yaw

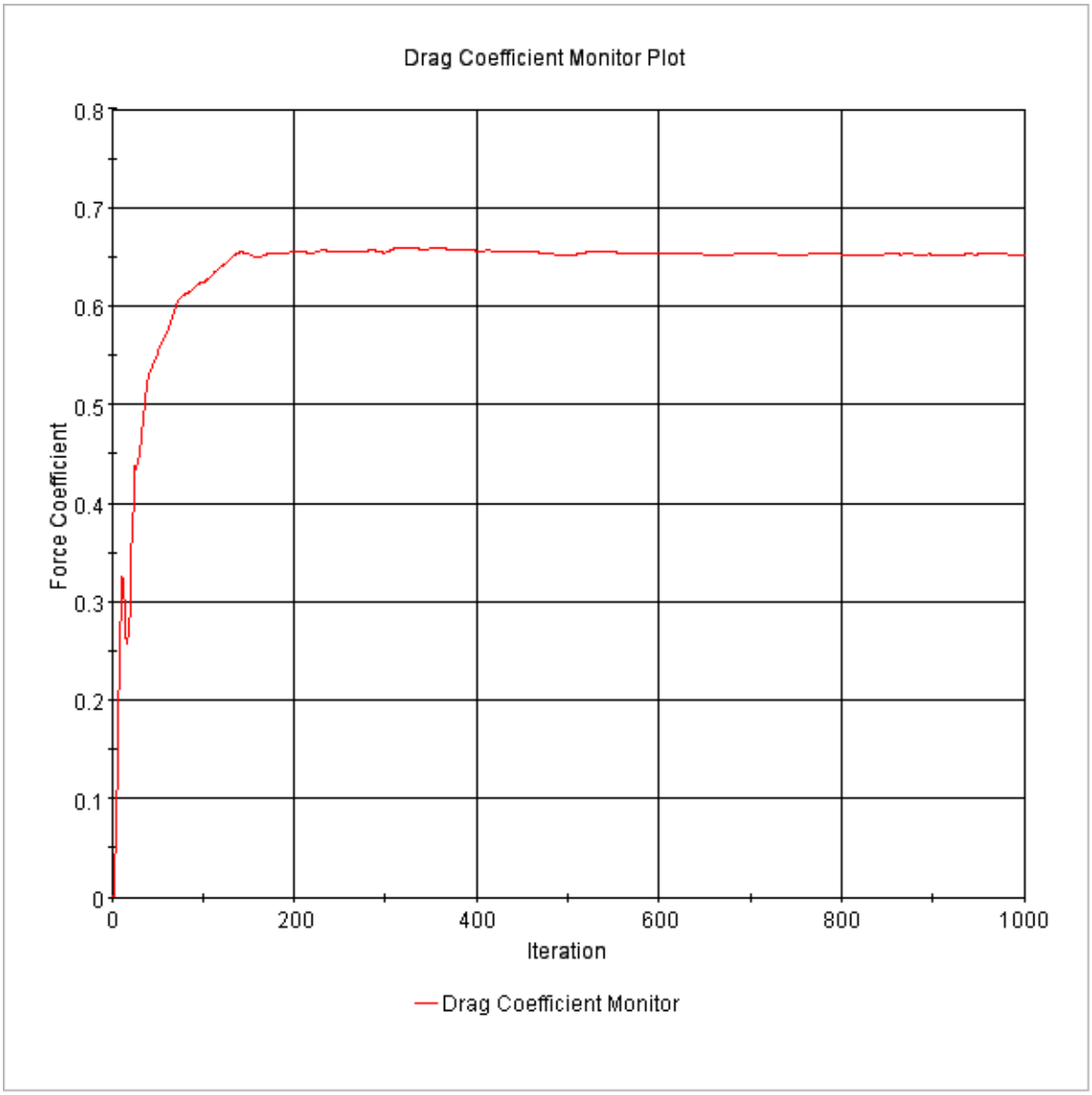

Figure 73 – Drag Coefficient Plot for Mid Position at 15° Yaw

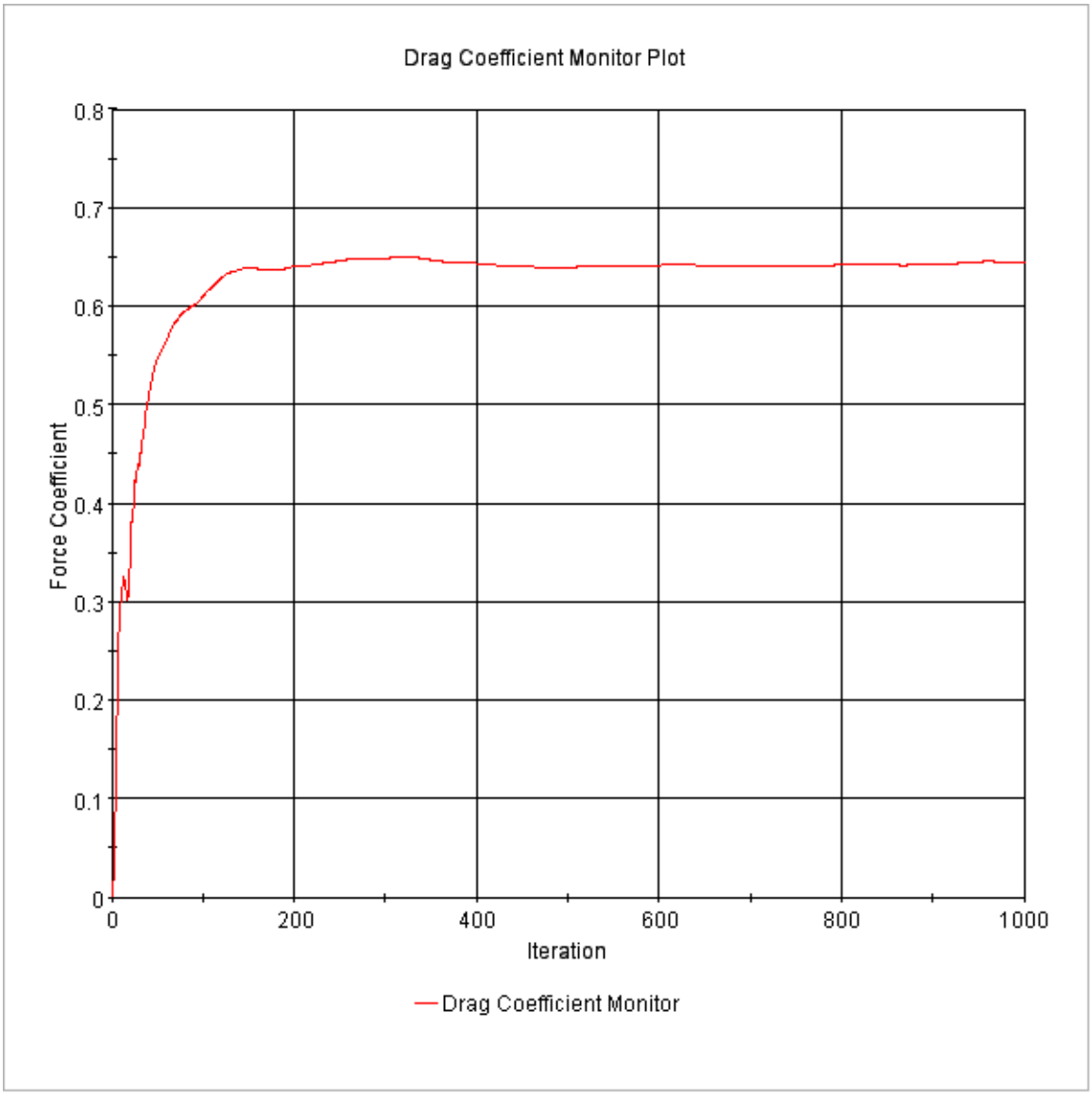

Figure 74 – Drag Coefficient Plot for Extreme Position at 0° Yaw

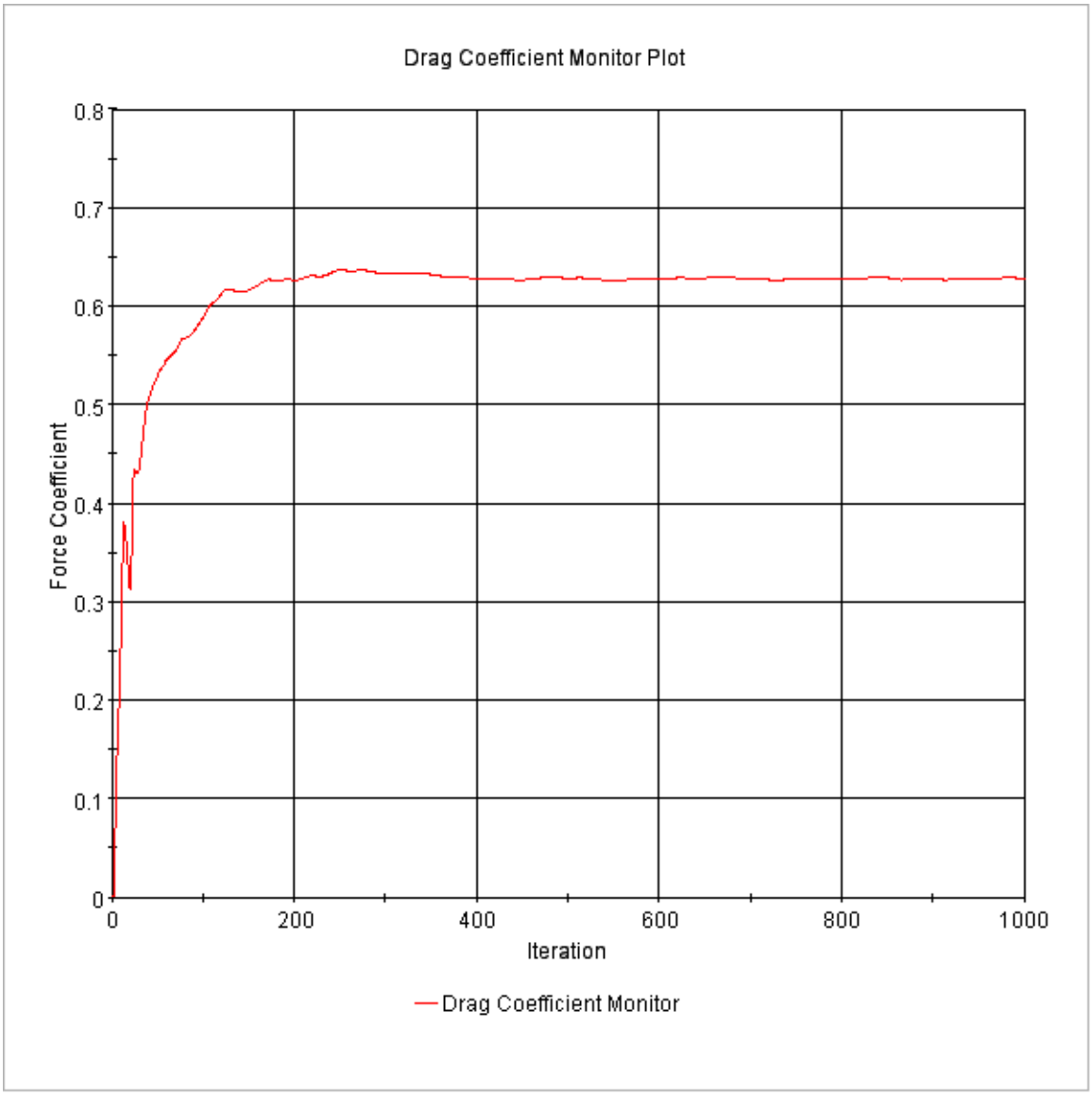

Figure 75 – Drag Coefficient Plot for Extreme Position at 2.5° Yaw

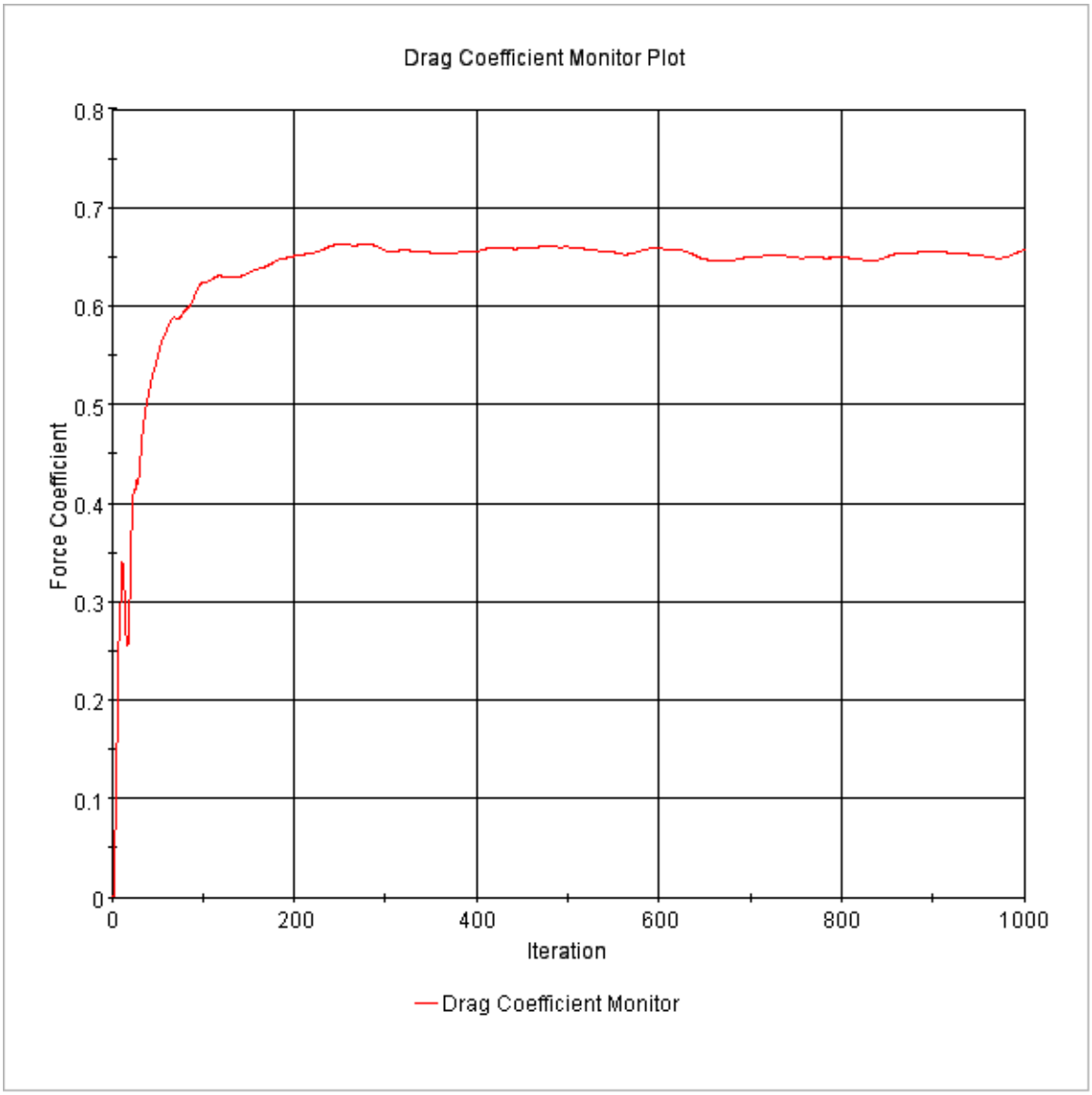

Figure 76 – Drag Coefficient Plot for Extreme Position at 5° Yaw

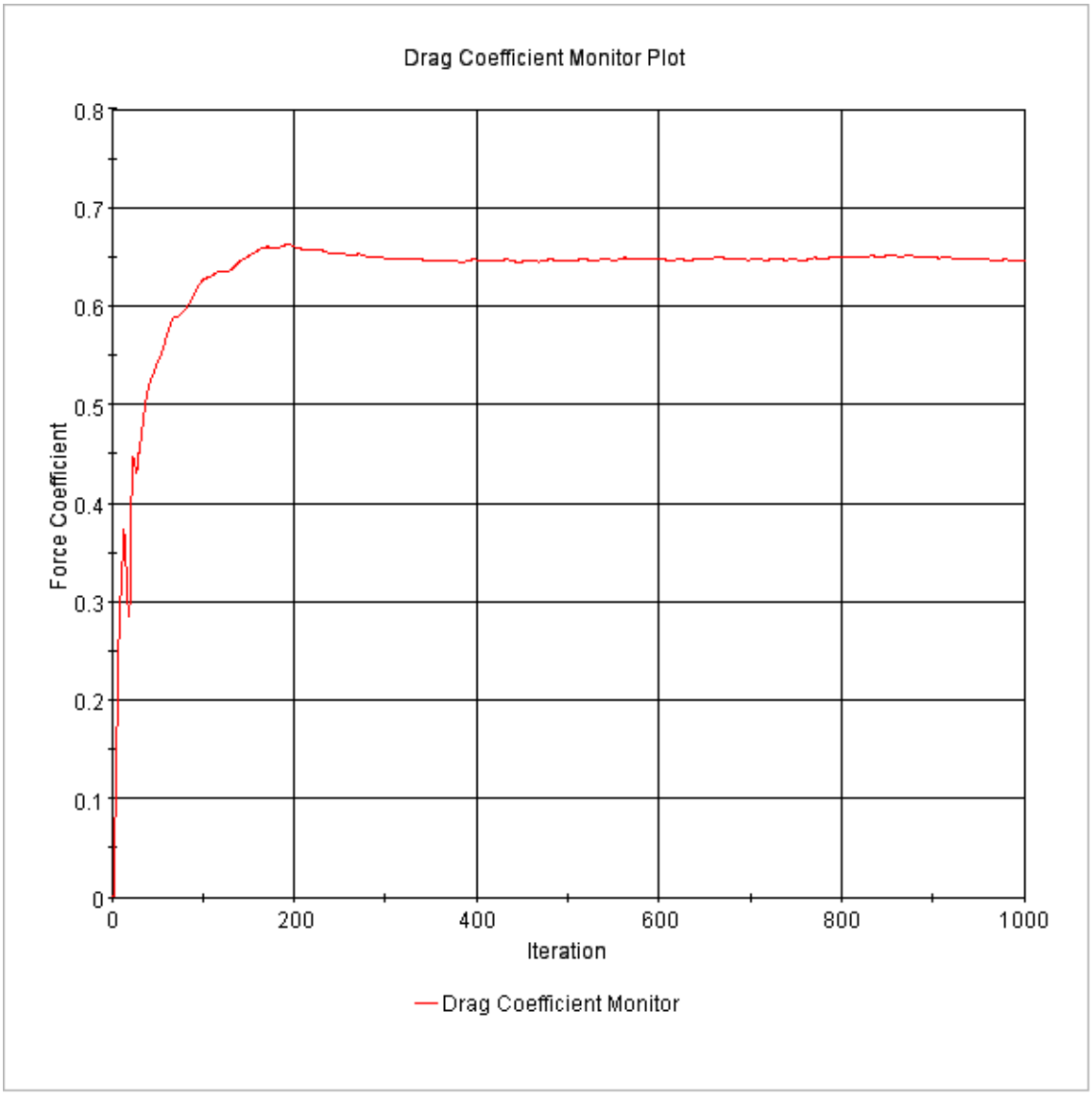

Figure 77 – Drag Coefficient Plot for Extreme Position at 7.5° Yaw

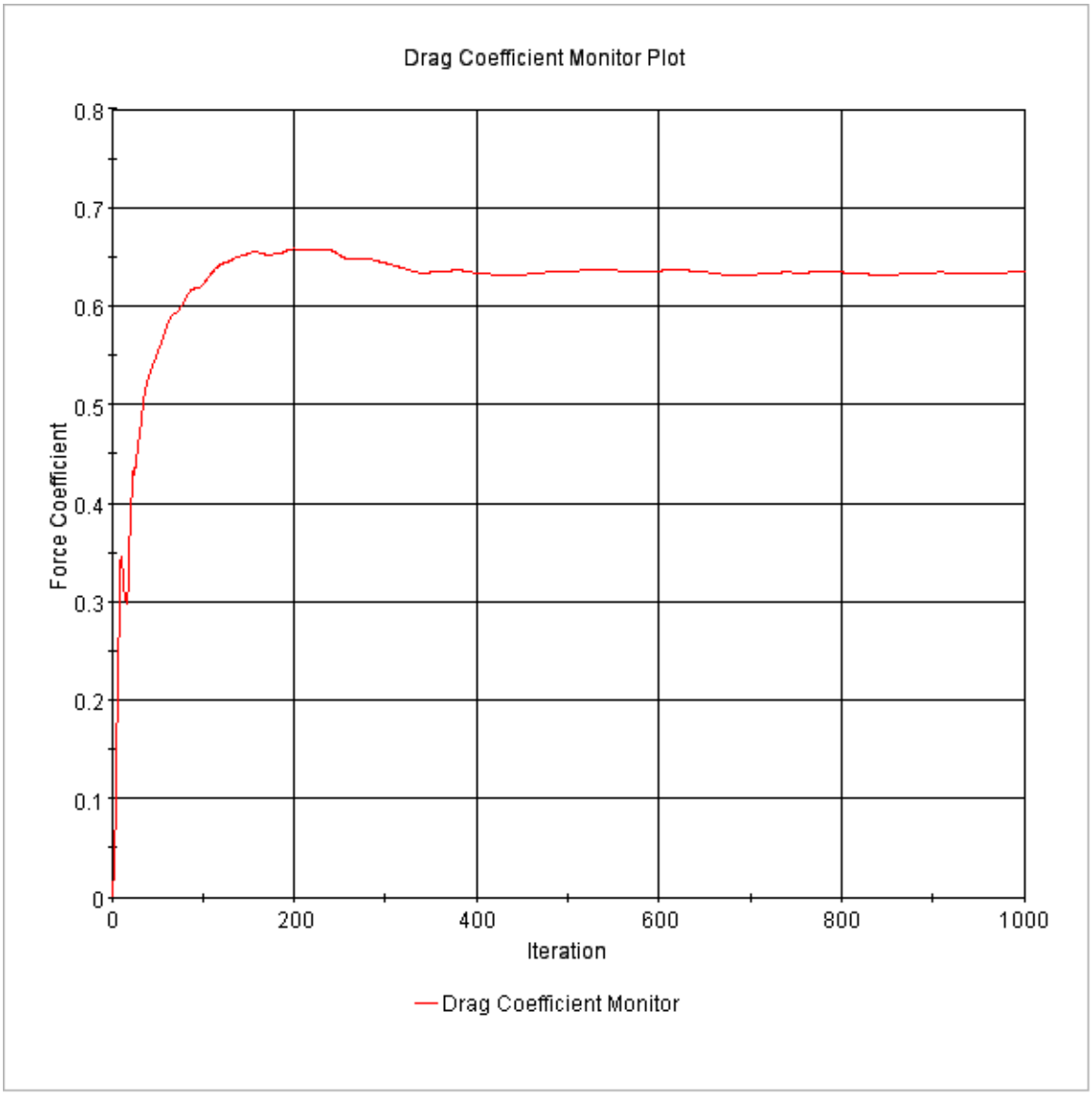

Figure 78 – Drag Coefficient Plot for Extreme Position at 10° Yaw

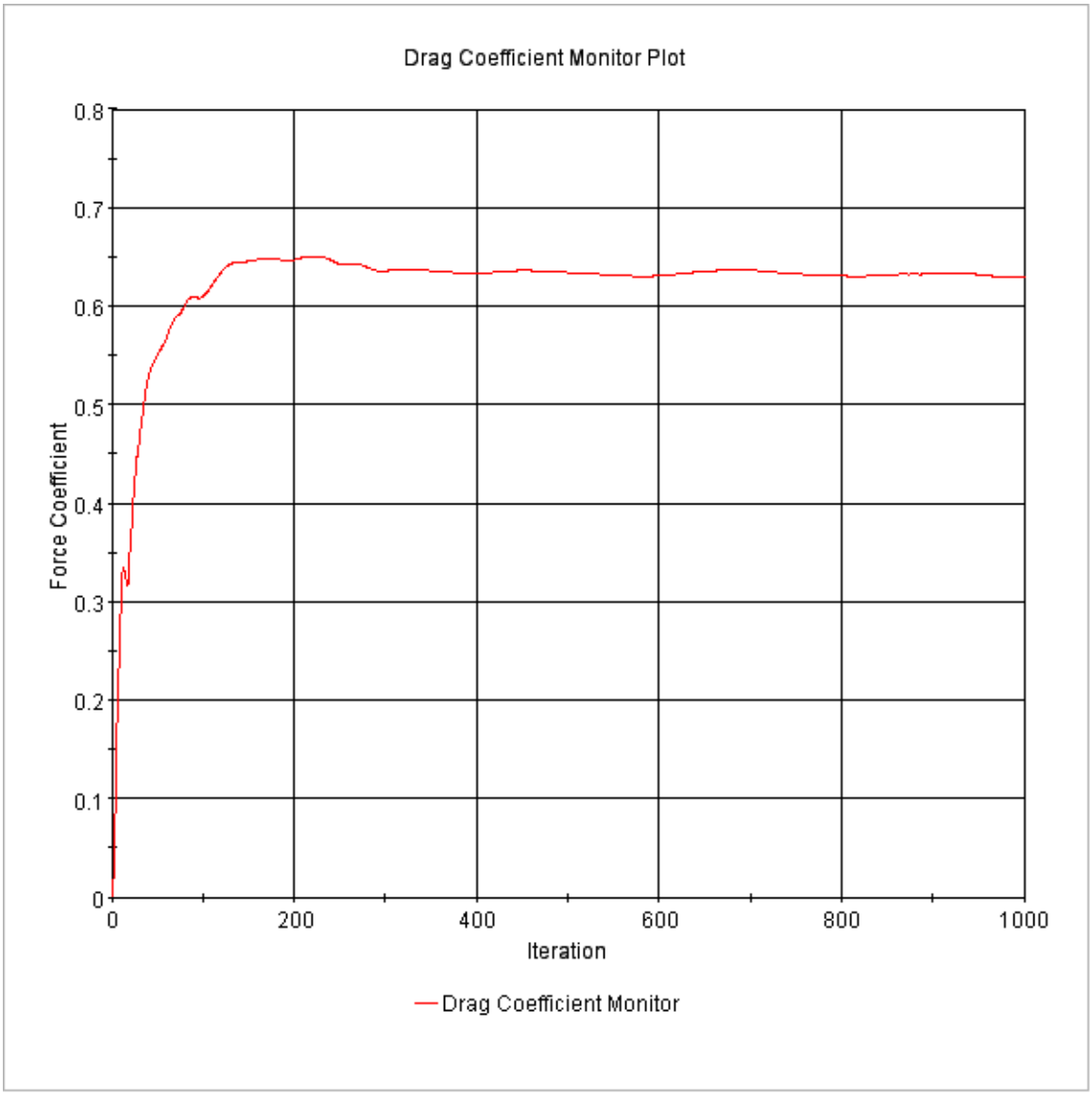

Figure 79 – Drag Coefficient Plot for Extreme Position at 12.5° Yaw

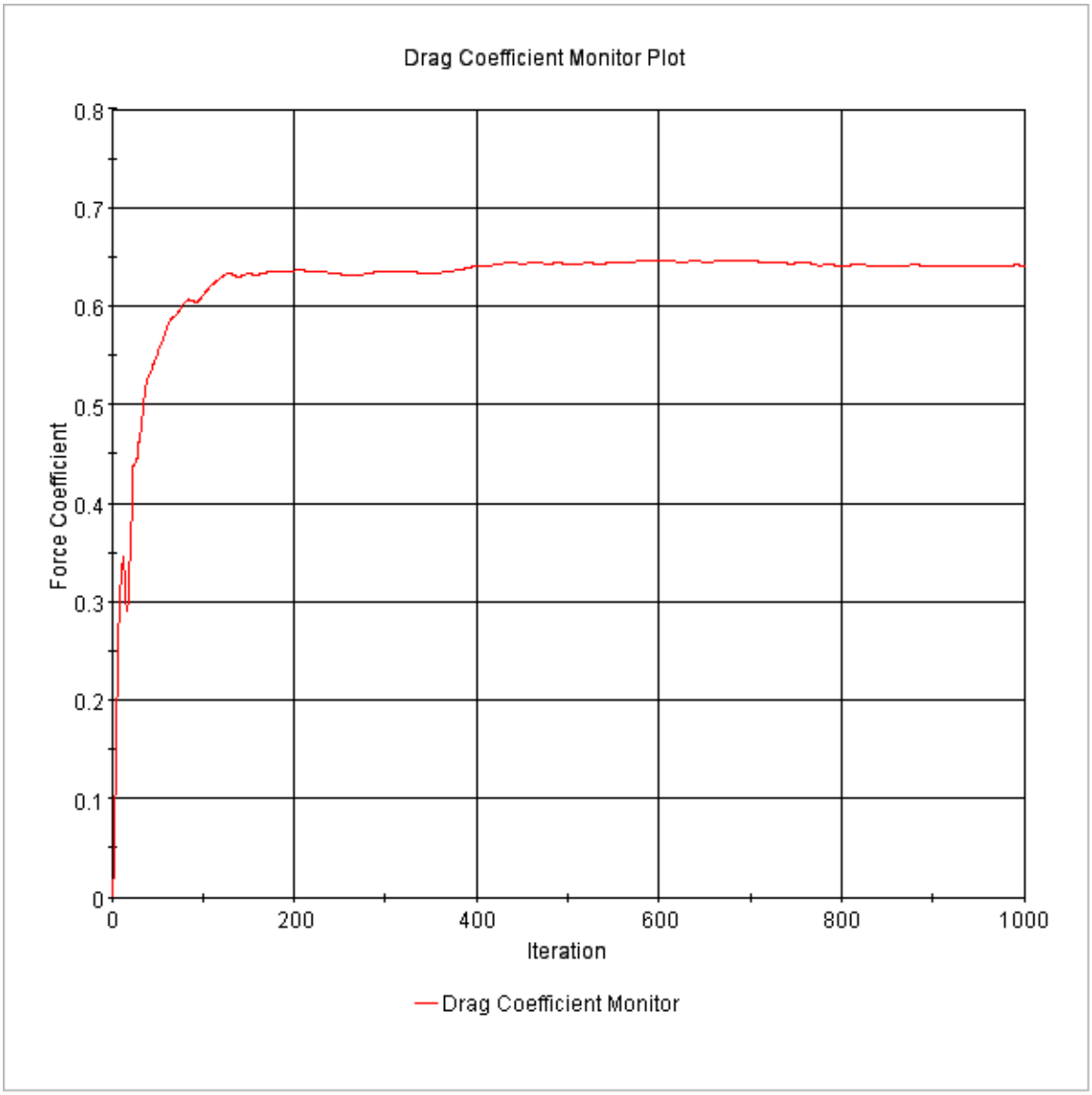

Figure 80 – Drag Coefficient Plot for Extreme Position at 15° Yaw